Dissertation
submitted to the
Combined Faculties for the Natural Sciences and for Mathematics
of the Ruperto-Carola University of Heidelberg, Germany
for the degree of
Doctor of Natural Sciences

Put forward by
Diplom Physiker Michael Heck
born in: Trier
Oral examination: 04.02.2013

Investigation of various excitation and detection schemes of stored ions in a Penning trap

Referees:

Prof. Dr. Klaus Blaum
Priv. Doz. Dr. Wolfgang Quint

Zusammenfassung:
Mit einem breitbandigem Fourier-Transformation Ionen-Zyklotron-Resonanz (FT-IZR) Massenspektrometer kann die Masse von Atomen und Molekülen in einem Bereich von einer bis hin zu einigen tausend atomaren Masseneinheiten bestimmt werden. Die Masse kann innerhalb einer kurzen Zeitdauer von ungefähr einer Sekunde mit einer Präzision von ca. 1 ppm gemessen werden. Weiterhin können auch Ionensorten mit einer geringen Häufigkeit ab einigen tausend Ionen detektiert werden. In dieser Arbeit wird der Aufbau und die Charakterisierung eines FT-IZR Massenspektrometers präsentiert, welches am Max-Planck-Insitut für Kernphysik in Heidelberg installiert ist. Das Massenspektrometer ist gezielt konstruiert um grundlegende Untersuchungen zu Detektions- und Anregungsschemata durchzuführen. Dazu wurde ein neues FT-ICR Detektionssystem erfolgreich aufgebaut. Es werden Untersuchungen zur Wechselwirkung von Ein- und Zwei-Puls Quadrupol-Anregungsfeldern mit Lithium-Ionen präsentiert. Da für den Nachweis viele Ionen notwendig sind, spielen Coulombwechselwirkungen zwischen den gespeicherten Ionen eine bedeutende Rolle. Die beobachteten Phänomene, wie Abschirmung von Anregungsfeldern und Ion-Ion-Wechselwirkung, werden diskutiert. Um diese Effekte qualitativ zu verstehen, wurden Vielteilchensimulationen durchgeführt. Weiterhin wurde die Genauigkeit und Präzision des Massenspektrometers aus Frequenzverhältnismessungen bestimmt.

Summary:
In mass spectrometry the masses of atoms or molecules in a large mass range up to a few thousand atomic mass units nowadays are determined by the so-called Fourier Transform Ion Cyclotron Resonance (FT-ICR) method. The mass can be measured within a few seconds with a high-precision of about 1 ppm. Furthermore, ion species with a low abundance of a few thousand ions can be detected. In this thesis the commissioning and the characterization of such an FT-ICR mass spectrometer will be presented. The experiment is installed at the Max Planck Institute for Nuclear Physics in Heidelberg. The mass spectrometer is constructed in such a way that various detection and excitation schemes can be investigated. Results concerning the one- and two-pulse quadrupolar excitation schemes are presented. Since many ions are trapped simultaneously, space charge effects play a crucial role. The observed phenomena like shielding of excitation fields and ion-ion interaction are discussed. Here, many particle simulations are performed to understand the observed phenomena. Furthermore, accuracy and precision limit studies of this mass spectrometer are discussed.

Contents

List of Tables

List of Figures

Chapter 1

Introduction and motivation

One of the basic properties of an atom is its mass. Atoms consist not only of nucleons and electrons but binding energy, caused by the atomic and nuclear binding forces. Einstein's famous energy-mass relation [1], $E = mc^2$, is an important link between the mass and the energy in nature allowing atomic mass spectrometry to provide a better understanding of the underlying interactions. In physics studies in general, high-precision mass measurements contribute to various fields, such as atomic physics (binding energy, quantum electrodynamics) [2], nuclear physics (nuclear structure, shell models) [3] or astrophysics (r-process, rp-process). In chemistry, high-precision mass measurements are needed to investigate the elemental composition of biomolecules, metals and clusters, biological macromolecules and petrochemicals. Relative precision $\delta m/m$ requirements for different fields of study vary considerably [4]. For stable atomic nuclides in atomic physics a precision of 10^{-11} is needed [5] while $10^{-9} - 10^{-6}$ is sufficient for studies of unstable nuclides in astrophysics and nuclear physics [6]. In chemistry and biology a precision of $10^{-6} - 10^{-5}$ is enough to assign the elemental compositions of a sample [7].
Modern high-precision mass spectrometry is based on linking the particle's mass to an oscillation frequency, which can be determined with highest precision. This principle is used in Penning-trap mass spectrometry, which is currently the most precise in the world. A Penning trap confines electrically charged particles by the superposition of a strong homogeneous magnetic field and a weak electrostatic quadrupole potential [8]. From the motional frequencies of the ion in the trap one can determine the so-called cyclotron frequency, which is only a function of particle's charge-over-mass ratio and the magnetic field, and thus enables determination of particle's mass. The main advantage of a Penning trap is that the ions are stored within a small volume isolated from external environmental influences. This makes such an apparatus a powerful tool in antimatter studies for example to perform mass measurements of antiprotons to test the CPT invariance (charge conju-

gation, parity and time reversal) [9] and to synthesize antihydrogen by simultaneously trapping positrons and antiprotrons [10, 11].

In Penning-trap mass spectrometry, two main detection methods are in use [4]. One is based on a time-of-flight measurement upon ejection of ions from the trap [12] and the other on detecting the ion motion of trapped particles through the image charges induced on the trap electrodes [13]. The time-of-flight method is common in studies of short-living ions as the mass measurement can be performed in rather short time. The drawback of the time-of-flight measurement is that the ion sample is lost after detection. The methods based on image charge detection are non-destructive. One of these methods is the so-called Fourier Transform Ion Cyclotron Resonance (FT-ICR) method, which was developed by the chemists M.B. Comisarow and A.G. Marshall in 1974. The advantage of an FT-ICR mass spectrometer is that a broad mass-to-charge range can be detected simultaneously within one second. Typically, the detectable mass range is from one to a few thousand atomic mass units [13] [14], which makes the FT-ICR method a powerful method for characterizing components of complex molecules with a sub ppm precision. Nowadays higher magnetic fields are used to increase the resolving power for analysing even more complex and heavier mixtures. For a measurement with a high-precision on the level of 10^{-11} cryogenic narrow-band detection systems are used [15]. Those have low noise level and are sensitive to a single ion stored in a Penning trap.

A broad-band FT-ICR Penning-trap mass spectrometer has been built at the Max Planck Institute for Nuclear Physics (MPIK) in Heidelberg. The trap was designed for the KArlsruhe TRItium Neutrino (KATRIN) experiment [16] in order to identify undesired components in the beam flux of the electron beam. Two Penning-trap mass spectrometers will be installed in the beam line of KATRIN in two different locations to monitor the reduction of the undesired beam flux. The mass spectrometers can perform a direct mass identification within half a second without disturbing the performance of the KATRIN experiment.

This thesis presents improvements on the existing FT-ICR Penning-trap mass spectrometer setup in Heidelberg. For instance, a new FT-ICR detection system has been installed. The setup allows to investigate different ion motion excitation methods as well as various FT-ICR detection schemes with multiple simultaneously stored ions.

Chapter 2 of this thesis explains the theoretical basics and concepts of Penning-trap physics. This includes storage, excitation and image charge detection of charged particles. In particular, a theoretical description of the quadrupolar excitation method based on the quantum mechanical treatment of an ion motion in a Penning trap will be presented. In addition, a theoretical model describing the induced image charges on a cylindrical detection plate is derived in a form of a Fourier series, which is needed to interpret the Fourier

spectra obtained in the experiment.

The broad-band FT-ICR setup consisting of the Penning trap and the superconducting magnet will be presented in Chapter 3. For the Penning trap, the electrostatic trapping potential including field imperfections will be characterized. The superconducting magnet used for this experiment will be analysed in detail.

In Chapter 4, the new FT-ICR detection system consisting of a broad-band amplifier system, a transient recorder and the FT-ICR control system will be discussed. The control system has been developed for controlling the excitation as well as the detection schemes of a measurement cycle. The characterization of the cryogenic broad-band amplifier for the KATRIN experiment as well as the room-temperature broad-band amplifier will be described.

The experimental results will be presented and discussed in Chapter 5. In this work, the sideband coupling of a quadrupolar excitation field to the ion motion is investigated in detail using the FT-ICR detection method, published in Ref. [17]. Results for both the one-pulse and two-pulse methods will be presented. The later one is also known as the Ramsey method which utilizes two time-separated but phase coherent excitation periods [18, 19].

With the trap used in these studies the FT-ICR ion detection is only possible with a high number of stored particles of roughly $10^3 \ldots 10^5$ ions. Therefore, Coulomb interactions and electric field screening effects have to be considered. Here, experimental results to observe the phenomena due to these effects will be presented. To understand these effects more qualitatively simulations of a dense ion cloud confined in a Penning trap have been performed.

In addition, accuracy and precision limit studies have been performed for the KATRIN project. Three methods for frequency ratio determination will be compared. All will be discussed in Chapter 5.

The thesis will end with a conclusion and outlook, presented in Chapter 6. In the future the setup at the MPIK in Heidelberg will be used for the new project called PIPERADE (PIège de PEnning pour des ions RAdioactifs à DEsir).

Chapter 2

Penning trap theory

In Penning-trap mass spectrometry the measurement of a nuclear, atomic or molecular mass is done via a frequency measurement of a charged particle. In physics, frequencies are measured with the highest precision and accuracy compared to all other physical quantities [4]. The most common device used for high-precision mass determinations is the Penning trap [20].

In this chapter the theoretical basics for understanding the ion storage in a Penning trap as well as the experimental methods for the ion excitation and detection are presented. First, the ion motion and the characteristic eigenfrequencies of a stored particle in an ideal Penning trap is discussed in Section 2.1. After this, deviations from the ideal Penning trap is described.

The ion motion of the stored particles can be manipulated by the application of external electric radio-frequency (rf) fields. A detailed theoretical description of the azimuthal dipolar and quadrupolar excitation fields is explained in Section 2.2. The theoretical description of the quadrupolar excitation is needed to compare experimental and theoretical results. These studies were already published by M. Heck *et al.* in [17].

The detection of the charged particles is experimentally done with the Fourier Transform Ion Cyclotron Resonance (FT-ICR) method within this thesis. The theoretical basics for the calculations of the image charges on the detection segments is derived in form of a Fourier series (see Section 2.3). Finally the limitations of the observed FT-ICR signal-to-noise ratio (SNR) due to the amplifier's noise for a broad-band detection circuit is presented.

2.1 Ion storage in a Penning trap

A charged particle in a purely electrostatic field cannot be in a stable equilibrium due to Earnshaw's theorem [21]. Gauss's Law states that the divergence of any electric force in free space is zero, thus the potential is divergence free and satisfies the Laplace equation. This means that only a saddle point can exist and, thus, no local minima or maxima of the electric potential occurs. To this end there is an instability at least in one direction which involves for a particle that no stable point exists. In order to avoid this instability, a strong homogeneous magnetic field in the direction of the instability is superimposed to a static quadrupolar electric potential. Such a device is called a Penning trap [22]. H. Dehmelt and W. Paul received *for the development of the ion trap technique* one half of the Nobel Prize in Physics in year 1989 while the other half was awarded to Norman F. Ramsey *for the invention of the separated oscillatory fields method and its use in the hydrogen maser and other atomic clocks* [18].

2.1.1 A single particle in an ideal Penning trap

An ideal Penning trap consists of the following configuration [4, 8]: a superposition of a homogeneous magnetic field, $\vec{B} = B_0\vec{e}_z$, which confines a particle in the radial direction, and a static quadrupolar electric field which traps the particle axially. These two fields cause the Lorentz force $\vec{F}_\mathrm{L}$ which acts on a charged particle with a mass m and a charge q moving with the velocity $\vec{\mathrm{v}}$ in the Penning trap

$$\vec{F}_\mathrm{L} = q(\vec{E} + \vec{\mathrm{v}} \times \vec{B}). \tag{2.1}$$

In an electric field free region, the magnetic field constraints the particle to a circular motion perpendicular to the z-direction at the so-called cyclotron frequency

$$\omega_\mathrm{c} = 2\pi\nu_\mathrm{c} = \frac{q}{m}B_0. \tag{2.2}$$

The cyclotron frequency ω_c has an important impact in mass spectrometry due to its dependence on the charge-to-mass ratio of the charged particle. The cyclotron frequency of a particle at the same charge state increases when the mass decreases.
Figure 2.1 shows schematically a Penning trap configuration for a hyperbolical (a) and cylindrical (b) geometry. The traps consist of one ring electrode, two correction electrodes and two endcaps. The hyperbolical type has two endcap electrodes, which are described by the two branches of the hyperbola of revolution $2z_0^2 = 2z^2 - x^2 - y^2$, and one ring electrode which is described by the hyperbola of revolution $-\rho_0^2 = 2z^2 - x^2 - y^2$. z_0 and ρ_0 are the minimum distances from the trap center to the endcap and ring electrodes,

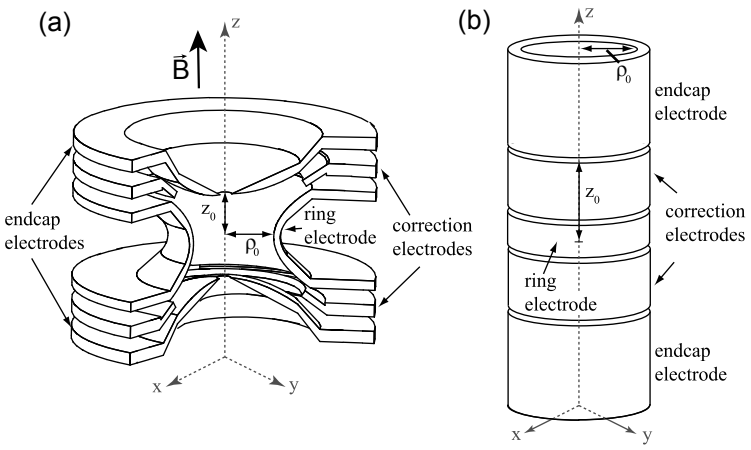

Figure 2.1: Scheme of a five-electrode hyperbolical (a) and cylindrical Penning trap (b) consisting of a ring-, two correction- and two endcap-electrodes. The geometrical trap parameters ρ_0 and z_0 are shown for both trap configurations. The magnetic field vector $\vec{B}$ is directed along the z-axis, which is the symmetry axis for both trap configurations. Courtesy of J. Repp [23].

respectively (see Fig. 2.1). For a hyperbolical trap, z_0 and ρ_0 define the characteristic trap parameter d

$$d^2 = \frac{1}{2}\left(z_0^2 + \frac{\rho_0^2}{2}\right). \tag{2.3}$$

In Eq. (2.1) the static electric field, $\vec{E} = -\nabla V$, is derived from the scalar quadrupolar potential which describes a saddle-point potential

$$V(x,y,z) = V_0 \frac{C_2}{2d^2}\left(z^2 - \frac{x^2+y^2}{2}\right), \tag{2.4}$$

where V_0 is the potential difference applied between the endcaps and the ring electrode and C_2 is the expansion coefficient depending on the geometry of the trap. For an ideal hyperbolical Penning trap C_2 is equal to one but for a real Penning trap deviations occur and in general C_2 depends on the potential applied to the correction electrodes.
Using $\vec{F} = m\ddot{\vec{x}}$ in the equation of motion (2.1) and inserting the quadrupolar electric field $\vec{E} = -\nabla V$ from Eq. (2.4), the x, y and z-components are written as

$$0 = \ddot{x} - \omega_c \dot{y} - \frac{1}{2}\omega_z^2 x \tag{2.5}$$

$$0 = \ddot{y} + \omega_c \dot{x} - \frac{1}{2}\omega_z^2 y \tag{2.6}$$

$$0 = \ddot{z} + \omega_z^2 z. \tag{2.7}$$

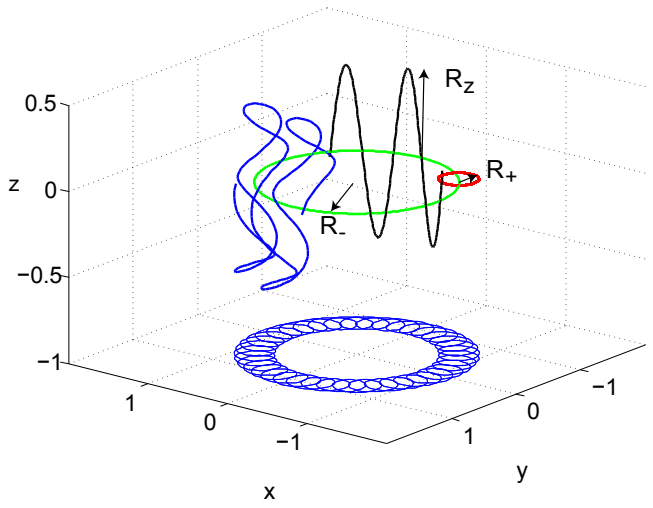

Figure 2.2: The three eigenmotions of an ion in a Penning trap. The black line corresponds to the axial oscillation with an amplitude R_z. The magnetron motion is an oscillation around the trap center (green circle with a radius R_-) and the modified cyclotron motion is superimposed to the magnetron motion (red circle with radius R_+). The blue curve corresponds to the superposition of all three eigenmotions. The radial motions are projected on the x,y-plane.

In z-direction, parallel to the magnetic field indicated in Fig. 2.1, the particle is bound due to the harmonic potential given in Eq. (2.4) and performs a harmonic oscillation at the axial frequency

$$\omega_z = 2\pi\nu_z = \sqrt{\frac{qV_0C_2}{md^2}} \tag{2.8}$$

with an amplitude R_z. The ion performs a stable motion if the axial frequency ω_z is real. It follows the trapping condition $qV_0 > 0$. In the radial plane, the cyclotron motion is modified by a weak repulsive electrostatic force which reduces the centrifugal force by $\frac{1}{2}\omega_z^2 x$ in x-direction and $\frac{1}{2}\omega_z^2 y$ in y-direction (see Eqs. (2.5) and (2.6)). This leads to a superposition of a stable and an unstable radial motion as described in the following.
The x- and y-components of the Eqs. (2.5) and (2.6) can be coupled by the introduction of a complex variable $u = x + \mathrm{i}y$. With the ansatz $u = e^{-\mathrm{i}\omega t}$, an algebraic condition can be derived

$$\omega^2 - \omega_c\omega + \frac{1}{2}\omega_z^2 = 0. \tag{2.9}$$

The roots of this equation are the eigenfrequencies of the radial motions and given by

$$\omega_\pm = 2\pi\nu_\pm = \frac{1}{2}\left(\omega_c \pm \omega_1\right) \tag{2.10}$$

where

$$\omega_1 = \sqrt{\omega_c^2 - 2\omega_z^2}. \tag{2.11}$$

The radial eigenmotions are the modified cyclotron motion at the modified cyclotron frequency ω_+ and the magnetron motion at the magnetron frequency ω_-. A stable, periodic solution is observed when the following trapping condition is satisfied

$$\omega_c^2 - 2\omega_z^2 > 0. \tag{2.12}$$

This means that ω_1 has to be real (see Eq. (2.11)). The general solution for the classical amplitudes of the two radial motions is written as a superposition $u(t)$, with the complex amplitudes $A_\pm = |A_\pm| e^{-i\chi_\pm}$,

$$u(t) = A_+ e^{-i\omega_+ t} + A_- e^{-i\omega_- t} \tag{2.13}$$

where $|A_\pm| = R_\pm$ are the cyclotron and magnetron radii and $\chi_\pm$ are the phases of the motions, respectively.
Figure 2.2 shows a schematic view of all three eigenmotions. It should be noted that both radial modes have the same direction of rotation, as becomes apparent from Eq. (2.13). In Table 2.1, the eigenfrequencies $\nu_i = \omega_i/(2\pi)$ are listed for different mass numbers for the conditions of the FT-ICR Penning trap used in this thesis.

For an ideal Penning trap the following relations between the frequencies exist:

$$\omega_c = \omega_+ + \omega_-, \tag{2.14}$$

$$\omega_z^2 = 2\omega_+\omega_-, \tag{2.15}$$

$$\omega_c^2 = \omega_+^2 + \omega_-^2 + \omega_z^2. \tag{2.16}$$

The first equation, Eq. (2.14), is strictly speaking only valid for an ideal Penning trap and is known as the magnetron sideband at the modified cyclotron frequency. It relates the cyclotron frequency ω_c to the sum of the frequencies of the radial modes. From the Eqs. (2.12) and (2.15) follows a hierarchy of the eigenfrequencies: $\omega_+ > \omega_z > \omega_-$. An important relation between all three eigenfrequencies and the true cyclotron frequency is expressed in Eq. (2.16) which is known as the invariance theorem. It is valid even if a tilt angle between the magnetic field and the trap axis as well as an ellipticity of the electric field are present [8].
The highest precision for determining the cyclotron frequency ν_c is reached if all three eigenfrequencies are measured. The most precise mass measurements on stable nuclides have been achieved with a relative mass precision of $\delta m/m < 10^{-11}$ [5]. This makes the Penning trap a powerful tool for mass determination and fundamental research [4]. However, in sideband mass spectrometry short-lived nuclei are measured and the precision is

A	Element	ν_z / Hz	ν_+ / Hz	ν_- / Hz
6	^{6}Li	136290	11997740	774
18	H_2O	49440	4009000	774
32	O_2	37080	2255030	774

Table 2.1: The axial frequency ν_z, the modified cyclotron frequency ν_+ and the magnetron frequency ν_- for different mass numbers A calculated for a magnetic field B of 4.699 T, a trapping potential V_0 of 60 V and a coefficient C_2/d^2 of 770 m^{-2}.

generally limited by the half-life of the ion of interest and its intensity. Here the sideband frequency $\omega_+ + \omega_-$ is measured yielding a relative mass uncertainty of typically $\delta m/m \approx 10^{-7} - ^{-8}$.

The magnetron frequency in Eq. (2.10) can be approximated with a Taylor expansion to the first order

$$\omega_- = \frac{V_0 C_2}{2d^2 B}. \tag{2.17}$$

The frequency ω_- depends on the electromagnetic fields of the Penning trap and is mass independent, which is an advantage for a motional excitation of all stored ion species simultaneously, as will be shown later. The magnetron motion is equivalent to a radial drift with the velocity $\vec{v} = \vec{E} \times \vec{B}/|\vec{B}|^2$ of a charged particle in the crossed electric and magnetic trapping field.

The mean potential energy E_{pot} of a stored ion in a Penning trap is calculated using the time dependent solutions of the ion motion:

$$\begin{aligned} E_{\text{pot}} &= -\lim_{T\to\infty} \frac{q}{T} \int_0^T V(x(t), y(t), z(t)) \mathrm{d}t \\ &\approx -\frac{qV_0C_2}{4d^2}(R_+^2 + R_-^2 - R_z^2). \end{aligned} \tag{2.18}$$

Equation (2.18) can be simplified if the pre-factor is replaced by $\omega_z^2/4$ and if Eq. (2.15) is used. The total energy of all three motional modes is then given by the sum of the kinetic and potential energies

$$\begin{aligned} E_{\text{total}} &= \frac{m}{2}(R_+^2\omega_+^2 + R_z^2\omega_z^2 + R_-^2\omega_-^2) + E_{\text{pot}} \\ &= \frac{m}{2}R_+^2(\omega_+^2 - \omega_+\omega_-) + \frac{m}{2}R_z^2(\omega_z^2 + \omega_+\omega_-) + \frac{m}{2}R_-^2(\omega_-^2 - \omega_+\omega_-). \end{aligned} \tag{2.19}$$

The energy of the magnetron mode is negative due to $(\omega_-^2 - \omega_+\omega_-) < 0$ and almost exclusively potential energy. Thus removing energy from the magnetron mode will increase the magnetron radius. The energy of the cyclotron mode is almost a purely kinetic energy.

The eigenmotions can be described by three independent harmonic oscillators. Thus quantizing the coordinates and momenta leads to a harmonic oscillator Hamiltonian [8] which has well-known eigenvalues. The total energy of a single charged spinless particle is given by the Landau levels:

$$E_{\text{total}} = \hbar\omega_+ \left(n_+ + \frac{1}{2}\right) + \hbar\omega_z \left(n_z + \frac{1}{2}\right) - \hbar\omega_- \left(n_- + \frac{1}{2}\right), \tag{2.20}$$

where n_+, n_- and n_z are the quantum numbers in the respective mode and $\hbar$ is Planck's constant. The total energy is given by the sum of the radial and axial energy eigenvalues.

2.1.2 The real Penning trap

In a real Penning trap, electric and magnetic field imperfections lead to a shift of the ion's eigenfrequencies. These frequency shifts depend on the motional amplitudes. Furthermore, effects like relativistic mass increase, Coulomb interactions, image charge interactions, and misalignment and distortion of fields lead to a deviation from the ideal Penning trap.

Imperfections of the electric field: The tolerances in machining the electrodes and their finite size can contribute to electrostatic imperfections. Additionally the segmentation of electrodes, holes, slits and the assembling of the Penning trap lead to field distortions. For any Penning trap, one has an invariance under rotation about the z-axis from which follows that only even terms have to be added to the quadrupolar potential given in Eq. (2.4). The lowest order potential imperfection ΔV of the harmonic potential is given by the octupolar term C_4

$$\Delta V = V_0 \frac{C_4}{2d^2}(z^4 - 3z^2(x^2+y^2) + \frac{3}{8}(x^2+y^2)^2). \tag{2.21}$$

In order to minimize the octupolar and higher order terms (not taken into account here), one can use correction electrodes between the ring and the endcap electrodes as shown in Fig. 2.1.

Imperfections of the magnetic field: Magnetic fields are divergence free due to Maxwell equations. The coils of the superconducting magnet have a finite length which leads naturally to a radial component of the magnetic field. In the center of a superconducting magnet the magnetic field is described by the superposition of a homogeneous magnetic field $\vec{B} = B_0\vec{e}_z$ and a weak magnetic bottle $\Delta\vec{B}$:

$$\Delta\vec{B} = B_2[(z^2 - (x^2+y^2)/2)\vec{e}_z - z(x\vec{e}_x + y\vec{e}_y)] \tag{2.22}$$

which is the lowest order imperfection.

Relativistic effects: Due to the fact that the relativistic mass increases with the velocity v of a particle, the cyclotron and axial frequencies shift to lower values compared to the frequencies of the rest mass m_0. The relativistic mass m is given by

$$m = \frac{m_0}{\sqrt{1-(\mathrm{v}/c)^2}} \tag{2.23}$$

where c is the speed of light.

Resulting frequency shifts for ω_+ and $\omega_\mathrm{c} = \omega_+ + \omega_-$: The eigenfrequencies of the ion motions in an ideal trap are independent on the motional amplitudes. However, the electric and magnetic field imperfections as well as the relativistic effect cause systematic frequency shifts, which depend on the motional amplitude. We consider here only the first order corrections $\Delta\omega_+$ and $\Delta\omega_\mathrm{c}$ of the modified cyclotron frequency and the cyclotron frequency, respectively [8]:

$$\begin{aligned}\Delta\omega_+ &= \frac{1}{2}R_+^2\left(-\frac{B_2}{B_0}\omega_+ + 3\omega_-\frac{C_4}{d^2} - \frac{\omega_+^3}{c^2}\right) + \frac{1}{2}R_z^2\left(\frac{B_2}{B_0}\omega_+ + 6\omega_-\frac{C_4}{d^2} - \frac{\omega_+^2\omega_-}{c^2}\right) + \\ &\quad \frac{1}{2}R_-^2\left(-\frac{B_2}{B_0}\omega_+ + 6\omega_-\frac{C_4}{d^2} - \frac{\omega_+\omega_-^2}{c^2}\right), \qquad (2.24)\\ \Delta\omega_\mathrm{c} &= \frac{1}{2}R_+^2\left(-3\omega_-\frac{C_4}{d^2} - \frac{\omega_+^3}{c^2}\right) + \frac{1}{2}R_z^2\left(\frac{B_2}{B_0}\omega_+ - \frac{\omega_+^2\omega_-}{c^2}\right) + \\ &\quad \frac{1}{2}R_-^2\left(-\frac{B_2}{B_0}\omega_+ + 3\omega_-\frac{C_4}{d^2} - \frac{\omega_+\omega_-^2}{c^2}\right). \qquad (2.25)\end{aligned}$$

Both frequency shifts depend quadratically on the radii R_+, R_- and the axial amplitude R_z. It should be noted that for the cyclotron frequency shift $\Delta\omega_\mathrm{c}$ the term with R_+ is independent on magnetic field imperfections.

Coulomb effects: The Coulomb force leads to a repulsion of the stored ions in the Penning trap. The consequences of this repulsive force are a line broadening of the resonance and a frequency shift. When regarding only two ion species the resolving power of the mass spectrometer determines if the resonance is resolved or not. The two ion species have the sideband frequencies $(\omega_+ + \omega_-)_1$ and $(\omega_+ + \omega_-)_1$, respectively. When the two resonance can be resolved, two peaks are measured, where the centres of the resonances are shifted to lower values. In the other case, one resonance is observed which occurs at the center-of-mass frequency. When only one ion specie with a high abundance is trapped, the a line broadening of the resonance is observed, which is due to the space charges [24].

Image charge shifts: The interaction of the coherent moving ion cloud with its image charges induced on the electrodes causes a frequency shift. The image charge frequency shift for a cylindrical trap has been described by X. Xiang *et al.* in Ref. [25] and is given by

$$\Delta\omega_+ = \frac{Nq}{\pi\varepsilon_0\rho_0 z_0 B_0 R_+}\sum_{m=1}^{\infty}\sum_{n=1}^{\infty} sin^2\left(\frac{n\pi R_z}{z_0}\right)\frac{I_m\left(\frac{n\pi R_+}{z_0}\right)I_{m+1}\left(\frac{n\pi R_+}{z_0}\right)}{I_m\left(\frac{n\pi\rho_0}{z_0}\right)I_{m+1}\left(\frac{n\pi\rho_0}{z_0}\right)}, \tag{2.26}$$

where N is the number of stored particles, R_+ is the modified cyclotron radius, R_z is the axial amplitude, and ε_0 is the vacuum permittivity. I_m is the modified Bessel function of order m.

Misalignment and distortion of fields: Another systematic frequency shift occurs due to the misalignment of the trap electrodes to each other and also with respect to the magnetic field axis. The equipotential lines of the quadrupolar potential are not circles anymore but modified by an ellipticity parameter ε. Additionally the magnetic field can be tilted with respect to the z-axis by an angle θ. The resulting frequency shift at the sideband frequency for a small ellipticity ($\varepsilon \gg 1$) and a small tilt ($\theta \gg 1$) is given by [26]

$$\Delta\omega_c = \omega_-\left(\frac{9}{4}\theta^2 - \frac{1}{2}\varepsilon^2\right). \tag{2.27}$$

Equation (2.27) is an amplitude independent frequency shift. One should notice that misalignment and distortion of fields cause no frequency shift on the modified cyclotron frequency ω_+ [8].

2.2 Ion manipulation methods

For a frequency measurement of a stored particle in a Penning trap, the eigenmotions have to be controlled and manipulated. The motional amplitudes are manipulated or excited by the application of an rf electric field on the ring electrode. The interaction of a dipolar or quadrupolar electric field with the ion is described in this section. A dipolar excitation field at the frequency ω_i manipulates the eigenmode i while a quadrupolar excitation field at $(\omega_i + \omega_k)$ leads to a coupling of the modes i and k. For a centering of the ion in the Penning trap the motional modes are usually cooled by collisions with the buffer gas. The buffer gas cooling technique will be described in this section, as well.
It should be mentioned that also other excitation types like a parametric excitation [27, 28] or an octupolar excitation field can be used to manipulate the eigenmotions [29].

The interaction of the particle with an external excitation electric field is described by a force, $\vec{F}(t) = q\vec{E}_{\mathrm{exc}}(t)$, which is added to the equation of motion in (2.1) of a particle in a Penning trap.

2.2.1 Azimuthal dipolar excitation method

The dipolar excitation field is described as a linear oscillating homogeneous field which changes the ions eigenmotion depending on the drive frequency ω_{exc}, the excitation amplitude U_{exc} and the initial phase ϕ_{exc}. This phase is given by the difference of the phase of the ion with respect to the excitation field. The linear polarized excitation field in the (x,y)-plane is written as

$$\vec{E}_{\mathrm{exc}} = \frac{U_{\mathrm{exc}}}{a_0}\cos(\omega_{\mathrm{exc}}t + \phi_{\mathrm{exc}}) \begin{pmatrix} 1 \\ 0 \end{pmatrix}, \tag{2.28}$$

where a_0 is a geometry parameter of the trap. Figure 2.3 (a) shows the excitation geometry using four out of eight segments of a cylindrical ring electrode to create a dipolar excitation field. An excitation signal $-U_{\mathrm{exc}}(t)$ is applied to the excitation segments $S_{\mathrm{exc},1}$ and $S_{\mathrm{exc},2}$ while a signal with phase shift of π is applied to the opposite segments $S_{\mathrm{exc},3}$ and $S_{\mathrm{exc},4}$. For a resonant excitation at $\omega_{\mathrm{exc}} = \omega_{\pm}$, the cyclotron and magnetron radii, R_+ and R_-, respectively, are calculated as

$$R_{\pm} = \frac{U_{\mathrm{exc}}}{a_0}\frac{q/m}{2(\omega_+ - \omega_-)}\sqrt{\tau_1^2 \mp \frac{2\tau_1 \sin(\omega_{\pm}\tau_1)\cos(\omega_{\pm}\tau_1)}{\omega_{\pm}}}, \tag{2.29}$$

which are in first order proportional to the product of the excitation time τ_1 and the excitation amplitude U_{exc}. In second order the radii are modulated by small oscillations due to the linear polarized excitation field. The initial phase difference, $\Delta\phi = \phi_{\mathrm{exc}} - \phi_{ion}$, has to be taken into account if the initial radii are non-zero. First the cyclotron radius R_+ is regarded. For $\Delta\phi = 0$, the R_+ is directly increased linear in time. If the phase difference is $0 < \Delta\phi \leq \pi/2$, the cyclotron radius is slowly increased in the beginning and then continues linear. For $\pi/2 < \Delta\phi \leq \pi$ the radius R_+ is first decreasing in the beginning and then increasing linear. For the case $\Delta\phi = \pi$ the radius R_+ is first decreasing to zero at the beginning and then increasing linear with the time. When taking the magnetron radius R_-, exactly the opposite behaviour is observed.
It should be noted that the magnetron and cyclotron radii increase both with the same rate. The excitation can be equivalently described by the electric excitation field perpendicular to the magnetic field which lead to a radial drift of the ion with the velocity $\vec{\mathrm{v}} = \vec{E} \times \vec{B}/|B|^2$. The ion will drift out of the trap center leading to an increase of the radii $R_{\pm}$.

For the experiments performed at the setup presented here a dipolar excitation pulse with a duration of τ_1 of the following form is applied:

$$rect\left(\frac{t}{\tau_1}\right) = \begin{cases} 1, & \text{for } |t| \leq \tau_1/2, \\ 0, & \text{otherwise} \end{cases} . \tag{2.30}$$

The excitation signal in the frequency domain is described by the convolution of the Fourier transform of the excitation signal $U_{\mathrm{exc}}(t)$ and a rectangular function [30, 31]

$$U(t) = U_{\mathrm{exc}}(t) \times rect\left(\frac{t}{\tau_1}\right) \Rightarrow \mathscr{F}(\omega) = \mathscr{F}(U_{\mathrm{exc}})(t) * \frac{\sin(\omega_{\mathrm{exc}}\tau_1/2)}{(\omega_{\mathrm{exc}}\tau_1/2)} \tag{2.31}$$

where the Fourier transform of the rectangular function results in a sinus cardinalis. The application of a sinusoidal signal at ω_{exc} with an excitation time τ_1 modulates the magnetron radius R_- and cyclotron radius R_+, respectively. The following line shapes are observed

$$R_\pm = \frac{U_{\mathrm{exc}}\tau_1}{\rho_0}\frac{q/m}{(\omega_+ - \omega_-)}\left|\frac{\sin((\omega_{\mathrm{exc}} - \omega_\pm)\tau_1/2)}{(\omega_{\mathrm{exc}} - \omega_\pm)\tau_1/2}\right| \tag{2.32}$$

where the modulation is described by the detuning $\omega_{\mathrm{exc}} - \omega_\pm$. In the frequency domain a symmetric distribution of frequencies around ω_{exc} is observed if the excitation duration is fixed.

The line shape described in Eq. (2.32) is used to determine the eigenfrequency by a fit to the data.

The full-width at half-maximum (FWHM) of the line shape in Eq. (2.32), defined as the line-width $\Delta\nu$, is found by a Taylor expansion of the sinc-function

$$\Delta\nu \approx \frac{1.2}{\tau_1}. \tag{2.33}$$

This equation is known as the Fourier limit. In some cases the square of the line shape in Eq. (2.32) is measured. The FWHM of the central peak is then given by $\Delta\nu \approx \frac{0.9}{\tau_1}$. The Fourier limit states that the excitation time τ_1 limits naturally the line-width of the central peak.

2.2.2 Azimuthal quadrupolar excitation method

For mass determinations of short-lived nuclei, the quadrupolar method is one of the most powerful techniques used in Penning-trap mass spectrometry. For an azimuthal excitation field, an interconversion between the magnetron and the cyclotron motion is achieved at the sideband frequency $\omega_c = \omega_+ + \omega_-$.

The interconversion of the radial modes of an ion occurs due to its interaction with a

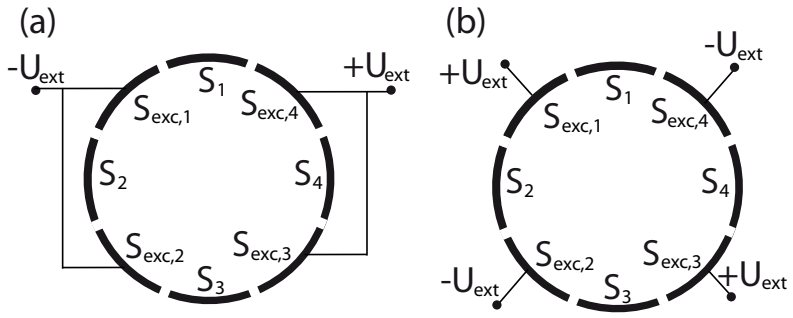

Figure 2.3: Side view of the eight-segmented ring electrode where alternately an excitation $S_{\mathrm{exc},i}$ and a detection electrode S_i are used. The geometries for creating a dipolar (a) or quadrupolar (b) field when applying an rf excitation signal $\pm U_{\mathrm{exc}}(t)$ are shown.

quadrupolar rf-potential. This potential is a solution of the Laplace equation in a source free Penning trap and it is given by [32]

$$\Phi_{\mathrm{exc}} = \frac{U_{\mathrm{exc}}}{a_0^2}\cos(\phi(t))(x^2-y^2) = \frac{U_{\mathrm{exc}}}{a_0^2}\cos(\phi(t))r^2\cos(2\varphi), \tag{2.34}$$

where $\phi(t) = \omega_{\mathrm{exc}}t + \chi_{\mathrm{exc}}$ is the phase of the external field and U_{exc} is the excitation amplitude. Such a field is created by applying an rf excitation signal on the excitation segments as shown in Fig. 2.3 (b). This field has a 2φ-symmetry. The spatial part of Eq. (2.34) is transformed into polar coordinates using the classical amplitudes of the eigenmodes given in Eq. (2.13) $u = x + iy$ as follows

$$r^2\cos(2\varphi) = Re(u^2) = Re(A_+^2 e^{-i2\omega_+ t} + A_-^2 e^{-i2\omega_- t} + 2A_+A_- e^{-i\omega_c t}). \tag{2.35}$$

The last term has to be inserted in Eq. (2.34). Then the equation contains very fast oscillating contributions which approximately average out to zero. The rotating wave approximation leads to three important situations, namely $\omega_{\mathrm{exc}} \approx 2\omega_+$, $\omega_{\mathrm{exc}} \approx 2\omega_-$ and $\omega_{\mathrm{exc}} \approx \omega_c$. A resonant quadrupolar excitation field at one of these frequencies will influence the motional modes of the ion.

The interpretation of the interconversion of the radial modes due to a quadrupolar field is done in the quantum mechanical framework. Here we regard the interconversion of the modes at the sideband frequency $\omega_{\mathrm{exc}} \approx \omega_c$ as described in [17, 32]. The effective Hamiltonian for the interconversion of the modes of one stored ion will be derived in the following.

First a coherent state $|\alpha_\pm\rangle$ is defined. This is a quantum mechanical state of the harmonic oscillator whose dynamics follow the classical harmonic oscillator. The Gaussian wave packet solution of the harmonic oscillator follows the classical trajectory without spreading. These states are the best approximation to the classical mechanics and have a minimal

uncertainty. They are given by [33]

$$|\alpha_\pm\rangle = e^{-|\alpha_\pm|^2/2} \sum_{n=0}^{\infty} \frac{\alpha_\pm^n}{n!} \hat{a}_\pm^{\dagger n}(0)|0\rangle \tag{2.36}$$

where $|0\rangle$ is the oscillator ground state and $\hat{a}_+^\dagger(0)$ and $\hat{a}_-^\dagger(0)$ are the creation operators for the oscillator quanta of the cyclotron and magnetron modes, respectively. In general, the coherent state is a normalized eigenstate of the harmonic oscillator annihilation operator $\hat{a}_\pm$ with a complex eigenvalue $\alpha_\pm$, i.e. $\hat{a}_\pm|\alpha_\pm\rangle = \alpha_\pm|\alpha_\pm\rangle$. The complex numbers $\alpha_\pm = \alpha_\pm(0)$ in Eq. (2.36) define the initial position and velocity of the ion at $t = 0$ time. Thus the coherent state in Eq. (2.36) defines the classical description of the ion motion in a trap. The time dependence of the complex oscillator amplitude is calculated from the expectation values of the annihilation operator $\hat{a}_+(t)$ and $\hat{a}_-(t)$

$$\alpha_\pm(t) = \langle\alpha_\pm|\hat{a}_\pm(t)|\alpha_\pm\rangle \tag{2.37}$$

with respect to the quasi-classical coherent state $|\alpha_\pm\rangle$. The expectation values $\alpha_\pm(t)$ defined in Eq. (2.37) are interpreted as the classical oscillator amplitudes $u = x + iy$, defined in Eq. (2.13). The Cartesian coordinates are related to the expectation values as follows

$$x + iy = A(\alpha_+ + \alpha_-^*) \tag{2.38}$$

where A is a normalization constant given by $A = \sqrt{2\hbar/(m\omega_1)}$, where $\hbar$ is the Planck's constant and the asterisk denotes the complex conjugate. The spatial part of the quadrupolar potential in Eq. (2.34) can be expanded:

$$\begin{aligned} 2\left(x^2 - y^2\right) &= (x+iy)^2 + (x-iy)^2 \\ &= A^2\left(\alpha_+^2 + \alpha_+^{*2}\right) + A^2\left(\alpha_-^2 + \alpha_-^{*2}\right) + 2A^2\left(\alpha_+^*\alpha_- + \alpha_-^*\alpha_+\right). \end{aligned} \tag{2.39}$$

Inserting the decomposition given in Eq. (2.39) into the quadrupolar potential given in Eq. (2.34) and using the rotating wave approximation, the potential energy can be written as

$$q\Phi_{\text{exc}} = \hbar g\left(e^{-i\phi(t)}\left(\alpha_+^{*2} + \alpha_-^2 + \alpha_+^*\alpha_-\right) + e^{i\phi(t)}\left(\alpha_+^2 + \alpha_-^{*2} + \alpha_-^*\alpha_+\right)\right) \tag{2.40}$$

where g is the coupling parameter given by $g = \frac{qU_{\text{exc}}}{2m\omega_1\rho_0^2}$. The coupling parameter g depends on the geometry of the trap and is proportional to the amplitude U_{exc} of the quadrupolar electric field.

An interpretation of Eq. (2.40) in the quantum mechanical context is possible if we consider Eq. (2.40) as an operator equation (when $\alpha_\pm$ and $\alpha_\pm^*$ are replaced by the annihilation operators $\hat{a}_\pm$ and creation operators $\hat{a}_\pm^*$, respectively). The first term α_+^{*2} in the first part of

Eq. (2.40) represents the creation of two modified cyclotron quanta and is interpreted as an absorption of one photon with the energy $\hbar\omega_{\mathrm{exc}} \approx 2\hbar\omega_+$ from the quadrupolar field. The second term α_-^2 describes transitions in which one photon of the energy $\hbar\omega_{\mathrm{exc}} \approx 2\hbar\omega_-$ is absorbed from the quadrupolar field and two excitation quanta of the magnetron mode are annihilated. Both terms do not affect the other mode. The last term describes the conversion of a magnetron quantum into a cyclotron quantum by simultaneous absorption of a photon with the energy $\hbar\omega_{\mathrm{exc}} \approx \hbar\omega_{\mathrm{c}}$. This leads to an annihilation of a quantum $\hbar\omega_-$ of the magnetron mode and a creation of a quantum $\hbar\omega_+$ of the cyclotron mode. The last three terms describe the inverse transitions.
For this work the interconversion of modes at the resonance frequency $\omega_{\mathrm{exc}} \approx \omega_{\mathrm{c}}$ is highly important. The effective Hamiltonian for the interaction of an ion with the quadrupolar field is reduced to

$$H_{\mathrm{exc}}(t) = \hbar g \left(e^{-i\phi(t)} \alpha_+^*(t)\alpha_-(t) + e^{i\phi(t)} \alpha_-^*(t)\alpha_+(t) \right). \tag{2.41}$$

It is interesting to translate the decomposition given in Eq. (2.39) back into cylindrical coordinates and velocities:

$$\alpha_+^2 = \frac{e^{2i\varphi}}{(A\omega_1)^2} \left(r^2(\omega_- + \dot{\varphi})^2 - 2ir\dot{r}(\omega_- + \dot{\varphi}) - \dot{r}^2 \right), \tag{2.42}$$

$$\alpha_-^{*2} = \frac{e^{2i\varphi}}{(A\omega_1)^2} \left(r^2(\omega_+ + \dot{\varphi})^2 - 2ir\dot{r}(\omega_+ + \dot{\varphi}) - \dot{r}^2 \right), \tag{2.43}$$

$$\begin{aligned} 2\alpha_+\alpha_-^* = \frac{e^{2i\varphi}}{(A\omega_1)^2} & \left(-2r^2(\omega_+ + \dot{\varphi})(\omega_- + \dot{\varphi}) \right. \\ & \left. + 2ir\dot{r}(\omega_+ + \omega_- + 2\dot{\varphi}) + 2\dot{r}^2 \right). \end{aligned} \tag{2.44}$$

The classical interaction of the ion with the quadrupolar field is calculated by inserting Eq. (2.44) and its complex conjugate into Eq. (2.41). We obtain a velocity-dependent classical interaction that would be difficult to motivate by classical arguments, but which appears very natural from the quantum mechanical point of view. It should be pointed out that the treatment of the interconversion of motional modes is purely classical except for the motivation of the effective interaction.

The time evolution of the amplitudes during the interconversion process is described by the Hamiltonian

$$H(t) = \hbar\omega_+ \left(\alpha_+^*(t)\alpha_+(t) + \frac{1}{2} \right) - \hbar\omega_- \left(\alpha_-^*(t)\alpha_-(t) + \frac{1}{2} \right) + H_{\mathrm{exc}}(t), \tag{2.45}$$

which is the sum of the radial Hamiltonian and the effective interaction Hamiltonian given in Eq. (2.41). The Heisenberg's equation of motion for classical amplitudes of magnetron

$\alpha_-(t)$ and cyclotron $\alpha_+(t)$ amplitudes can be calculated as

$$\dot{\alpha}_+(t) = -i\omega_+\alpha_+(t) - ige^{-i(\omega_{\rm exc}t+\chi_{\rm exc})}\alpha_-(t) \quad (2.46)$$

$$\dot{\alpha}_-(t) = +i\omega_-\alpha_-(t) - ige^{+i(\omega_{\rm exc}t+\chi_{\rm exc})}\alpha_+(t) \quad (2.47)$$

with the following solutions

$$\alpha_+(t) = e^{-i(\omega_+ +\delta/2)t}\left[\left(\cos\frac{\omega_{\rm R}t}{2} + i\frac{\delta}{\omega_{\rm R}}\sin\frac{\omega_{\rm R}t}{2}\right)\alpha_+(0) - i\frac{2g}{\omega_{\rm R}}\sin\frac{\omega_{\rm R}t}{2}e^{-i\chi_{\rm exc}}\alpha_-(0)\right], \quad (2.48)$$

$$\alpha_-(t) = e^{+i(\omega_- +\delta/2)t}\left[-i\frac{2g}{\omega_{\rm R}}\sin\frac{\omega_{\rm R}t}{2}e^{+i\chi_{\rm exc}}\alpha_+(0) + \left(\cos\frac{\omega_{\rm R}t}{2} - i\frac{\delta}{\omega_{\rm R}}\sin\frac{\omega_{\rm R}t}{2}\right)\alpha_-(0)\right] \quad (2.49)$$

where $\delta = \omega_{\rm exc} - \omega_{\rm c}$ is the detuning of the quadrupolar field with respect to the resonance frequency $\omega_{\rm c}$ and the frequency of the interconversion

$$\omega_{\rm R} = \sqrt{4g^2+\delta^2}. \quad (2.50)$$

$\omega_{\rm R}$ is known as the Rabi frequency, which is associated with the interconversion of modes due to the coupling of the quadrupolar field with the ion. Thus for a stronger coupling parameter g a larger frequency of interconversion is observed. The instantaneous cyclotron and magnetron radii are calculated from the complex oscillator amplitudes $\alpha_\pm(t)$

$$R_\pm(t) = \sqrt{\frac{2\hbar}{m\omega_1}}|\alpha_\pm(t)| = \sqrt{\frac{2\hbar\langle N_\pm(t)\rangle}{m\omega_1}}. \quad (2.51)$$

The cyclotron radius R_+ and the magnetron radius R_- are the observables accessible in the experiment. The explicit expression for the radii is given by [32, 34]

$$R_\pm^2(t) = \left(\cos^2\frac{\omega_R t}{2} + \frac{\delta^2}{\omega_R^2}\sin^2\frac{\omega_R t}{2}\right)R_\pm^2(0) + \frac{4g^2}{\omega_R^2}\sin^2\frac{\omega_R t}{2}R_\mp^2(0) \pm 2\frac{2g}{\omega_R}\sin\frac{\omega_R t}{2}\left(\cos\frac{\omega_R t}{2}\sin\Delta - \frac{\delta}{\omega_R}\sin\frac{\omega_R t}{2}\cos\Delta\right)R_+(0)R_-(0), \quad (2.52)$$

where $\Delta = \chi_+ + \chi_- - \chi_{\rm exc}$ is the phase difference between the radial ion motions and the excitation field, and where $R_\pm(0)$ are the initial cyclotron and magnetron radii, respectively. The phase Δ has no influence on the interconversion of modes if either the initial magnetron or the initial cyclotron radii is zero.

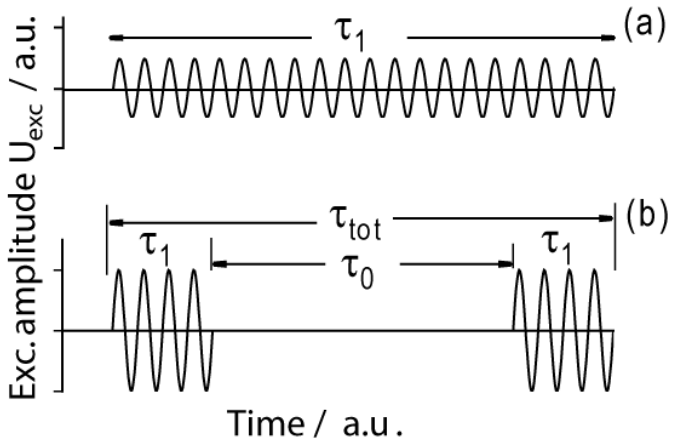

Figure 2.4: Excitation schemes of the one-pulse quadrupolar rf field with an excitation time τ_1 (a) and two-pulse (Ramsey) quadrupolar rf field (b). Note that the coupling strength g is proportional to the excitation amplitude U_{exc}. The Ramsey scheme uses two identical pulses with a duration τ_1 which are separated by a waiting time τ_0. The total time is $\tau_{\mathrm{tot}} = 2\tau_1 + \tau_0$.

The expectation values for the number of quanta in the cyclotron and magnetron oscillators are defined as $\langle N_{\pm}(t)\rangle$. The total number of quanta $\langle N_{\mathrm{tot}}\rangle$ in the system is conserved during the interaction with the quadrupolar field and given by

$$\langle N_{\mathrm{tot}}(t)\rangle = \langle N_{\mathrm{tot}}(0)\rangle = \langle N_{+}(t)\rangle + \langle N_{-}(t)\rangle = \frac{m\omega_1}{2\hbar}\left(R_{+}^2(t) + R_{-}^2(t)\right). \tag{2.53}$$

This means that the total number of quanta is at any time equal to the sum of the quanta in the magnetron and cyclotron modes. Let's assume that the ion motion at time zero, $t = 0$, is a pure magnetron motion. Then from Eq. (2.53) follows that the sum of the squares of the cyclotron and magnetron radii is equal to the square of the initial magnetron radius, i.e. $R_{+}^2(t) + R_{-}^2(t) = R_{-}^2(0)$.
For a mass determination, the conversion from a pure magnetron motion into a pure cyclotron motion is performed, i.e., the initial conditions are $R_{+}(0) = 0$ and $R_{-}(0) \neq 0$. Then the fraction $n_{+}(t) = R_{+}^2(t)/R_{-}^2(0)$ varies between 0 and 1. This definition is used to calculate the profile functions for the one- and two-pulse (Ramsey) excitation schemes. Both excitation schemes are illustrated in Fig. 2.4.

The one-pulse excitation scheme: Figure 2.4 (a) shows a one-pulse excitation scheme with a duration time τ_1 and an amplitude g. We assume that the initial state of the ion is a pure magnetron motion at $t = 0$. Then the interaction of the ion with a quadrupolar rf

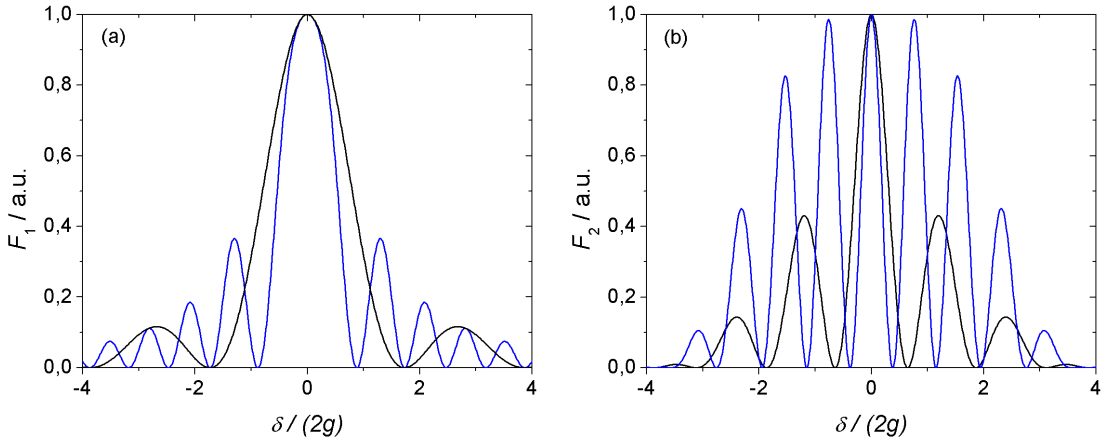

Figure 2.5: The one- and two-pulse profile function as a function of the detuning normalized to the coupling parameter $\delta/(2g)$. (a) One-pulse profile function for $\tau_1 = 1\tau_c$ (black curve) and $\tau_1 = 3\tau_c$ (blue curve). (b) Two-pulse profile function for $\tau_1 = 0.5\tau_c$ with a waiting time of $\tau_0 = \tau_c$ (black curve) and $\tau_0 = 2\tau_1$ (blue curve).

field with a detuning δ leads to the profile function

$$F_1(\tau_1, \delta, g) = \frac{R_+^2(\tau_1)}{R_-^2(0)} = \frac{4g^2}{4g^2 + \delta^2} \sin^2\left(\frac{\omega_R \tau_1}{2}\right). \tag{2.54}$$

Figure 2.5 (a) shows the one-pulse profile function as a function of $\delta/(2g)$ for a pulse duration of $\tau_1 = 1\tau_c$ and $\tau_1 = 3\tau_c$. The conversion time τ_c is defined as a full conversion from an initial magnetron state into the cyclotron state or vice versa for an excitation at the resonance frequency ($\omega_{exc} = \omega_c$). The conversion time is then $\tau_c = \pi/(2g)$. A conversion back to the initial state is reached after the Rabi period $\tau_R = 2\tau_c = \pi/g$.

Experimentally the conversion profile is obtained by measuring the cyclotron radius R_+ as a function of the detuning $\delta/2\pi$. The FT-ICR method gives directly access to R_+, which is determined from the Fourier amplitude at the eigenfrequency ω_+ as described in Section 2.3.3.

The mass resolving power $\mathscr{R}$ obtained with the application of a one-pulse quadrupolar field with a time length τ_1 is given by

$$\mathscr{R} = \frac{m}{\Delta m} = \frac{\omega_c}{\Delta\omega_c} \approx 0.9 \nu_c \tau_1 \tag{2.55}$$

where $\Delta\omega_c$ is the FWHM of the profile function. The last approximation is the so-called Fourier limit. Thus a shorter excitation time will result in a broader frequency range. Therefore, if short-lived nuclides are measured, the half-life of the nuclides limits the resolving power.

The two-pulse excitation scheme: The two-pulse excitation scheme was invented by Norman F. Ramsey [18, 19] and is nowadays a standard technique applied in Penning-trap mass spectrometry because the sideband frequency $(\nu_+ + \nu_-)$ is determined with a higher precision compared to the conventional one-pulse excitation scheme [35, 36]. As shown in Fig. 2.4 (b), the excitation scheme consists of two phase coherent excitation pulses, i.e. two excitation pulses with same duration τ_1 and same amplitude g, which are separated by a waiting time τ_0. It should be noted that a fixed phase relation between the two pulses is needed. The Heisenberg's equations of motion of the cyclotron amplitude (2.46) and the magnetron amplitude (2.47) have to be solved for the three time intervals. The profile function of the two-pulse quadrupolar excitation scheme for the conversion of a pure magnetron state into cyclotron motion is calculated as [32]

$$F_2(\delta, \tau_0, \tau_1, g) = \frac{R_+^2(\tau_{\text{tot}})}{R_-^2(0)} \tag{2.56}$$

$$= \frac{16\,g^2}{\omega_{\text{R}}^2} \sin^2\left(\frac{\omega_{\text{R}}\tau_1}{2}\right) \cdot \left[\cos\left(\frac{\delta\tau_0}{2}\right)\cos\left(\frac{\omega_{\text{R}}\tau_1}{2}\right) - \frac{\delta}{\omega_{\text{R}}}\sin\left(\frac{\delta\tau_0}{2}\right)\sin\left(\frac{\omega_{\text{R}}\tau_1}{2}\right)\right]^2$$

where the total time is $\tau_{\text{tot}} = 2\tau_1 + \tau_0$. Figure 2.6 (a) to (d) show the evolution of the classical ion trajectory for a two-pulse excitation done at resonant excitation at ω_{c} with a duration of $\tau_1 = \tau_{\text{c}}/2$ and a waiting time τ_0. A conversion of a pure magnetron motion into a pure cyclotron motion is observed. After the first excitation pulse the magnetron and cyclotron radii are equal and evolve afterwards for the waiting time. After the second excitation pulse the ion motion is converted into a pure cyclotron motion, which has the same radius as the initial magnetron motion.

Figure 2.5 (b) shows the two-pulse profile function as a function of $\delta/(2g)$ for an excitation time $\tau_1 = 0.5\tau_{\text{c}}$ and two waiting times, $\tau_0 = \tau_{\text{c}}$ and $\tau_0 = 2\tau_1$, respectively. The bracket term in Eq. (2.56) modulates the function with respect to the detuning δ. As seen from Fig. 2.5 (b) more sidebands around the center frequency occur for a longer total excitation time τ_{tot}. The FWHM of the conversion profile is decreased by a factor of 1.6, when increasing the total time from $1\tau_{\text{c}}$ to $3\tau_{\text{c}}$. More explanations will be given in Section 5.2 where experimental data are compared with the profile given in function Eq. (2.56).

2.2.3 Buffer gas cooling of the ion motion

After the injection of the ions in the Penning trap, the kinetic energy is often too large. In order to reduce the ion energy G. Savard et al. [37] invented a relatively fast cooling

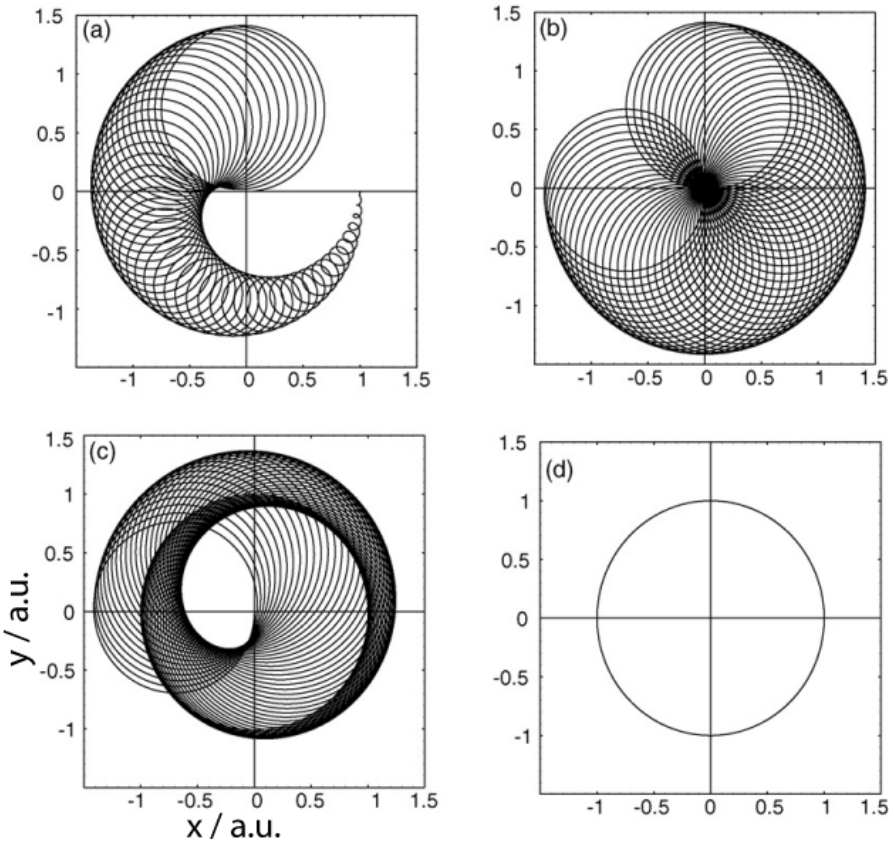

Figure 2.6: Ion trajectory for a two-pulse Ramsey excitation scheme at the resonance frequency ($\omega_{exc} = \omega_c$). In this scheme arbitrary units (a.u.) are used. The excitation time for each pulse is $\tau_1 = \tau_c/2$ and the initial mode is a pure magnetron motion with $R_-(0) = 1$. (a) During the first excitation pulse, the magnetron radius is reduced while the cyclotron radius increases. After a duration of a half conversion time the magnetron and cyclotron radii are equal, i.e. $R_-(\tau_1/2) = R_-(0)/\sqrt{2}$. (b) During the waiting time τ_0 the ion motion follows the trajectory which is a superposition of magnetron and cyclotron motions. (c) During the second excitation pulse of time length $\tau_1 = \tau_c/2$ the magnetron motion is completely converted into the cyclotron motion. (d) After the second pulse the ion performs a pure cyclotron motion with cyclotron radius $R_+(\tau_1) = R_-(0)$, thus a full conversion from the magnetron into the cyclotron motion is observed.

technique. This method is commonly used in Penning-trap mass spectrometry for short-lived nuclides and has an advantage that it can be applied to a wide mass range.

The axial and cyclotron energy are reduced or cooled when the stored ions make collisions with a present buffer gas. The cooling can be described by a damping force $\vec{F}_\mathrm{d}$ which is proportional to the momentum of the ions with mass m and velocity v

$$\vec{F}_\mathrm{d} = -\delta m\vec{\mathrm{v}}, \tag{2.57}$$

where the damping coefficient δ is given by [34]

$$\delta = \frac{q}{m}\frac{1}{M_\mathrm{ion}}\frac{p/p_\mathrm{N}}{T/T_\mathrm{N}}. \tag{2.58}$$

Here M_ion is the reduced ion mobility at a pressure p and temperature T referenced to the normal pressure $p_\mathrm{N} = 1,01325\,\mathrm{bar}$ and temperature $T_\mathrm{N} = 273,15\,\mathrm{K}$. The motional radii depend exponentially on the damping coefficient, $R_\pm(t) = R_\pm(t_0)e^{\mp\alpha_\pm t}$, with $\alpha_\pm = \mp\delta\omega_\pm/(\omega_+ - \omega_-)$. The cyclotron radius decreases with time, while the magnetron radius simultaneously increases. This is due to the fact that the magnetron motion is unstable (see Section 2.1.1). Notice that due to the hierarchy $\omega_+ > \omega_-$, the cyclotron motion decreases much faster than the magnetron radius increases.
A reduction of the magnetron radius can be achieved when the magnetron motion is converted into the cyclotron motion by applying a quadrupolar excitation field at $\omega_\mathrm{exc} = \omega_\mathrm{c}$. When using simultaneously buffer gas, the cyclotron radius decreases with time which leads to a centering of the ions. The parameters like buffer gas pressure, excitation amplitude and time have to be chosen such that the ions of interest will be centered. When more than one ion specie are simultaneously trapped, this cooling process leads to a mass selection since the cyclotron frequency depends on the ion mass.

2.3 Ion detection techniques

For the determination of the cyclotron frequency ω_c by using a one- or a two-pulse quadrupolar excitation field, the cyclotron radius has to be measured as a function of the detuning δ (see Eq. (2.54) and Eq. (2.56)). In Penning-trap mass spectrometry (MS) two detection methods can be used for measuring the conversion profiles.
First, a destructive time-of-flight (TOF) detection method is described, where the ion is lost after detection. The flight-time of the particle from the trap to the detector is measured as a function of the detuning. This method is applied in high-precision mass measurements on short-lived nuclides.
Secondly, the non-destructive FT-ICR detection method allows to measure the image

charges induced by the trapped ions on the detection surface. A Fourier transformation of the induced current leads to the determination of the eigenfrequencies of the ions. This technique was developed in chemistry, nowadays well-known as broad-band FT-ICR MS [14] where a mass resolving power of 10^6 with a precision of 1 ppm is sufficient for mass identification [13, 38]. For high-precision measurements of stable nuclides, a narrow-band detection circuit is used which is sensitive to one stored ion. Such mass spectrometers are used to measure the g-factor of atomic systems [39], or for applications like metrology, fundamental physics and weighing chemical bonds [40, 41].

2.3.1 Destructive time-of-flight detection

The interconversion between the magnetron and the cyclotron modes due to the application of a quadrupolar excitation field leads to a change of the radial energy E_{rad} depending on the detuning. The cyclotron and magnetron motions of a trapped ion in a magnetic field B have a magnetic moment $\vec{\mu} = -E_{\mathrm{rad}}/B\vec{e}_z$ in the z-direction which depends mainly on the kinetic energy of the cyclotron mode, i.e. $E_{\mathrm{rad}} \approx mR_+^2\omega_+^2/2$ (see Eq. (2.19)). For the detection, the ion is ejected from the center of the Penning trap to the detector, which is placed outside the strong magnetic field, as seen in Fig. 2.7 (a). The coupling of the gradient of the magnetic field to the adiabatic invariant magnetic moment $\vec{\mu} = \mu_z\vec{e}_z$ leads to an axial force

$$\vec{F} = -\vec{\mu}\cdot\nabla\vec{B} = -\frac{E_{\mathrm{rad}}}{B}\frac{\partial B}{\partial z}\vec{e}_z. \tag{2.59}$$

This force is directed towards the detector and is proportional to the radial energy. The ion's time-of-flight T from the trap center at position $z = 0$ to the detector at z_{det} depends on the detuning δ

$$T(\delta) = \int_0^{z_{\mathrm{det}}} \mathrm{d}z \sqrt{\frac{m}{2[E_0 - qV(z) - \mu(\delta)(B(z) - B(0))]}}, \tag{2.60}$$

where E_0 is the initial kinetic energy of the ion at the position $z = 0$, and $V(z)$ the potential and $B(z)$ the magnetic field along the ion path from the trap center to the detector, respectively. Notice that E_0 is independent of the detuning, since it has contributions of the initial axial energy, from the electric and magnetic fields. Figure 2.7 (b) shows a TOF resonance curve for a one-pulse quadrupolar excitation field as a function of the detuning. For a quadrupolar excitation at ω_{c} with a pulse duration equal to the conversion time the magnetic moment has a maximum value because the ion performs a pure cyclotron motion. Thus, the ion energy E_0 is maximized, which leads to the shortest TOF compared to any mixed motion. For an off-resonant excitation the motion is a superposition of magnetron and cyclotron motions, thus the TOF is longer than at the resonance case.

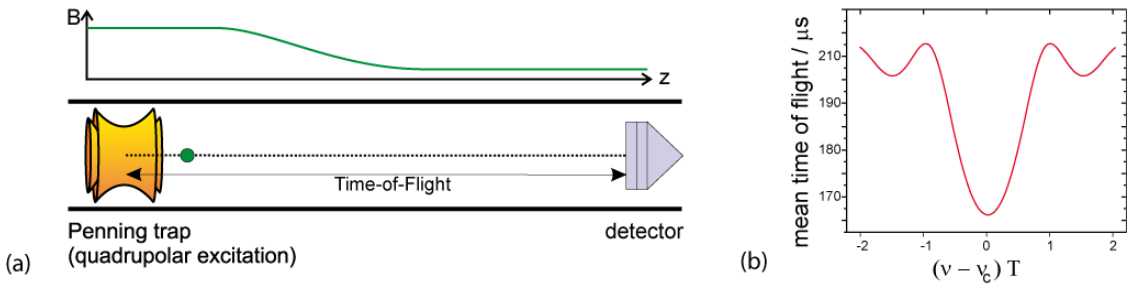

Figure 2.7: (a) Schematic view of the time-of-flight detection technique. The Penning trap is placed in a strong magnetic field while the detector is placed outside the magnetic field. The time-of-flight of the ions from the trap to the detector depends on the initial azimuthal energy of the ions. (b) A typical time-of-flight resonance as a function of the detuning $\nu - \nu_c$ is shown. For further details see text. Plot taken from [42].

The statistical uncertainty of a TOF measurement is inversely proportional to the mass resolving power and the square root of the number of detected ions [43]

$$\left(\frac{\delta m}{m}\right) \propto \frac{1}{\mathscr{R}\sqrt{N_{ion}}}. \tag{2.61}$$

Notice that the mass resolving power $\mathscr{R}$, defined in Eq. (2.55), is limited by the half-life of the nuclides.

2.3.2 Non-destructive ion image charge detection

The broad-band FT-ICR detection method is a non-destructive method which was introduced by Comisarow and Marshall in 1974 [14]. The moving particles induce image charges on the surface of the detection electrodes of the trap. These electric charges can be derived in form of a Fourier series for each detection segment. The Fourier components at the frequencies $m_+\nu_+ + m_-\nu_-$, where m_+ and m_- are integers, are calculated as a function of the motional radii R_+ and R_-. At the FT-ICR setup presented in this thesis the FT-ICR detection method is used. In order to interpret the observed FT-ICR signals a brief introduction for calculating these Fourier amplitudes will be presented.
Due to Gauss's Law, a particle with a charge q at a position $\vec{x}_0$ inside a volume will induce a charge $-q$ on the surface. However, in an open-endcap Penning trap the detection electrodes have a finite length and a finite opening angle. The induced charges are non-uniformly distributed over the surface S of the electrodes and depend on the ions position. The potential on the surface of a detection electrode is given by the Green's function satisfying the Dirichlet boundary value problem $G_D(\vec{x},\vec{x}') = 0$ for $\vec{x},\vec{x}' \in S$. The potential

inside the trap volume created by a charge q located at $\vec{x}_0$ is given by [44]

$$\Phi(\vec{x},\vec{x}_0) = qG_{\mathrm{D}}(\vec{x},\vec{x}_0), \tag{2.62}$$

where the Green's function G_{D} is known. The surface charge density σ induced by an ion at a position $\vec{x}_0$ on the detection surface S is given by the derivative normal to S

$$\sigma(\vec{x},\vec{x}_0) = \frac{1}{4\pi}\cdot\frac{\partial\Phi}{\partial n}\bigg|_{\vec{x}\in S} = \frac{q}{4\pi}\cdot\frac{\partial}{\partial n}G_{\mathrm{D}}(\vec{x},\vec{x}_0)\bigg|_{\vec{x}\in S}. \tag{2.63}$$

Only the electric field perpendicular to the detection electrode will give a contribution to the charge density. As shown in Fig. 2.3, four electrodes of the eight-fold segmented ring electrode are used for detection. The total charge $Q_i(\vec{x}_0)$ induced on the surface S_i of one detection electrode is given by an integration of the surface charge density σ over the surface S_i

$$Q_i(\vec{x}_0) = \int_{S_i} \mathrm{d}A\,\sigma(\vec{x},\vec{x}_0), \tag{2.64}$$

where the surface element is defined as $\mathrm{d}A = a\mathrm{d}\varphi\mathrm{d}z$.
The cylindrical geometry will be implemented by using a model of a cylinder with radius a_0 and length L. A rotational symmetry with respect to the z-axis is assumed. An analytical solution of the Green's function with Dirichlet boundary values for this cylinder in polar coordinates can be found in Ref. [45]. The Green's function is inserted in Eq. (2.63) and the surface charge density is calculated with Eq. (2.64). We assume that a point charge q located at the position $\vec{x}_0 = (r_0, \varphi_0, \xi_0)$ induces a surface charge on the detection element S_i. An angular and an axial integration over the surface element S_i result in the total image charge. The analytical expression without approximation is given by [46]

$$\begin{aligned} Q_i(\vec{x}_0) = \quad & q \quad \frac{8}{4\pi^2}\sum_{j=0}^{\infty}\frac{1}{2j+1}\sin\left(\frac{(2j+1)\pi}{2}\frac{z_r}{L}\right)\cos\left(\frac{(2j+1)\pi}{L}\xi_0\right) \\ & \times \quad \sum_{m=0}^{\infty}\phi_{i,m}(\varphi_0)\frac{\mathrm{I}_m((2j+1)\pi r_0/L)}{\mathrm{I}_m((2j+1)\pi a_0/L)}, \end{aligned} \tag{2.65}$$

where I_m are the modified Bessel functions, z_r is the length of the detection surface and the function $\phi_{i,m}(\varphi_0)$ is the angular integration of the i-th detection segment. This integration depends on the opening angle of the electrode.

2.3.3 Fourier amplitudes for FT-ICR ion detection

The trapped ions induce image charges $Q_i(\vec{x}_0)$ on the detection electrodes which is experimentally first recorded as a function of time. Then a Fourier transformation gives information about the periodic ion motion at certain frequencies. The image charges described

in Eq. (2.65) are not yet time dependent. The next step is to replace the ion position $\vec{x}_0$ by the time dependent classical amplitude $u(t)$ defined in Eq. (2.13). Thus the time dependent induced charge $Q_i(t)$ on the detection segment S_i is written in form of a Fourier expansion [46] with respect to the eigenfrequencies $\omega_+, \omega_-, \omega_z$ of the moving ion

$$Q_i(t) = -q \sum_{m_+} \sum_{m_-} \sum_{m_z} W^{(i)}_{m_+,m_-,m_z}(R_+,R_-,R_z) \cos(m_+\varphi_+(t) + m_-\varphi_-(t) + m_z\varphi_z(t) + \chi_{m_+,m_-,i}) \tag{2.66}$$

where $\chi_{m_+,m_-,i} = (m_+ + m_-)(i-1)\pi/2$, and m_+ and m_- are integers, and m_z is a positive or negative even integers. The Fourier coefficients $W^{(i)}_{m_+,m_-,m_z}(R_+,R_-,R_z)$ at the frequency $m_+\omega_+ + m_-\omega_- + m_z\omega_z$ depend on the magnetron radius R_-, the cyclotron radius R_+ and the axial amplitude R_z. The Fourier coefficients of the image charges given in Eq. (2.66) are the accessible observables in the experiment and are given by

$$W^{(i)}_{m_+,m_-,m_z}(R_+,R_-,R_z) = \sum_{m=0}^{\infty} \sum_{k=0}^{\infty} \sum_{l=0}^{\infty} \frac{1}{2}(1+\delta_{0,l})\delta_{m,m_++m_-}\delta_{2l,m_z} \\ c_{i,m}A_{m,k,l}(R_z)\frac{1}{a_0^{m+2k}} P^{m_+,m_-}_{m,k}(R_+,R_-), \tag{2.67}$$

where $m = m_+ + m_-$, the Kronecker symbol $\delta_{0,l}$ and the geometry coefficients $A_{m,k,l}(R_z)$, which depend on the axial amplitude R_z. The functions $P^{m_+,m_-}_{m,k}(R_+,R_-)$ are polynomials of degree $m+2k$ depending on R_+ and R_-, with $m = m_+ + m_- \geq 0$.
The dimensionless geometry coefficients $A_{m,k,0}$ are calculated for $m,k = 0,1,2$ of the Penning trap used within this thesis. These values are listed in Table 2.2 and the trap parameter are taken from [47]. The coefficients decrease roughly by a factor of 10 with increasing index k. When changing the index m only small changes occur. The coefficients $c_{i,m}$ are derived by the angular integration, thus they include the opening angle α of the electrodes and they are given for $m = 0$ by $c_{1,0} = c_{2,0} = c_{3,0} = c_{4,0} = \alpha$. For $m > 0$ they are given by $c_{1,m} = c_{2,m} = c_{3,m} = c_{4,m} = 4/m\sin(m\alpha)$.

For the FT-ICR detection, the most important Fourier amplitudes $W^{(i)}_{m_+,m_-,0}(R_+,R_-,0)$ at frequencies $m_+\omega_+ + m_-\omega_-$ are now presented, i.e. the Fourier amplitudes at different indexes m_+ and m_- are given. We assume that the ion has only a radial motion and no axial oscillation, i.e. $R_z = 0$. The index m_z is set to zero for the following calculations.

Fourier amplitude at the frequency ω_+: $(m = m_+ = 1, m_- = 0)$ In FT-ICR MS the mass determination of unknown ions is done by detecting the Fourier amplitude at the modified cyclotron frequency. This Fourier amplitude at ω_+ is given by

$$W^{(i)}_{1,0,0} = \frac{R_+}{a_0}\left(c_{i,1}A_{1,0} + \frac{1}{a_0^2}(R_+^2 + 2R_-^2)\cdot c_{i,1}A_{1,1} + \frac{1}{a_0^4}(R_+^4 + 6R_+^2R_-^2 + 3R_-^4)\cdot c_{i,1}A_{1,2} + \ldots\right),$$

$A_{m,k,0}$	$k=0$	$k=1$	$k=2$
$m=0$	0.12994	0.04114	0.00140
$m=1$	0.14182	0.02473	−0.00432
$m=2$	0.15011	0.01545	−0.00531

Table 2.2: Dimensionless geometry coefficients $A_{m,k,0}$ of the KATRIN Penning trap with parameters $\rho_0 = 35.5\,\mathrm{mm}$, $L = 236\,\mathrm{mm}$ and $z_r = 56\,\mathrm{mm}$ for $R_z = 0$.

(2.68)

which is in first order proportional to the cyclotron radius R_+. Thus, measurement of the Fourier component results in a direct measurement of the resonance shape for the cyclotron radius of a dipolar excitation pulse, as described in Eq. (2.32). Also, the one- and two-pulse profile functions for the quadrupolar excitation can directly be measured.

Fourier amplitude at the frequency ω_-: $(m = m_- = 1, m_+ = 0)$ The Fourier amplitude at ω_- is given by

$$W_{0,1,0}^{(i)} = \frac{R_-}{a_0}\left(c_{i,1}A_{1,0} + \frac{1}{a_0^2}(R_-^2 + 2R_+^2)\cdot c_{i,1}A_{1,1} + \frac{1}{a_0^4}(R_-^4 + 6R_+^2R_-^2 + 3R_+^4)\cdot c_{i,1}A_{1,2} + \ldots\right), \tag{2.69}$$

which is in first order proportional to the magnetron radius R_-. The determination of the magnetron frequency is in most of the experiments not directly possible because the noise level of the amplifier at these low frequencies is larger than the FT-ICR signal in the frequency spectrum itself. Notice that the detection of the magnetron motion leads to an energy dissipation from which an increase of the magnetron radius results.

Fourier amplitude at the frequency $\omega_+ + \omega_-$: $(m = 2, m_+ = m_- = 1)$ The Fourier amplitude at the magnetron sideband of the modified cyclotron frequency $\omega_+ + \omega_- = \omega_c$ is of high importance for FT-ICR MS, since it is directly linked to the mass of the stored ion species. The Fourier amplitude is only visible if the ion performs a magnetron and cyclotron motion

$$W_{1,1,0}^{(i)} = \frac{R_+R_-}{a_0^2}\left(2c_{i,2}A_{2,0} + \frac{3}{a_0^2}(R_+^2 + R_-^2)\cdot c_{i,2}A_{2,1} + \ldots\right). \tag{2.70}$$

The Fourier amplitude is proportional to the product of the magnetron and cyclotron radii. It should be noticed that the first order scales with a_0^{-2}.

Fourier amplitude at the frequency $\omega_+ - \omega_-$: $(m = 0, m_+ = 1, m_- = -1)$ The lower frequency sideband is also an observable in this study:

$$W^{(i)}_{1,-1,0} = \frac{R_+ R_-}{a_0^2}\left(2c_{i,0}A_{0,1} + \frac{4}{a_0^2}(R_+^2 + R_-^2)\cdot c_{i,0}A_{0,2} + ...\right). \tag{2.71}$$

The Fourier amplitude appears only when a magnetron and a cyclotron motion are present, similar to the Fourier amplitude at ω_c.

Fourier amplitude at the frequency $2\omega_+$: $(m = m_+ = 2, m_- = 0)$ The second harmonic of the modified cyclotron frequency $2\omega_+$ is in first order proportional to the square of the cyclotron radius

$$W^{(i)}_{2,0,0} = \frac{R_+^2}{a_0^2}\left(c_{i,2}A_{2,0} + \frac{1}{a_0^2}(R_+^2 + 3R_-^2)\cdot c_{i,2}A_{2,1} + ...\right). \tag{2.72}$$

Detection schemes: The calculation of the induced charges was performed for one detection segment S_i. The induced charges from each detection segment can be detected simultaneously. As shown in Fig. 2.3 the Penning trap has an eight-fold segmented ring electrode where four segments are used for detection. For reaching higher Fourier amplitudes two different detection schemes can be applied by using the image charges Q_i on each electrode: (i) The differential signal, $Q_d(t) = (Q_1 + Q_2) - (Q_3 + Q_4)$ (dipolar detection) and (ii) the sum signal $Q_q(t) = (Q_1 + Q_3) - (Q_2 + Q_4)$ (quadrupolar detection) are used as a detection scheme. The appearance of a Fourier amplitude for both detection schemes depends on the integer $m = m_+ + m_-$ [44].

For dipolar detection, the Fourier amplitudes occur for odd integers of m, i.e., signals at the modified cyclotron and magnetron frequencies $\omega_\pm$ with $m = 1$, signals at the higher harmonics of the modified cyclotron and magnetron frequencies $3\omega_\pm, ...$ with $m = 3$ and signals at magnetron sidebands of the modified cyclotron frequency $\omega_+ \pm 2\omega_-$ with $m = 3$ are observed. With the dipolar detection mostly the Fourier amplitude at ω_+ is measured. The image charges induced on the four detection electrodes are derived from Eq. (2.66) and Eq. (2.68) and the image charge in first order is given by

$$Q_d(t) = \frac{R_+}{a_0}A_{1,0}c_{i,0}2\sqrt{2}\cos\left[\varphi_+(t) + \frac{\pi}{4}\right]. \tag{2.73}$$

The Fourier coefficient at ω_+ is proportional to the cyclotron radius R_+.

For the quadrupolar detection, the Fourier amplitudes occur if m is an even integer, i.e., signals at the harmonics $2\omega_\pm$ with $m = 2$, $4\omega_\pm$ with $m = 4$ and at the magnetron sidebands of the modified cyclotron frequency $\omega_+ + \omega_-$ with $m = 2$ and $\omega_+ - \omega_-$ with $m = 0$ can be observed. In the quadrupolar detection the Fourier amplitude at the sideband frequency

$\omega_c = \omega_+ + \omega_-$ is important due to the direct charge-to-mass relation. The image charge in first order is given by

$$Q_q(t) = \frac{R_+ R_-}{a_0^2} A_{2,0} c_{i,2} \cdot 8 \cdot \cos\left[\varphi_+(t) + \varphi_-(t)\right]. \tag{2.74}$$

The observed Fourier amplitudes for both detection schemes are higher compared to the single segment detection. It should be mentioned that both detection methods are sensitive to a superposition of the cyclotron and the magnetron motions which leads to magnetron sidebands of the modified cyclotron frequency, as seen before.

2.3.4 Signal-to-noise ratio of a broad-band FT-ICR detection circuit

After exciting the ion motion, the charges induced by the ions on the detection electrodes are picked-up by a broad-band amplifier system consisting of two amplifiers. The amplifiers themselves have both of them a low-noise behaviour which increases the SNR. In this section e_n is the voltage noise density and i_n is the current noise density, i.e. the noise density is given per frequency interval.

Figure 2.8 shows the equivalent circuit of a broad-band detection system with two low-noise amplifiers. The noise sources of the first amplifier are characterized by the voltage noise density e_n and the current noise density i_n. The input resistance of the amplifier is R_i and its gain is defined by A_1. The input capacity of the amplifier and the capacity of the cables are added to the detector capacitance C_d.

The input current noise i_n flows through the input impedance $Z = (1/R_i + i\omega C_d)^{-1}$, which yields a noise voltage $i_n Z$. The thermal (Johnson) noise of the input resistance is due to the thermal velocity fluctuations of the charge carriers in the resistor at a temperature T. The spectral noise N_1 of the first amplifier is equal to the sum of the three noise sources in quadrature, since they are not correlated [48]

$$N_1^2 = e_n^2 + (i_n|Z|)^2 + 4k_B T|Z| \tag{2.75}$$

where k_B is the Boltzmann constant. The second amplifier has a noise source N_2 and a gain A_2. The total noise density at the output of the circuit shown in Fig. 2.8 is given by

$$N^2 = (N_1 A_1 A_2)^2 + (N_2 A_2)^2. \tag{2.76}$$

The ion signal is modelled as a current source at the input of the pre-amplifier. The ion image current $i_s(t)$ is calculated from the image charges $\mathrm{d}Q_i(t)/\mathrm{d}t$ (see Eq. (2.66)). In the case of single segment detection the image current for a detection at ω_+ is given by

$$i_s(t) = \frac{\mathrm{d}Q_i(t)}{\mathrm{d}t} = -q\frac{R_+}{a_0} c_{i,1} A_{1,0} \omega_+ \sin(\omega_+ t + \chi_{1,0,i}), \tag{2.77}$$

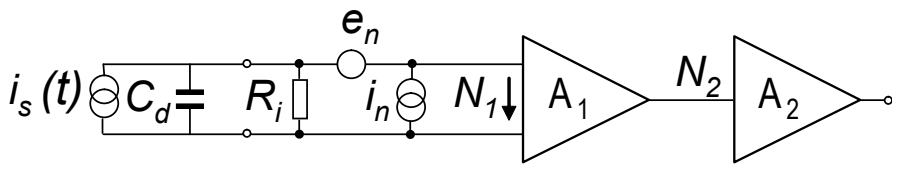

Figure 2.8: The equivalent circuit of the pre- and post-amplifiers used for the broad-band FT-ICR detection. The ion current is described as a current source $i_s(t)$. The detector electrode has a capacitance C_d, which includes the input capacitance of the pre-amplifier. The pre-amplifier is characterized by the gain A_1, the input resistance R_i, the voltage noise e_n and the current source i_n. The post-amplifier has a noise source N_2 and a gain A_2.

which is proportional to the modified cyclotron frequency and is described in M. Comisarow et al. in [49]. The ion image current of an ion moving with only cyclotron motion is a few orders of magnitude higher than for an ion with only magnetron motion. The root mean square value of the ion current $i_s(t)$ for N_ion coherently-moving ions in a Penning trap is given by

$$i_s(\mathrm{rms}) = -N_\mathrm{ion} q \frac{R_+}{a_0\sqrt{2}} c_{i,1} A_{1,0} \omega_+. \tag{2.78}$$

The ion image current is typically in the fA range. It flows through the impedance Z, built by the input resistance of the pre-amplifier in parallel to the detector capacitance. The resulting FT-ICR signal voltage S is amplified by the gain of the two low-noise amplifiers, i.e. $S = i_s(\mathrm{rms})|\mathrm{Z}|\mathrm{A}_1\mathrm{A}_2$. The SNR after the pre- and post-amplifier detection system is calculated using Eq. (2.76).

$$\left(\frac{S}{N}\right)^2 = \frac{(i_s(\mathrm{rms})|Z|A_1A_2)^2}{[e_n^2 + (i_n|Z|)^2 + (4k_\mathrm{B}TR_i|Z|)](A_1A_2)^2 + (N_2A_2)^2}. \tag{2.79}$$

If we assume that the input resistance is large compared to the impedance of the detector capacitance C_d, i.e. $R_\mathrm{i} \gg 1/(\omega C_\mathrm{d})$ then the SNR is simplified to

$$\left(\frac{S}{N}\right)^2 = \frac{(i_s(\mathrm{rms})/(\omega C_\mathrm{d}))^2}{e_n^2 + [i_n^2 + (4kTR_i)^2]/(\omega C_\mathrm{d})^2 + \left(\frac{N_2}{A_1}\right)^2} = \left(\frac{S}{N_1}\right)^2 \cdot \frac{1}{1 + \left(\frac{N_2}{A_1 N_1}\right)^2}. \tag{2.80}$$

The noise sources of the second amplifier can be neglected if the amplified noise of the first amplifier is much larger than the noise of the second amplifier, i.e. $A_1N_1 \gg N_2$. In this case the SNR is independent on the gain A_1 and depends only on the noise of the pre-amplifier.

Chapter 3

A broad-band FT-ICR setup in Heidelberg

A broad-band FT-ICR setup has been built up at the Max Planck Institute for Nuclear Physics (MPIK) in Heidelberg. In this chapter the different components of the setup are discussed. The Penning trap was designed for the KArlsruhe TRItium Neutrino (KATRIN) experiment. Therefore the requirements concerning this project are discussed which includes the characterization of the trapping potential of the Penning trap. Also the stability of the high-voltage source was investigated concerning the fluctuations and temperature drifts. The magnetic field created by the superconducting magnet are analysed in detail. Here the field maps of the homogeneous region are presented.

3.1 Requirements for the KATRIN project

The Penning trap and the detection electronics have been designed the for identification of different ion species in the beam flux coming from the windowless gaseous tritium source (WGTS) of the KATRIN experiment. This project aims to measure the absolute mass of the electron antineutrino with a sensitivity better than 0.2 eV (90% C.L.) by measuring the beta-decay kinematics at the endpoint of the beta-spectrum of tritium [16]. The ion flux from the tritium source towards the detector consists of tritium $^3H^+$, also denoted T^+, tritium clusters $T^+_{3,5}$ as well as low abundant He^+ ions [50, 51]. The aim of the Penning trap in KATRIN is to identify these ion species and to measure their abundance in the ion flux. As seen in Fig. 3.1, the two Penning traps will be installed in the beam tube of the differential pumping section (DPS), one at the entrance and one at the exit of the DPS. The magnetic field is 5.6 T [47]. The DPS is the section behind the tritium source. This way the pumping efficiency of the DPS section can be on-line monitored. It is important

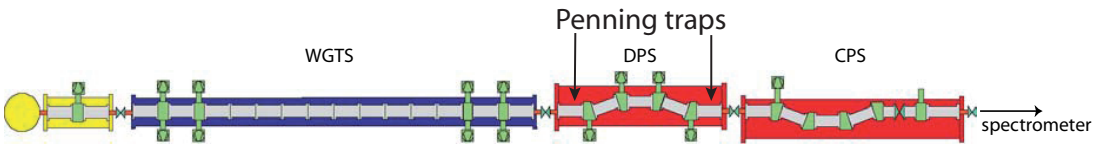

Figure 3.1: The windowless tritium source (WGTS) emits additionally to the β-electrons also molecular tritium. The tritium flow in direction of the spectrometer is reduced by the differential pumping section (DPS) and the cryogenic pumping section (CPS) [51]. The two Penning traps will be located in the DPS section with a magnetic field strength $B_0 = 5.6\,\mathrm{T}$.

to mention that the beam flux, which transports the beta electrons to the detector, should not be reduced and influenced by the Penning traps. The best choice is then to use a cylindrical open-endcap Penning trap which does not strongly restrict the electron flow to the main spectrometer. In this case, the trap radius ρ_0 has to be chosen as close to the beam tube radius as technically possible.

For a simultaneous ion detection in a mass-to-charge m/q range from 3 to 15 u/e, which effectively covers all expected ion species, a broad-band amplifier had been developed by Stahl Electronics[1]. Since the temperature of the beam tube of the DPS was originally planned to be at 70 K the amplifier should work in this environment. For this purpose only GaAs field effect transistors with a low input noise density and a high DC-input resistance are suitable. The cryogenic amplifier should have a low voltage noise density which increases the signal-to-noise ratio and thus low-abundant ion species are detectable.

An important requirement concerns the magnetic field and its inhomogeneity. The mass resolving power $\mathscr{R} = m/\Delta m = \omega_c/\Delta\omega_c$ is directly proportional to the magnetic field B_0 [13]. A minimum mass resolving power $m/\Delta m$ of $2 \cdot 10^5$ is needed to resolve tritium and helium ions. For a magnetic field of 5.6 T the frequency resolution $\Delta\omega_c$ is 130 Hz. Thus, to resolve these two ions a detection time longer than 10 ms is needed.

The magnetic field sets the maximum limit for the density of particles which can be stored in a magnetic field, which is known as the Brillouin limit [52] (see Section 5.3.1). For example, the Brillouin limit for a magnetic field of 5.6 T results in a maximum ion density of 2.8×10^7 ions/mm^3 for tritium ions.

The magnetic bottle term of the magnetic field causes amplitude-dependent frequency shifts, as discussed in Section 2.1.2. This leads to a broadening of the observed FT-ICR signals for the ions in the frequency spectra. In order to resolve the tritium and helium

[1] Stahl-Electronics, Hauptstrasse 15, 67582 Mettenheim, Germany

nuclide the two peaks have to be resolved. For this the magnetic bottle term B_2 should be lower than $0.036\,\mathrm{Tm}^{-2}$.

The materials of the trap have to fulfill two requirements. One is that they need to have a low magnetic susceptibility. This is the case for the copper electrodes, the aluminium support structure and the polyetheretherketon PEEK insulators. Otherwise, the strong magnetic field will magnetize the materials, which therefore leads to an additional magnetic field inhomogeneity at the trap center. The second requirement is that the materials have to fulfill the ultra-high vacuum conditions of the KATRIN experiment. The outgassing rate of the materials for the trap, the amplifier boards and the cables have been tested (see Ref. [47]). The materials fulfill the requirements.

In this thesis the cryogenic broad-band amplifier for the KATRIN project is characterized at 70 K. It should be noted that at the FT-ICR setup in Heidelberg a room temperature broad-band amplifier system is used which has a slightly different design from the KATRIN amplifier. More details and results will be explained in Section 4.4.

3.2 General overview of the FT-ICR experiment

Before describing the specific properties of the electronic devices, an overview is shown in Fig. 3.2 [53]. The setup consists of a vacuum chamber and a superconducting magnet. The cylindrical Penning trap with open-endcap electrodes is placed in the center of the homogeneous region of the superconducting magnet with a magnetic field of 4.7 T. The homogeneous region is roughly 130 mm away from the geometrical center of the magnet, the side further away from the ion source, as seen in Fig. 3.2. The magnet has a horizontal room temperature bore with a diameter of 150 mm. The room where the experiment is setup is not temperature stabilized. This causes for example voltage drifts of the voltage sources or drifts of the magnetic field.
For testing purposes in this thesis, a thermionic ion source[2] emitting $^6Li^+$ and $^7Li^+$ ions is used. Typically the mean kinetic energy of the ions is in the range of 20-40 eV. Behind the ion source a movable Faraday cup is placed to measure the emitted ion current. The ions are focused and guided towards the Penning trap by two electrostatic einzel lenses and the magnetic field. As seen from Fig. 3.2, a Faraday cup or a micro-channel plate (MCP) can be installed behind the Penning trap for detecting the ions. The Faraday cup can be used to measure either the current of the continuous beam or the ion bunches ejected from the trap. The DC current is used to determine the transmission through the magnetic field. The MCP detector can be used to perform time-of-flight measurements of

[2]HeatWave Labs, Inc., 195 Aviation Way, Suite 100, Watsonville, CA 95076-2069

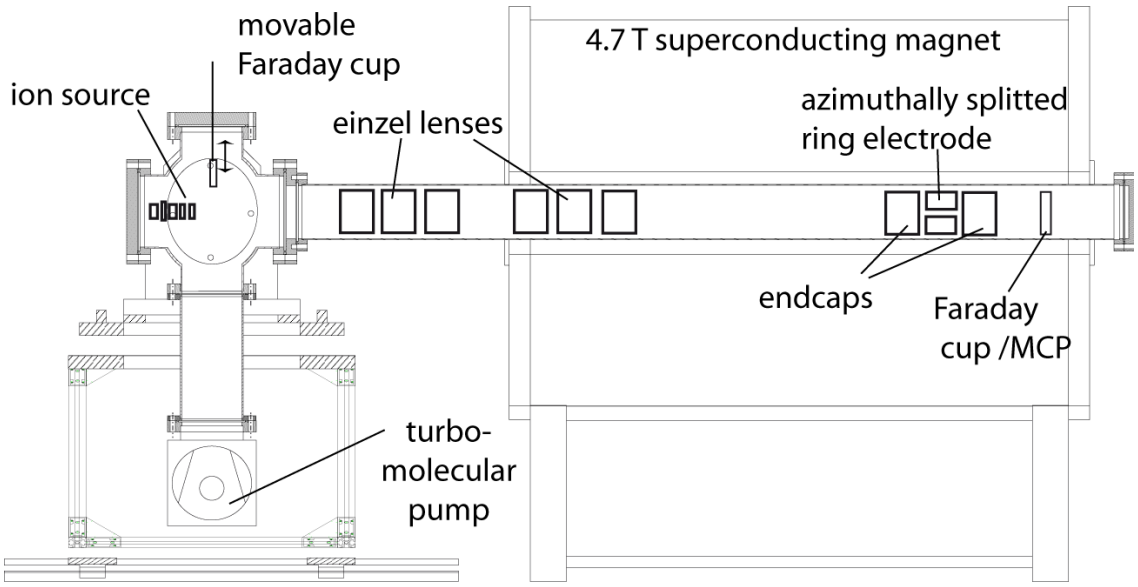

Figure 3.2: Schematic view of the FT-ICR setup located at the MPIK in Heidelberg. The lithium ions are guided from the ion source by an einzel lens system towards the Penning trap which is placed in the homogeneous region of the magnetic field. Notice that the homogeneous region is shifted to the side further away from the ion source. For more details see the text.

the ejected ions. Additionally the number of ejected trapped ions can be determined by using a charge sensitive amplifier which is connected to the Faraday cup detector.

All the components mentioned above are placed in an ultra-high vacuum (UHV) chamber. The UHV is reached by using a turbo-molecular pump (Oerlikon MAG W 600) in combination with a fore-vacuum pump (Edwards XDS 10). A final pressure of $p \approx 5.0 \times 10^{-9}$ mbar can be reached after a bake-out of the setup at 120 °C for three days. All vacuum components, i.e., beam tubes and crosses, are made of non-magnetic 316L stainless steel. The flanges have the CF 100 or CF 160 standard and they are sealed with copper rings. The beam tube inside the magnet bore has an inner diameter of 100 mm while the outside beam tube has a diameter of 160 mm.

To adjust the Penning-trap symmetry axis with respect to the magnetic field axis, the beam tube in the magnet bore can be tilted and shifted in the radial and axial direction, respectively. The fine adjustment is mechanically done by adjusting the screws holding the beam tube on both sides of the magnet. Thus the beam tube can be tilted by maximum angle of 2.7° and shifted along the magnet bore by ± 3 cm and radially by ± 2.2 cm.

3.3 The thermionic ion source

A thermionic ion source is used for the creation of the ions. The source emits positive charged alkali ions through the thermal emission process. For the lithium ion production, a good choice for an emitter material is the β-eucryptite (Li_2O-Al_2O_3-$2SiO_2$) which belongs to the aluminosilicate minerals. This mineral emits lithium ions when it is heated up above 1300 K. The ion emitter material consists naturally of lithium, i.e. the natural abundance of isotopes is ^{6}Li (7%) and ^{7}Li (93%), respectively. The ion source is commercially available from HeatWave Labs Inc.
The lithium emitter is a highly porous tungsten plug which is indirectly heated. The mineral powder is placed on the face of the emitter and melted into the porous tungsten. A bifilar heater coil made of a tungsten and rhenium wire is used to heat a pot of Al_2O_3 mixed with H_2, which finally heats the plug. The thermionic emission process leads to an ion emission from the hot surface when the thermal energy of the ions overcome the work function of the mineral. The emission ion current density J is described by the Richardson law [54]

$$J = AT^2 e^{-W/k_B T}, \tag{3.1}$$

where T is the temperature of the mineral, k_B the Boltzmann constant and $A = 1.2 \times 10^6\,\mathrm{Am^{-2}K^{-2}}$ is the material independent Richardson constant. If an ion has an energy larger than the work function W of the material it escapes from the surface with a probability given by the Boltzmann factor $e^{-W/k_B T}$. The work function for β-eucryptite is about 3 eV [55]. For low energy beams (< 100 eV) the lithium ion emission is space charge limited. Then the ion current follows the Child-Langmuier equation [56], which has a three halves power law of the used accelerating voltage $J \propto V^{3/2}$. It should be noted that a change of the acceleration voltage does not change the work function.
Figure 3.3 (a) shows a technical drawing and (b) shows a photograph of the assembled ion source with the extraction optics. The ion emitter is placed in the accelerator electrode. The created ions are focused and guided by the electrode system, which consists of an accelerator, an extractor, a lens 1 and lens 2, exit lenses and a deflector electrode. The electrodes are isolated by sapphire balls which also fix the distance.

Figure 3.3 (c) shows the electric connections of the heater element. A DC current I_F flows through the filament wire and heats indirectly the tungsten plug. The ion emitter filament is floated by a voltage source which defines the initial potential energy of the ions.
The ion current is detected with a movable Faraday cup which is placed right after the ion source (see Fig. 3.2) and read out with a pico-ampere meter. Typically the extracted

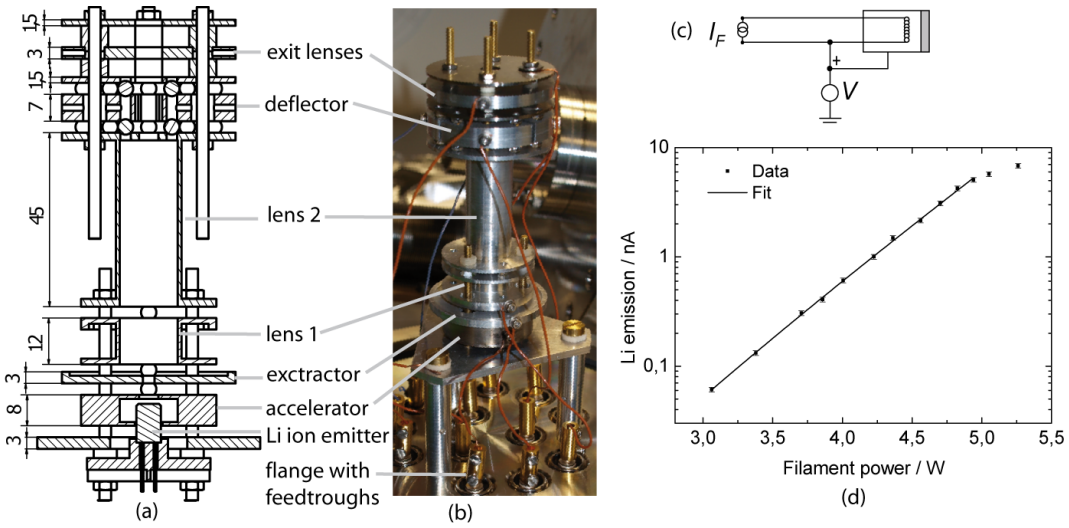

Figure 3.3: A detailed technical drawing (a) and a photograph (b) of the alkali ion source. The scale is in mm. The gray dashed parts of (a) are the electrodes. (c) The current source delivers the filament current I_F which is floated by a positive voltage V. (d) The measured lithium emission current behind the ion source is shown as a function of the filament power. The black line is a fit of the Richardson law (see Eq. (3.1)) to the data up to a current of 4.9 A, before the current saturates.

ion current is in the nA-range. Figure 3.3 (d) shows the extracted DC lithium ion current as a function of the filament heating power which is proportional to the emitter surface temperature. The ion current increases exponentially with the heater power. Fitting the data with the Richardson law yields good agreement. A saturation of the ion current density on the surface of the ion emitter for high filament powers leads to a deviation of the measured current from the Richardson law for filament powers higher than 5 W.

3.4 Ion transport

The ion transport from the ion source towards the Penning trap is achieved with electrostatic lenses and the magnetic field. Typically, the ions are transported with a kinetic energy of 20-40 eV. First, the ion beam is focused and deflected by the optics mounted on the ion source, as seen in Fig. 3.3 (a). For focusing and deflecting the ion beam towards the superconducting magnet, two electrostatic einzel lenses are used, as seen in Fig. 3.2. Each einzel lens consists of three hyperbolical electrodes which are azimuthally four-fold segmented, so that the lenses can be used for both, focusing and deflecting the ion beam. A focus is created if all four segments are biased with the same potential. In the deflecting operation two neighbouring segments of one electrode are connected to ground and the

two opposing segments are connected to the voltage supply.
When the ions are injected in the magnetic field the Lorentz force compresses the ion beam radially. The ions can also be reflected due to the magnetic mirror effect. When the ions pass the magnet, they can be detected with a Faraday cup placed behind the Penning trap. This way the transmission of the ions through the magnetic field is measured and optimized by varying the potentials applied to the electrodes of the optic elements.

The materials of the einzel lenses (copper electrodes, stainless steel holders and ceramic insulators) have a negligible magnetic susceptibility. Otherwise the materials will be, as mentioned before, magnetized by the magnetic field and this leads to additional inhomogeneities. The electric connections of the electrodes to the voltage supply are done with Teflon insulated copper wires. A bipolar voltage source with a range of $\pm 500\,\mathrm{V}$ is used for biasing the electrodes. The HV supply will be characterized in Section 3.6.

3.5 The cylindrical Penning trap

An open trap geometry is required for the KATRIN experiment as explained in Section 3.1. Thus, the only feasible way to fulfill these requirmenets was to construct a cylindrical Penning trap with open endcap electrodes. With two cylindrical correction electrodes, placed between the ring and endcap electrodes, the anharmonicities of the trapping potential can effectively be tuned out. Since a mass resolving power of maximum 10^6 is sufficient for the use in the KATRIN experiment, the trap geometry can be further simplified by not using correction electrodes at all. Figure 3.4 shows a technical drawing and a photograph of the designed Penning trap. Within this thesis results from measurements with two different cylindrical Penning traps will be presented. Both traps have the same dimension and both have two two-fold segmented endcap electrodes (see Fig. 3.4) but one trap has a four-fold segmented ring electrode while the other trap has an eight-fold segmented one.
The trap designed for the KATRIN experiment has a four-fold segmented ring electrode, each segment has an opening angle of 87° and the gap between the electrodes is 3°. The trap used at the setup in Heidelberg has an eight-fold segmented ring electrode, each segment has an opening angle of 42°.

The trap support structure is made of the aluminium alloy $\mathrm{AlMg_3}$ and the electrodes are machined out of oxygen-free high purity copper (99.99 %). Copper is well suited for a trap construction due to its high electric conductivity as well as its low magnetic susceptibility (-8×10^{-7} at $T = 293\,\mathrm{K}$) [57]. Magnetization of the material due to the external magnetic field changes the homogeneity of the magnetic field. This is negligible for copper. In order to avoid oxidation of the surface, the copper electrodes are first plated with

a 50 µm thick silver layer and then with a 1 µm thick gold layer. The silver layer prevents that gold diffuses into copper. Before plating the copper electrodes they are polished in order to have sufficiently smooth surfaces.
The insulation pieces are made of PEEK, which has a low outgassing rate and a high heat resistivity. The PEEK spacers are used for insulating the electrodes from the outer structure as well as holding the electrodes. The pre-amplifier used for the image charge detection and the filter board used for filtering the excitation and DC signals are mounted on top of the aluminium support structure as seen in Fig. 3.4 (b).

3.5.1 Calculation and simulation of the trapping potential

The electrostatic trapping potential or any potential field in a charge free environment fulfills the Laplace equation ($\Delta\Phi(x,y,z) = 0$). When applying a voltage V_0 between the endcaps and the ring electrode, the potential near the trap center is given by $V = V_0\Phi_0$, where Φ_0 is a solution of the Laplace equation with Dirichlet boundary value. An analytical expression for the trapping potential for the cylindrical Penning trap can be calculated which fulfills the Laplace equation. The potential near the trap center is expanded with the Legendre polynomials $P_k(\cos\theta)$ [58]:

$$V = V_0 \frac{1}{2} \sum_{k=0,\text{even}}^{\infty} C_k \left(\frac{r}{d}\right)^k P_k(\cos\theta), \tag{3.2}$$

where the coefficients C_k depend on the trap geometry and are expressed in terms of the Bessel functions of order zero J_0:

$$C_k = \frac{(-1)^{k/2}}{k!} \frac{\pi^{k-1}}{2^{k-3}} \left(\frac{d}{z_0 + z_e}\right)^k \sum_{n=0}^{\infty} (2n+1)^{k-1} \frac{A_n}{J_0(ik_n\rho_0)}. \tag{3.3}$$

The parameters k_n and A_n are given by

$$k_n = \frac{(n+1)\pi}{z_0 + z_e} \tag{3.4}$$

$$A_n = \frac{1}{2}\left[(-1)^n - 2\sin(k_n z_0)\right]. \tag{3.5}$$

One can see that the potential in Eq. (3.2) scales with $(r/d)^k$ where d is the characteristic trap dimension defined in Eq. (2.3). Due to the axial symmetry only even coefficients C_k appear in the sum.
For a cylindrical trap the length z_0 is geometrically defined as the distance between the trap center and the endcap electrode. Note that the trap dimension d is defined for hyperbolic traps. As explained in [8] the parameter d for cylindrical traps is used for the comparison

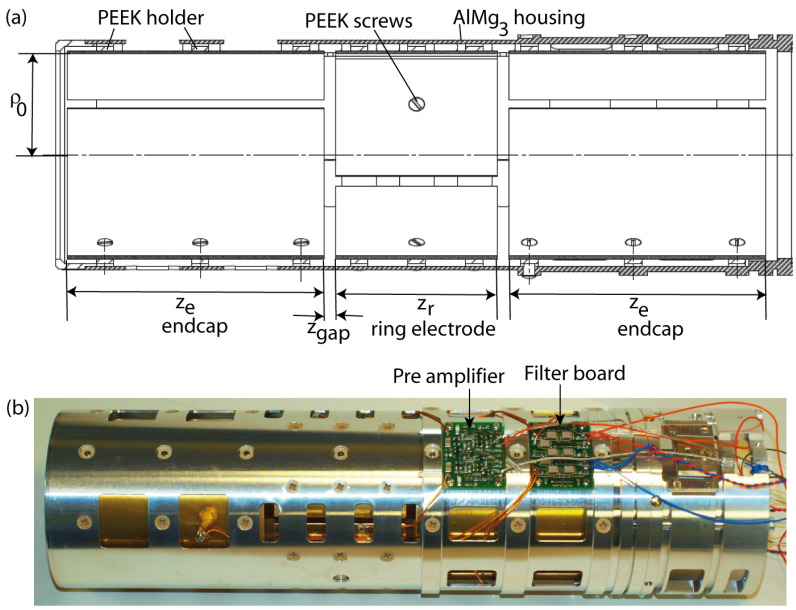

Figure 3.4: Technical drawing (a) and photograph (b) of the open cylindrical Penning trap with two two-fold segmented endcap electrodes on the left and the right side, and a four-fold segmented ring electrode at the center. The length are $z_e = 89\,\text{mm}$, $z_r = 56\,\text{mm}$, $z_{gap} = 4\,\text{mm}$ and the radius is $\rho_0 = 35.5\,\text{mm}$. The pre-amplifier and the filter board are attached to the trap support structure.

of the coefficients with the hyperbolic traps. The potential in Eq. (3.2) is expanded into $(r/d)^k$, which is exactly the same as for the hyperbolic trap.

The coefficients C_2, C_4 and C_6 are calculated for the uncompensated cylindrical Penning trap by using the dimensions defined in Fig. 3.4 (a). The gap z_{gap} between the ring and each endcap electrode of 4 mm is not considered for the calculation of the coefficients. The sum of the gap width and the ring electrode length $z_r/2$ results in a length of 32 mm. Figure 3.5 shows the coefficients C_k as a function of the characteristic length z_0. As seen, C_2 and C_6 do not strongly depend on z_0. The coefficient C_2 determines the axial frequency (see Eq. (2.8)). The higher order coefficients C_4 and C_6 terms lead to an amplitude-dependent frequency shift (see Section 2.1.2 for C_4). The coefficient C_4 change its sign at $z_0 = 29\,\text{mm}$, which cause a change of the sign of the frequency shift from the electrostatic contribution. The coefficient C_0 describes the offset potential in the trap center with respect to the chosen ground potential. This potential gives additional potential energy when ejecting the stored ions from the trap.

In order to quantify deviations from the quadrupolar potential further away from the trap center, simulations of the electrostatic potential has been done with the program

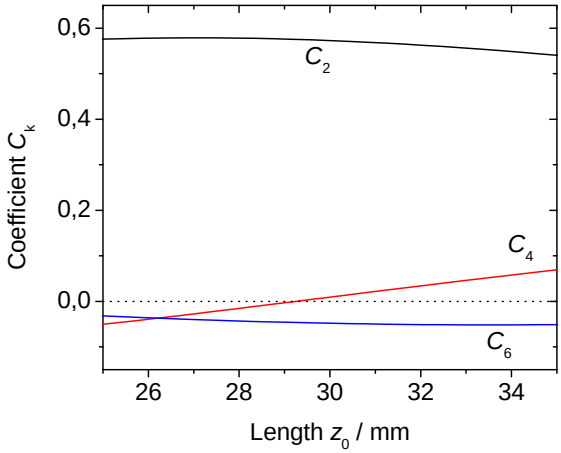

Figure 3.5: The polynomial coefficient C_k as a function of the length z_0. The parameters for the calculation of C_k are $\rho_0 = 35.5\,\text{mm}$ and $z_e = 89\,\text{mm}$.

COMSOL[3]. This program solves numerically the Laplace equation with given boundary conditions by using the Finite-Elemente-Method (FEM). The simulation makes use of the axial symmetry. The electrodes are assumed to be made of highly conducting copper. For simplicity, the potentials on the ring electrode and the endcap electrodes are set to 0 V and 1 V, respectively. Figure 3.6 (a) shows the electric potential for a plane extending from the trap axis at $\rho = 0$ to 35 mm and from $z = 0$ to $\pm 121\,\text{mm}$. As expected, the equipotential lines form a saddle point potential at the trap center. The potential near the surface of the ring electrodes is strongly anharmonic and the potential is close to 0 V. Thus an ion injected off-center would see a smaller potential barrier than an ion on the trap axis.
Figure 3.6 (b) shows the electric potential $V(z, \rho = 0)$ along the trap axis and the radial potential $V(z = 0, r)$ along the radial plane. The simulated axial potential near the trap center is fit with a function $V(z,0) = V_0/2(C_0 + C_2/d^2\, z^2 + C_4/d^4\, z^4)$ given in Eq. (3.2) with $P_k(\cos\theta) = P_k(1) = 1$. The coefficients are found to be $C_0 = 0.399\,591(3)$, $C_2/d^2 = 7.714(1) \cdot 10^{-4}\,\text{mm}^{-2}$ and $C_4/d^4 = -7.4(7) \cdot 10^{-9}\,\text{mm}^{-4}$. The simulation data are nicely described by the theoretical function, since residuals of the fit values are in the range of 10^{-6}.

3.5.2 Rf fields for ion motion excitations

The excitation of the ion motion can be done with dipolar and quadrupolar rf fields, as described in Sections 2.2.1 and 2.2.2. The excitation fields are created using the four

[3]Comsol Multiphysics GmbH, Berliner Str. 4, 37073 Göttingen

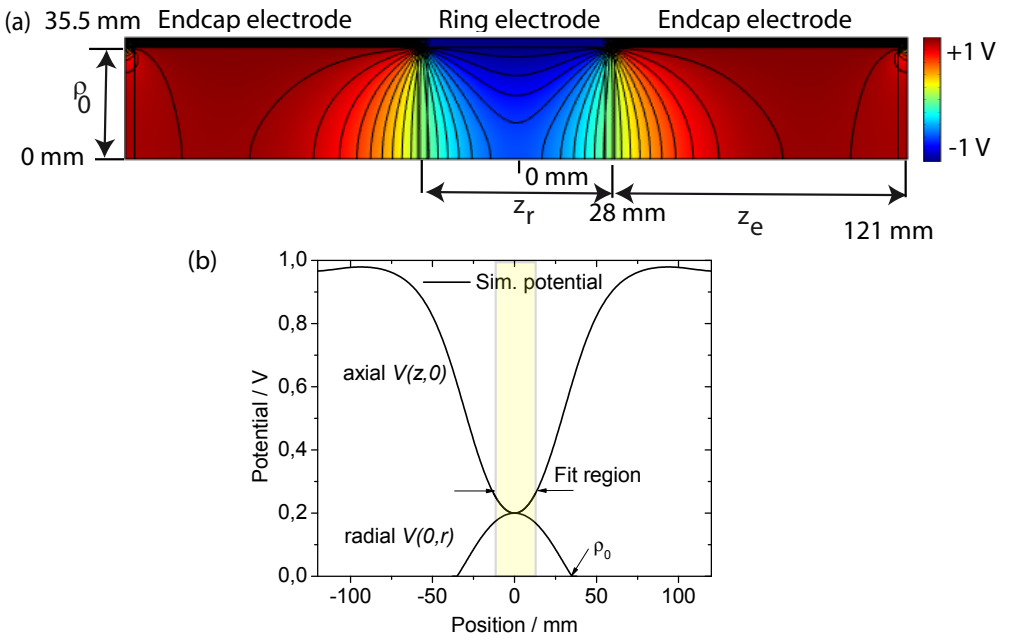

Figure 3.6: (a) Contour plot of the electrostatic potential with a FEM simulation shown for a half of the trap from $z = 0$ to $\pm 121\,\text{mm}$ and $\rho = 0$ to $35.5\,\text{mm}$. (b) The axial potential $V(z, \rho = 0)$ on the trap axis and the radial potential $V(z = 0, r)$ for $z = 0$ along the radial plane. The yellow band is the region used to fit the projection $V(z, \rho = 0)$ of the simulated potential.

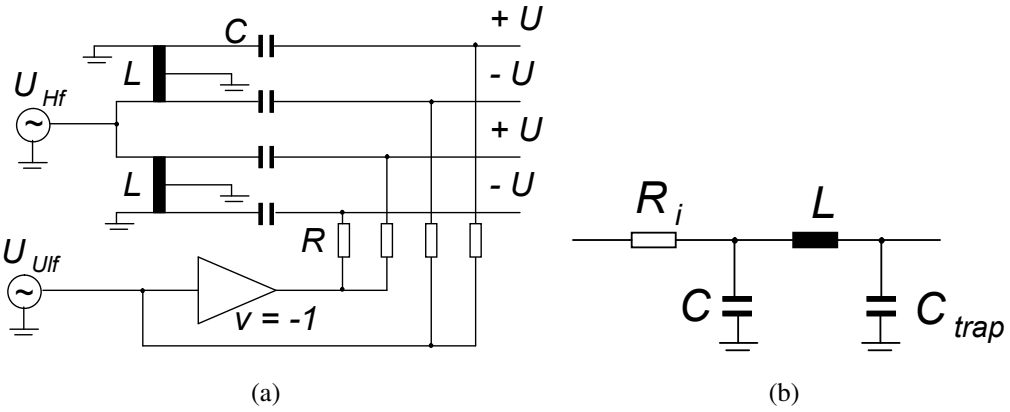

Figure 3.7: (a) Scheme of the electrical circuit used for creating rf signals with an amplitude $\pm U$. A passive circuit is used for the high frequency range (1 to 12 MHz) while an active circuit is used for the ultra-low frequency range (0.1 to 2 kHz). The amplifier has a gain of -1. (b) Π-circuit as an impedance matching circuit at 20 MHz with an inductance $L = 4\mu\text{H}$, $C = 100\,\text{pF}$ and the parasitic trap capacitance C_{trap} of 63 pF. The waveform function generator has an output impedance of $R_i = 50\,\Omega$.

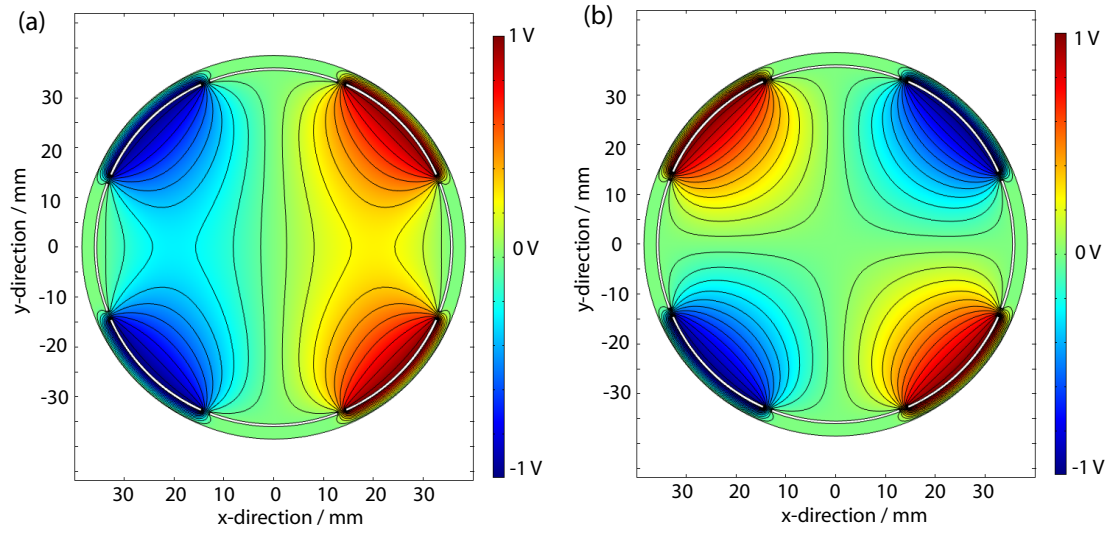

Figure 3.8: Electrostatic FEM simulation of a dipolar (a) and a quadrupolar (b) rf field with zero phase shown in the azimuthal plane at $z = 0\,\text{mm}$. The fields are created by applying either $1\,\text{V}$ or $-1\,\text{V}$ to the excitation segments of the ring electrode.

segments of the eight-fold segmented ring electrode. The rf excitation fields need signals with amplitudes of $\pm U$. Therefore an electrical circuit is needed to create signals with opposite phase. A phase shifter has been built as shown in Fig. 3.7 (a), one for the low frequency range and a second one for the high frequency range. This circuit has two inputs for connecting the rf signals delivered by the function generators and four output signals which are connected to the four excitation segments of the ring electrode as shown in Fig. 2.3.

In the setup presented here, the cyclotron frequency ν_c is in a high frequency range from 1 to 12 MHz. Two transformers have been built with a passive circuit using an iron powder toroidal core. The primary and the secondary side are wound with a copper wire. Due to Faraday's induction law, the induced voltage on the secondary side has a phase shift of π. The phase shift and the response curve of the coil have been measured with an oscilloscope. The band pass filter has a maximum transmission at 2 MHz and an attenuation of 3 dB at 0.3 and 12 MHz. This is sufficient for the excitation of particles with an m/q-ratio from 6 to roughly 230.

The magnetron frequency is in the frequency range from 0.1 to 2 kHz. An active inverting amplifier having an amplification factor of -1 has been built to create a phase shift of π. By connecting the output rf signals to the ring electrode segments in the correct order, dipolar or quadrupolar excitation geometries can be created, as already mentioned in Fig. 2.3.

For an excitation at the modified cyclotron frequency ν_+ and the higher harmonic frequency $2\nu_+$, in some cases larger excitation amplitudes are needed. Since the maximum output amplitude of the waveform function generators of $10\,V_{PP}$ is not high enough, an impedance matching network has been built using a capacitor and an air coil, as shown in Fig. 3.7 (b). Such a network is known as a Π-circuit and acts as an amplifier. In this case, the circuit reaches an amplification factor of roughly 6 at a resonance frequency of 10 MHz and 20 MHz. The circuit transfers the maximum power from the output impedance of the function generator to the capacitive load due to the *LC*-resonance circuit. The parasitic trap capacitance C_{trap} has been determined with an *LC*-circuit which was connected to one segment of the ring electrode.

The azimuthal dipolar and quadrupolar excitation field potentials were simulated with the program COMSOL. Figure 3.8 shows color coded field maps for the trap with the eight-fold segmented ring electrode. The color scale shows the potential which increases from negative (blue) to positive (red) values. For a dipolar excitation, the potentials on the electrodes $S_{exc,1}$ and $S_{exc,2}$ are set to $-1\,V$ and on the opposite electrodes $S_{exc,3}$ and $S_{exc,4}$ to $+1\,V$ (see also in Fig. 2.3). The detection electrodes are set to 0 V. The created dipolar potential is shown in Fig. 3.8 (a). Near the trap center the equipotential lines are parallel to the *y*-direction. Along the *x*-axis, a linear increase of the potential is observed and thus ions at this excitation phase feel a force in *x*-direction.
Figure 3.8 (b) shows the created quadrupolar potential, where the potential on the electrodes $S_{exc,1}$ and $S_{exc,3}$ is set to $+1\,V$ and on the electrodes $S_{exc,2}$ and $S_{exc,4}$ to $-1\,V$. A quadrupolar potential is formed near the trap center while a strong deformation close to the electrodes is observed. The quality can be improved by using all eight segments for excitation. It should be noticed that the 0excitation field inhomogeneities along the axial direction can be neglected since the ring electrodes have a length of 56 mm.

3.6 Stability of the high-voltage source

The voltage source used in the setup delivers the trapping potential and bias the electrostatic einzel lenses. A voltage drift of the trapping potential causes an axial frequency shift, which leads to shift of the ion's eigenfrequencies ν_+ and ν_-. The stability of the voltage source has been investigated for a typical measurement time of a few minutes as well as for a long term measurement to study the voltage drifts due to temperature dependencies. A high-voltage source HV 500-16 from Stahl Electronics is used. It is a 16 channel bipolar DC-voltage source with up to $\pm 500\,V$ output voltage per channel. The device is connected to the laboratory PC running with a LabView based control software. The voltage source has a low voltage noise level of 1.06 mV in the frequency range from

0 to 10 MHz [59].

For the characterization of the voltage source, one channel was set to 10 V and its output was recorded every second for a duration of 40 h. The temperature of the device was simultaneously recorded. Both, temperature and voltage, were measured with the pico-ampere meter (Keithley, 6514 Electrometer). Figure 3.9 (a) shows an Allan deviation plot. It shows the relative voltage drift for different time intervals. First a decrease of the relative voltage drift is observed. The voltage source has the highest relative stability of 18 ppm for a time interval of 0.018 h, i.e. 64 s. For longer time intervals the relative voltage drift increases slowly. The fluctuations from the measurement device could be excluded since the Allan deviation is determined to be two orders of magnitude below the fluctuations of the voltage source.
The voltage data which have been recorded every second are statistically distributed. Figure 3.9 (b) shows the voltage distribution in 500µV steps around the center voltage 9.9809 V. The offset voltage of 19 mV does not result from the measurement but from intrinsic properties of the HV supply. The voltage fluctuations are Gaussian distributed with a standard deviation of $\sigma = 0.55$ mV which gives a relative stability of 55 ppm in the second time-scale range.

During the long-term measurement a maximum temperature difference of 1.5 K was observed which is due to the temperature change between day and night. The environment of the setup is not temperature stabilized. By correlating temperature data to voltage data the temperature coefficient has been determined to be 50 µV/K. This value is below the measured standard deviation of 550 µV at 10 V. No broadening of the Gaussian distribution was observed. It should be noted that the cross talk between two neighbouring channels is in the range of 1.2 ppm, which is well below other fluctuations at 10 V [59].

The voltage source is good enough for biasing the HV-switch which is used for switching the trapping potential. For example, the magnetron frequency is proportional to the trapping potential. The voltage fluctuation for a typical trapping voltage of 60 V results in a magnetron frequency fluctuation of roughly 42 mHz which is well below the detection resolution of the current FT-ICR setup.

3.7 The superconducting magnet

The magnetic field is created by a superconducting magnet which was assembled by Oxford Instruments[4] in 1985. It is a horizontal magnet with an inner bore diameter of 120 mm. The main coil is charged up with a current of 46 A. As already noted in Fig. 3.2,

[4] Oxford Instruments, Abingdon, UK

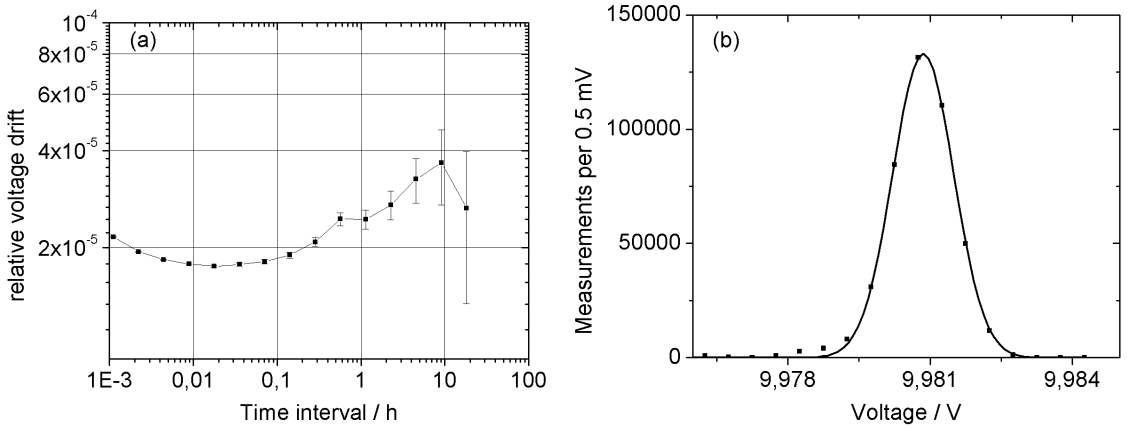

Figure 3.9: (a) The relative voltage drift of the voltage source as a function of the time interval in an Allan deviation plot. The output voltage of 10 V was recorded every second for a duration of 40 h. (b) Distribution of one-second long voltage measurements. The output voltage has a Gaussian distribution. The fit is shown with a black line. The short term stability of the source in one-second time-scale is described by the standard deviation $\sigma = 0.55\,\mathrm{mV}$.

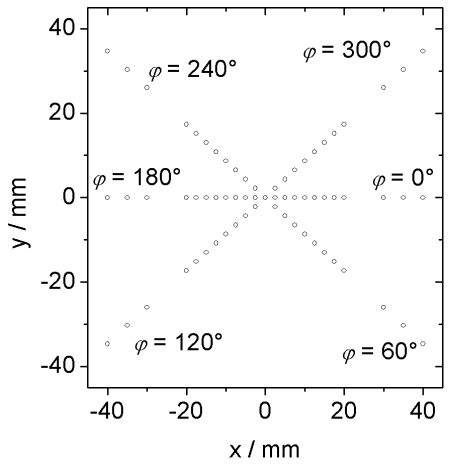

Figure 3.10: Each open circle defines the position in the (x,y)-plane of the measurement probe for the magnetic field measurement. The z-axis points into the paper. The angel φ rotates clockwise.

the position of the main coil is not at the center of the 1 m long magnet but axially off by 130 mm. The magnet has one shim coil for each direction, i.e. a x-, y- and z-shim coil. Each of them can be independently used to improve the homogeneity of the magnetic field. The magnet was setup and shimmed in the FT-ICR laboratory in Heidelberg in March 2008. At that time the shim coils have been loaded with the currents provided by the previous user in the laboratory notebook, which were slightly different from the currents given in the manual.
In order to minimize the initial magnetron radius of the captured ions two apertures were inserted close to the homogeneous region. Shooting the ions through these apertures was unsuccessful probably due to a tilted magnetic field. Therefore, magnetic field measurements have been performed and showed that the field was shifted and tilted. To correct these magnetic field shifts we decided to set different shim currents to the superconducting magnet. Unfortunately, the x- and y-shim coils appeared to be broken while the z-shim coil still worked. Application of any current to the x- and y-shim coils resulted in no change of the magnetic field. Most probably the superconducting switch heater units are broken. The switch is used to break the superconducting coil loop so that the current can be directed to flow through the current source. Thus the magnetic field in x- and y-directions haven't been improved.

The magnetic field was measured in the radial plane for different z-positions as shown in Fig. 3.10. The radial plane is described by the radius and the angle φ which was varied clockwise in 60° steps. Figure 3.11 shows results of various measurements of the magnetic field as a function of the z-direction (a) and (b), of the angle (c) and of the radius (d) in four different panels. While the magnetic field in (a) is measured with a Hall probe (Sypris, 7010 Gauss/Teslameter), the measurements in the panels (b)-(d) have been performed with a Nuclear Magnetic Resonance (NMR) probe (Metrolab, TP2025 NMR Teslameter). The Hall probe measures the projection of the magnetic field on the axial direction, while the NMR probe measures the absolute value of the magnetic field. The latter one drives the nuclear spin state of deuterium atoms in the probe head which depends on the magnetic field [60].
Figure 3.11 (a) shows the axial component of the magnetic field along the bore axis. The measurement was done in about ± 1 m around the homogeneous region of the magnet. The magnetic field in the homogeneous region is roughly 4.699 T. This region is shifted by 120 mm away from the geometrical center of the magnet to $z = 0$ mm in the plot. The magnetic field is mainly created by the main coil and decreases symmetrically around the center. The data points are fitted with a model using a current loop which is the black line in the plot. It turned out that a description of the axial magnetic field with five current loops is very good [61].

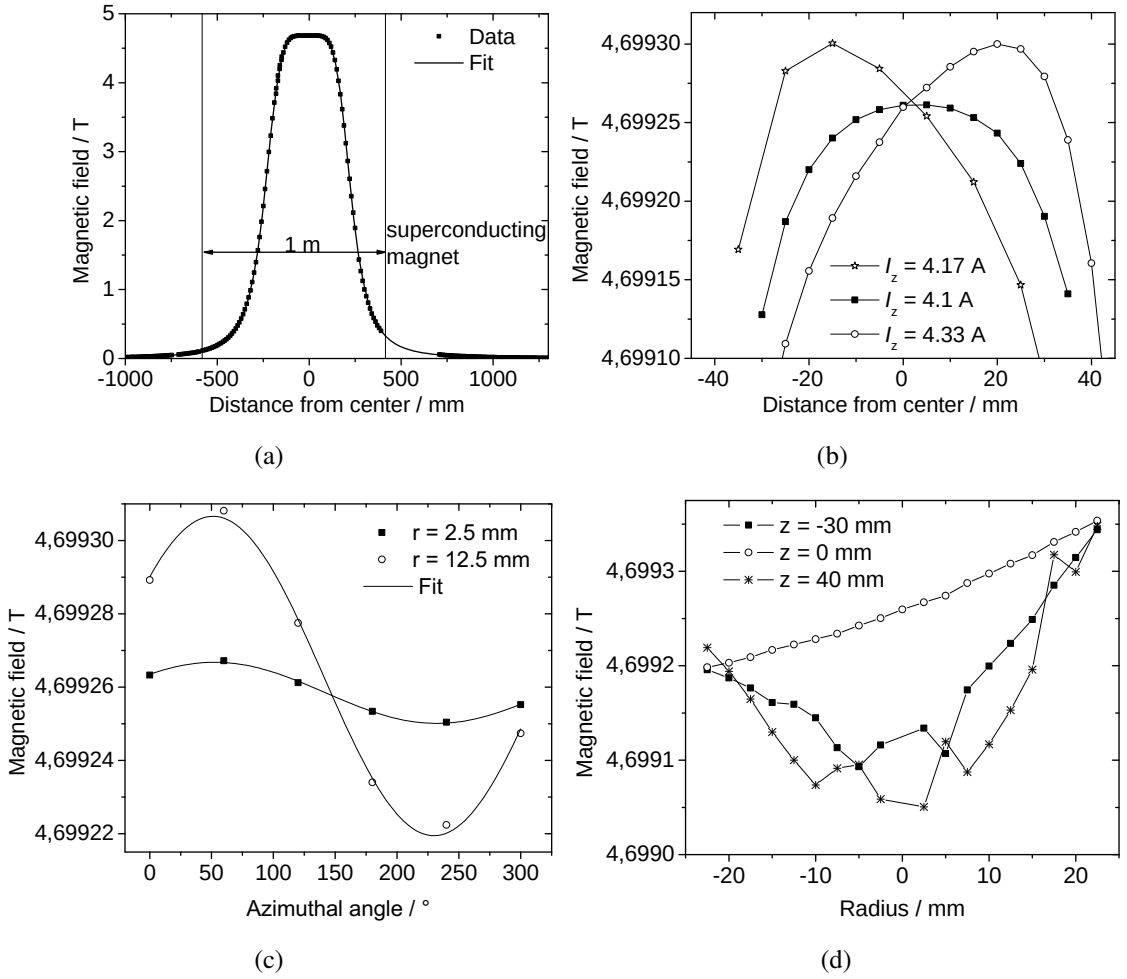

Figure 3.11: (a) Magnetic field along the magnet axis measured with a Hall probe. The homogeneous region is shifted to zero so that a symmetric decrease of the field is seen. Thus, zero on the z-axis in panels (a) and (b) refers to the maximum magnetic field along the z-direction. The black line is a fit of a model with five current loops to the data. The measurements in the (b-d) panels were taken with an NMR probe. (b) Magnetic field along the axial direction for three different shim currents in the z-shim coil of the superconducting magnet. (c) Magnetic field as a function of the azimuthal angle φ for two different radii at an axial position of $z = 0\,\text{mm}$. The maximum magnetic field is at 60°. The black solid lines are sinusoidal fits to the data. (d) Radial dependence of the magnetic field at different axial positions measured at an angle of $\varphi = 60°$. See text for further details.

A detailed look into the homogeneous magnetic field region is shown in Fig. 3.11 (b)-(d), where the magnetic field is plotted as a function of the axial direction (b), the azimuthal angle (c) and the radius (d). Figure 3.11 (b) shows the magnetic field along the z-direction for three different shim currents in the z-shim coil. A shim current of $I_z = 4.33\,\mathrm{A}$ (open circles) was the original value before the shimming of the magnet. As seen, the magnetic field was not symmetric around the maximum value and decreased more steeply further away from the center. However, a symmetric behaviour along the z-axis is expected due to the magnetic bottle term (see Section 2.1.2). Figure 3.11 (b) indicates that the position of the maximum depends on the current loaded in the z-shim coil. For the lowest and highest shim currents an asymmetric form of the magnetic field was observed. For $I_z = 4.17\,\mathrm{A}$ the magnetic field has a quadratic form, which is well described by $B(z) = B_0 + B_1 z + B_2 z^2$. A region of $\pm 15\,\mathrm{mm}$ around the center is used for the fit not shown in Fig. 3.11 (b). This yields the coefficients $B_0 = 4.699\,267\,8(3)\,\mathrm{T}$, $B_1 = 10.6(4) \times 10^{-6}\,\mathrm{T/mm}$ and $B_2 = -6.52(20) \times 10^{-8}\,\mathrm{T/mm^2}$. The maximum magnetic field is located 370 mm away from the right side of the magnet housing (see Fig. 3.2).
Figure 3.11 (c) shows the absolute value of the axial magnetic field at $z = 0\,\mathrm{mm}$ as a function of the angle for two different radii. The data points show an oscillating behaviour which can be explained by the magnetic field created by the x- and y-shim coils. These fields are superimposed to the field created by the main coil which leads to a shift the magnetic field in the radial direction. The data are fitted with a sinusoidal function. Both curves have the same baseline B_0. For a radius $r = 2.5\,\mathrm{mm}$ the fit yields an amplitude of $8\,\mu\mathrm{T}$ with respect to B_0 and for $r = 12.5\,\mathrm{mm}$ the amplitude is $43\,\mu\mathrm{T}$, which are 2 and 12 ppm, respectively. This amplitude increases due to the quadrupolar nature of the magnetic field. The tilt and the shift of the magnetic field in the x- and y-directions could not be corrected due to the broken x- and y-shim coils.
Figure 3.11 (d) shows the magnetic field as a function of the radius for a shim current of $I_z = 4.17\,\mathrm{A}$, at different positions: $z = 0\,\mathrm{mm}$, $z = 40\,\mathrm{mm}$ and $z = -40\,\mathrm{mm}$. As one can see, the magnetic field increases for $z = 0\,\mathrm{mm}$ while for off-center the field shows a minimum at the center of the bore. This is unexpected since the magnetic field has the highest value at $z = 0\,\mathrm{mm}$ and is hence an indication of wrong shim currents in the x- and y-shim coils.

After shimming the z-shim coil the magnetic field has been mapped by using the NMR probe. Figure 3.12 shows color-coded plots of the magnetic field relative to 4.699 T in a plane perpendicular to the trap axis for different axial positions from -30 to 40 mm around the maximum magnetic field at $z = 0\,\mathrm{mm}$. The lines indicate equal absolute values of the magnetic field and have a distance of $10\,\mu\mathrm{T}$. The scale of the magnetic field changes from blue (low field) to red (high field).
As seen from Fig. 3.12 (a) and (h) a minimum magnetic field is observed at the center

of the bore as well as a strong increase from the center towards the point $(20,-30)$ mm, given in Cartesian coordinates (x,y). The panels (b) to (g) show no clear minimum, but a uniform decrease of the magnetic field from the point at $(20,-30)$ mm to the point at $(-20,30)$ mm, which corresponds to the angles 60° and 240°, respectively. The shifted maximum leads to the oscillatory behaviour as described for Fig. 3.11 (c). Notice that the gradient in the panel from (b)-(g) is lower than in the panels (a) and (h). This is already discussed in Fig. 3.11 (d).
The x- and y-shim coils appear to have significant currents running through them. Unfortunately, these currents cannot be quenched due to the broken superconducting heater units. One should notice that when moving magnetic materials inside the magnet bore a current in the shim coils is induced due to Ampere's Law. More details of simulations with COMSOL can be found in the diploma thesis of H. Golzke [61]. Within the model, the geometry of one shim coil was taken into account and the magnetic field near the trap center was simulated. These simulations reproduce well the observed shifts of the magnetic field.

The Penning trap will be placed in the most homogeneous part of the newly-shimmed magnet at $z = 0$ mm, which is 370 mm away from the averted side of the magnet support structure when looking from the ion source. The spatial homogeneity is defined as the maximum magnetic field deviation inside a volume of a hexagon. The volume is given by the flat-to-flat distance of 5 mm and the height of ± 6 mm around $z = 0$ mm on the field axis. A spatial homogeneity of $\Delta B/V = 5.84 \times 10^{-5}$ T/cm^3 is determined. The homogeneity $\Delta B/B_0$ is thus 10 ppm.

The magnetic field is not stable over time and fluctuations occur due to environmental influences. The magnetic field also decays over time due to the flux creep effect in a superconducting magnet [62]. For the magnet used in this thesis the decay rate was measured with an NMR probe placed for 96 hours at the center of the magnet to be $\Delta B/(B\Delta t) = 2.5 \times 10^{-11}\,\mathrm{min}^{-1}$ [53] . In addition to the constant decay, a room temperature dependent variation of the magnetic field was measured, yielding a temperature dependency of roughly 1.2 μT/K. This is sufficient for reaching a mass resolving power of 10^6 like in the FT-ICR experiment presented here.

It should be mentioned that compared to a high-precision mass spectrometry setup the liquid helium level in the superconducting magnet is not pressure-stabilized. Therefore the temperature of the liquid helium fluctuates over time. Thus, the magnetization of the surrounding materials changes due to their susceptibility. This causes finally some fluctuations of the magnetic field. These fluctuations can be minimized by stabilizing the bore temperature and the liquid helium pressure.

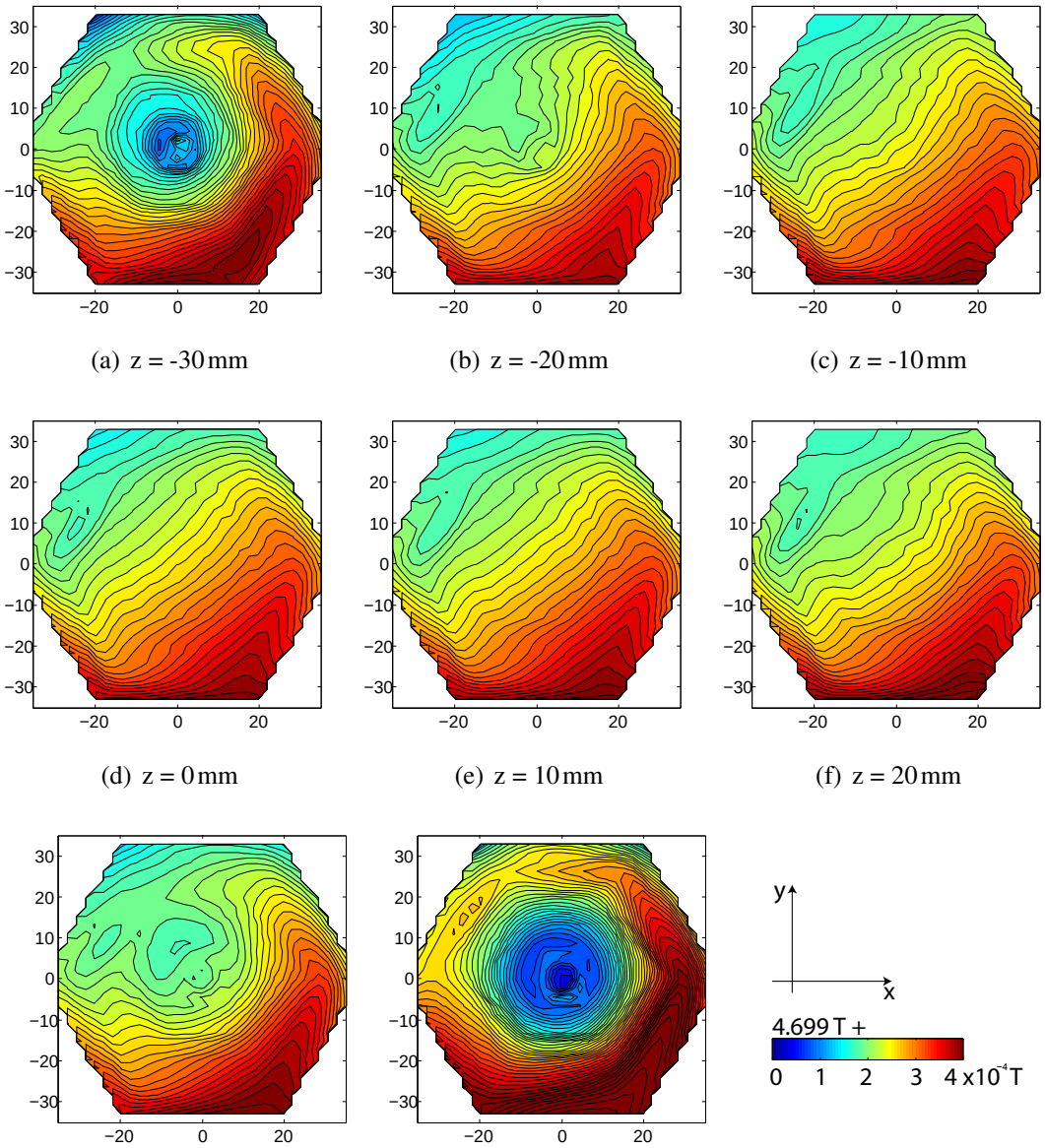

(a) z = -30 mm (b) z = -20 mm (c) z = -10 mm

(d) z = 0 mm (e) z = 10 mm (f) z = 20 mm

(g) z = 30 mm (h) z = 40 mm (i) Scale

Figure 3.12: The magnetic field relative to a constant value of B =4.699 T. The field is measured for eight different axial positions in a plane perpendicular to the magnet axis. The colour code goes from low (blue) to high (red) magnetic field values and the contour lines are separated by 10 µT. In panel (a) and (h) a minimum magnetic field is observed at the center of the magnet. The maximum magnetic field in the axial direction occurs at $z = 370$ mm. The tilt and the shift of the magnetic field is due to the broken x, y-shim coils.

Chapter 4

FT-ICR detection system

For the ion image charge detection a new broad-band FT-ICR detection system was installed at setup at the MPIK. For the determination of the ion's eigenfrequency a timing scheme has to be applied which defines each step of a measurement cycle. The FT-ICR control system was developed to have a flexible control of the excitation parameters and it provides various detection schemes. In this section the working principle of the control system is presented. Also the basics of the Fourier transformation, which is used for transforming the ion signals into a frequency spectrum, are described.

In order to ensure that the observation of an ion signal with a proper signal-to-noise ratio is possible, the amplifiers have to be characterized. The amplifier is used to amplify the tiny ion currents induced on the detection electrodes. Results of the noise behaviour and the voltage amplification are presented for the KATRIN pre-amplifiers as well as for the pre-amplifier used at the setup at MPIK.

4.1 Timing scheme of the measurement cycle

For the manipulation of the ion motion and the frequency determination a timing scheme has to be applied. For a measurement cycle the trigger system has to be started as is described in Section 4.2. A timing scheme for a typical measurement cycle is shown in Fig. 4.1 and consists of the following steps:

(A) For the injection of the ions, the trapping potential V_0 applied to the endcap 1 electrode (closer to the ion source) is switched to 0 V. The ions can enter the trap and will be reflected by the potential V_0 applied to the endcap 2 electrode (further away from the ion source). After an injection time, typically 100 µs (negligible on the Fig. 4.1), endcap 1 is switched from 0 V to the trapping potential (typically V_0 is between 20 V and 60 V). Finally the ions are confined in the Penning trap. A delay

time of 10 ms after the injection can be introduced for cooling the axial and the cyclotron motions by collisions with rest gas particles.

(B) A dipolar excitation field at the magnetron frequency ν_- is applied with a duration $\tau_- = n/\nu_-$ defined by the number of periods n of the signal. Usually, between 8 and 16 periods for the excitation are used. The magnetron excitation causes the ions to move out of the center of the Penning trap to a magnetron radius, denoted by R_-.

(C) An azimuthal dipolar or quadrupolar rf excitation field with a duration τ_1 can be applied to the excitation ring electrode segments, as explained in Section 3.5.2. The excitation schemes for one- and two-pulse quadrupolar excitation fields have been already described in Fig. 2.4.

(D) After the excitation of the ion motion, the amplified ion signals are recorded for a detection time t_{tr}. A Fourier transformation of the discrete-time signals leads to the magnitude-mode frequency spectra, which are computed for each single segment and the dipolar and quadrupolar detection methods. From the frequency spectra the Fourier amplitudes at the eigenfrequencies, harmonics and sideband frequencies can be measured.

(E) For ejection, the trapping potential of the endcap 2 electrode is switched from V_0 to 0 V while endcap 1 is still at V_0. Then the ions fly towards a Faraday cup or an MCP detector for further studies.

The total trapping time is defined as the time difference between the injection and ejection of the ions. Typically one measurement cycle takes about 500 ms. After the ejection the measurement cycle starts again with the injection from step (A) in Fig. 4.1. Between each cycle, parameters such as excitation frequency, amplitude and time can be changed. In Chapter 5 more details about the parameters defining the timing scheme for the specific experiments will be given.

4.2 Trigger system and reference clock

Each step of the timing scheme from a measurement cycle is controlled by the trigger signal. The electronic devices are sequentially triggered. A box diagram of the communication between the devices is shown in Fig. 4.2 including the trigger signal, the clock signal and the ion signal lines between the devices. A timing generator (Berkeley Nucleonics Corp., 565 pulse/delay generator) delivers a 5 V TTL pulse, which triggers the whole measurement process. Two high-voltage (HV) switches are used (one from Behlke

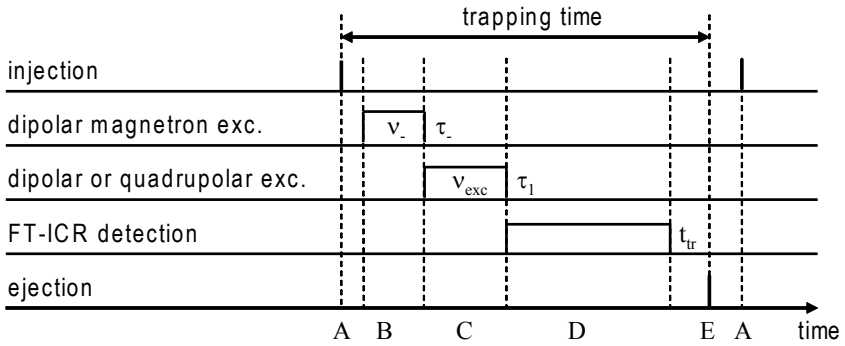

Figure 4.1: The timing scheme of a measurement cycle during which the ions are injected (A), excited (B) and (C), detected (D) and ejected (E). The trapping time is defined from the injection to the ejection of the ions. For more details see text.

GmbH, GHTS 30 A and one home made), both biased by the HV source with DC voltages.
The timing generator triggers simultaneously the HV switch for ion injection and the waveform function generators (Agilent, model 33250A Function / Arbitrary waveform generator, 80 MHz). After a delay time introduced by the function generator, the rf signals are generated for the excitation of an ion motion. These signals are carried via feedthroughs into the UHV chamber and further to a low-pass filter board. As seen in Fig. 3.4, the filter board is directly mounted on the Penning-trap support structure. The filter board is used to clean the rf signals as well as the trapping voltage from induced noise before the signals are applied to either the ring or the endcap electrodes.
After the ion excitation, the ion signals induced on the detection electrode are picked-up with a pre-amplifier, which is mounted directly on the Penning-trap housing. Then the ion signals are fed into a room-temperature post-amplifier, which is mounted on a flange outside the vacuum. After the two stages amplification, the signals are finally fed into the transient recorder (Spectrum GmbH, M2i.3026). After the ion excitation the transient recorder is triggered. Then the ion signals are recorded and the data acquisition is started by the FT-ICR control system (FT-ICR CS), as will be explained in Section 4.3.

The waveform function generator provides a reference clock, which is a square-wave signal at 10 MHz with ± 1 V. One function generator is used to synchronize the clocks of all the other function generators and the transient recorder. The reference clock avoids that the output rf signals are shifting in time against each other and the rf signals have a fixed phase relation between each other.
The transient recorder has an external clock input, which accepts only a square-wave clock signal from 0 to 3 V. Thus the reference clock signal from the function generator had to be

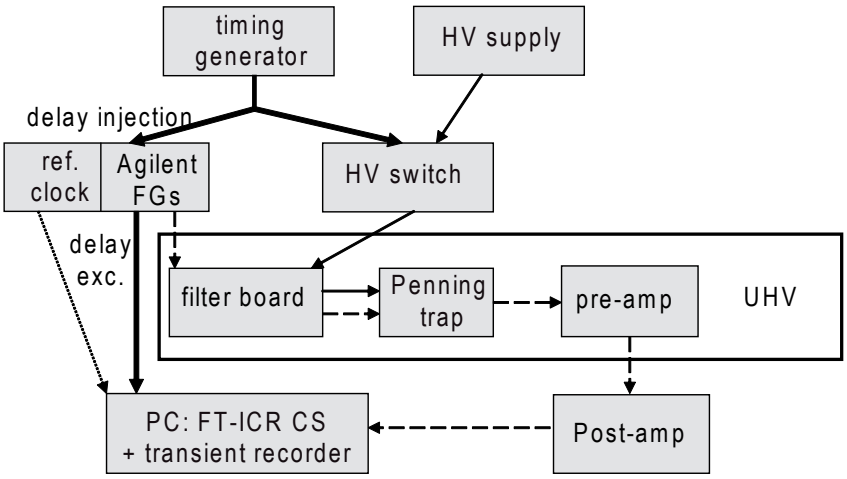

Figure 4.2: Box diagram of the communication between the electronic devices. The thick solid black arrows show the direction of the trigger signal. The thin black solid arrows show the signal for the trapping potential. The excitation and detection signal lines are shown as broken arrows. The signal for the reference clock is fed into the transient recorder and shown as a dotted arrow.

transformed. For this purpose, a 10 MHz amplifier is built. In principle, the circuit consists of a non-inverting amplifier with a high-speed operational amplifier.

4.3 The FT-ICR control system

An FT-ICR control system (FT-ICR CS) has been devolved to provide a convenient and flexible control of the experiment. The FT-ICR CS is based on the transient recorder program. The latter is extended to a full control system including a control of function generators, the HV source (Stahl-Electronics) and the transient recorder. The structure of the control system can be represented by several modules built together: the data acquisition (DAQ) module, the instrument control and the data analysis (DAN) modules. The main features of the FT-ICR CS are the following:

- Selection of different detection schemes like single-segment, dipolar and quadrupolar detection,
- Control of the function generators and the transient recorder,
- 1D and 2D scans of parameters like excitation frequency, amplitude and duration,
- Computing various frequency spectra and preliminary on-line data analysis.

The FT-ICR CS has been built in LabView 8.5[1]. Figure 4.3 shows the front panel of the FT-ICR CS Graphical User Interface (GUI). The FT-ICR CS implements the single-segment, the dipolar and the quadrupolar detection scheme (A), which can also be used in parallel. The FT-ICR CS computes six frequency spectra. For each of them the frequency settings can be defined individually (B). This allows the user to detect six different frequencies of one ion or several ion species simultaneously. Four out of the six frequency spectra are fitted with Gaussian functions. The fit parameters like the center frequency, the amplitude and the standard deviation are shown on-line (C).
The excitation parameters of the waveform function generators, i.e. the excitation frequency, amplitude, duration and the scan parameters can be set in a panel on the left bottom side of the GUI (D). The statistic parameters for averaging either the recorded discrete-time signals or the frequency spectra can be controlled from panel (E), as is explained later.
In another panel, which is not shown here, one can find the settings of the transient recorder. These are the sampling rate f_s, the number of samples N, trigger settings and the voltage level of each channel. The signals from the four detection segments are recorded simultaneously with the transient recorder. This is a fast 12 bit A/D converter board with a resolution of 12 bit for all four channels. The signals are recorded in discrete-time steps with a sampling rate of up to 60 MS/s. As mentioned before, the card can be externally triggered and clocked. A LabView library provided by the customer is used for the communication with the card.

This section is now subdivided into two parts. First, the working principle of the FT-ICR CS will be explained. Second, the basics of the Fast Fourier Transformation (FFT) algorithm will be shortly discussed. The FT-ICR CS uses the FFT to transform a signal from the time domain into the frequency domain.

Schematic working principle of the FT-ICR CS: Figure 4.4 shows a flowchart for the working principle of the FT-ICR CS starting with the initialization of the excitation parameters which are the excitation time, frequency and amplitude. The user can choose between a parameter scan or using a fixed set of parameters. The control system can be operated in two modes, either the single mode or the loop mode. In the single mode, the parameter scan is done once. In the loop mode the parameter scan is repeated many times. After each measurement cycle, the ion signals are recorded and the frequency spectra are computed. For a parameter scan, the start value a_{start} is after each measurement cycle incrementally increased with the step size Δa, i.e. $a_{i+1} = a_i + \Delta a$, until the stop value a_{stop} is reached. When the stop value is reached, there are two possibilities how to proceed: in

[1] National Instruments Germany GmbH, Ganghoferstrasse 70, 80339 München, Germany

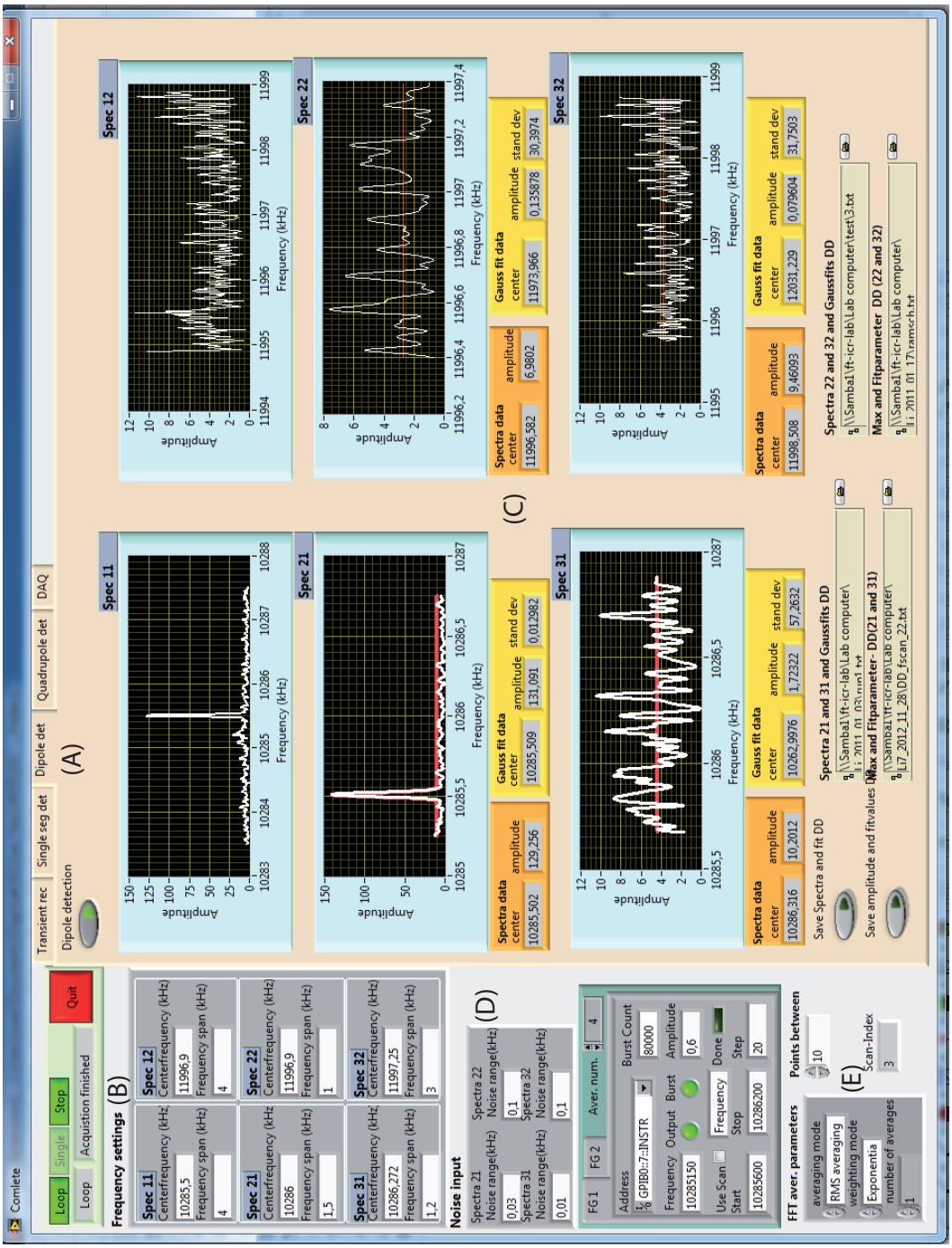

Figure 4.3: Front panel of the FT-ICR CS graphical user interface. The program consists of the following parts: (A) Different detection schemes can be chosen on-line, (B) frequency settings of the frequency spectra, (C) frequency spectra and fitting routine to the computed spectra, (D) control of the function generators settings and (E) statistic settings for the averaging.

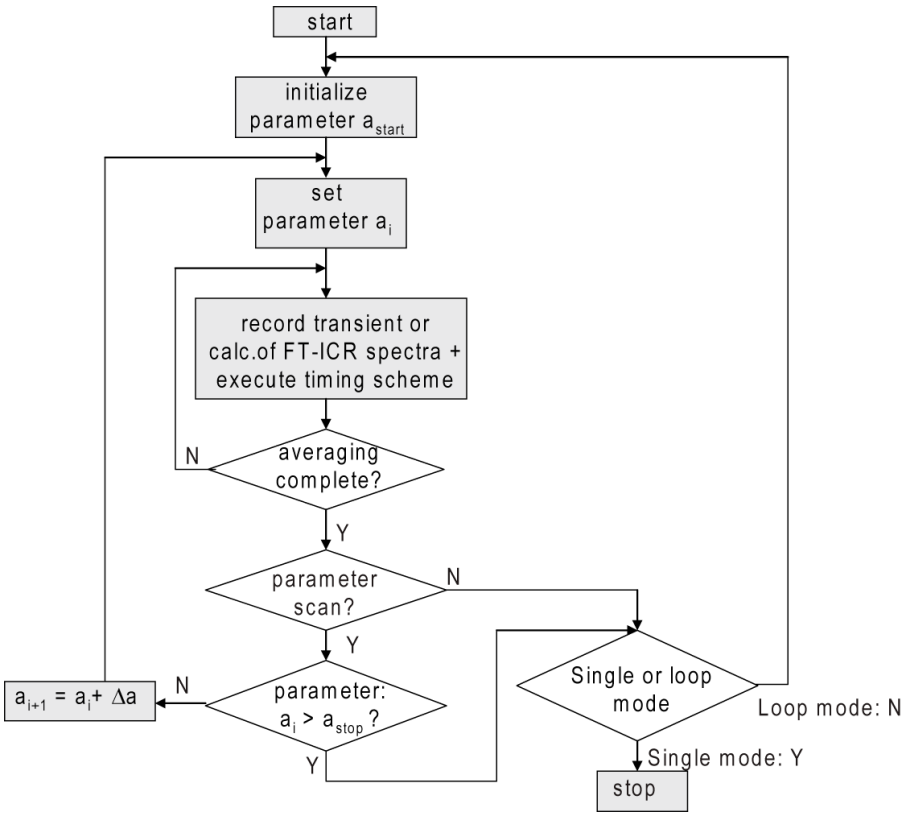

Figure 4.4: Flowchart representing the FT-ICR CS for the single and the loop modes for a fixed parameter a or a parameter scanned from a_{start} to a_{stop} with a step size Δa. The decision can be either Y for yes or N for no. For details see the text.

the single mode the control system stops the measurement cycle and in the loop mode the parameter scan starts again from the initialized starting value a_{start}.

In order to increase the signal-to-noise ratio of the measured signals, either the recorded discrete time signals or the frequency spectra or both can be averaged n-times. This increases the signal-to-noise ratio by a factor of $\sqrt{n}$. As seen from Fig. 4.4, the averaging process has to be completed before the cycle can continue. Thus it is possible to use the average of, e.g., the time-discrete signals, in combination with the loop mode.

It should be mentioned that the 2D-parameter scan is similar to the scan explained above. Here two parameters are scanned simultaneously. The first parameter is scanned many times. Each time the stop value is reached, the second parameter is incrementally increased by one step.

The Fast Fourier Transformation (FFT): The FT-ICR detection is based on the detection of the induced image charges of an ion. The signal in the time domain is Fourier transformed into the frequency domain. From the resulting frequency spectra the Fourier

amplitudes at the eigenfrequencies, sideband frequencies and the harmonics can be determined. The FT-ICR CS implements the FFTspectrum.vi[2] which computes the magnitude frequency spectrum from a discrete-time signal. The basics of the FFT will be discussed in the following.

The FFT is a fast algorithm to compute the Discrete Fourier Transform (DFT) [63]. The result of the FFT is exactly the same as for the DFT but the computing time of the FFT algorithm is much faster. For a signal with N samples, the computation of the DFT needs $O(N^2)$ arithmetical operations while the computation with the FFT of the same signal requires $O(N\log N)$ arithmetical operations. This is a substantial progress in speed and it reduces computation time drastically if long samples are computed. The algorithm used in an FFT is the so-called Cooley Tukey algorithm which can compute the N samples with $O(N\log N)$ operations [63]. The basic idea is that the algorithm breaks the N samples down into several computations of a DFT with a smaller size. After these two transformations the results are combined to a Fourier transformation. Now the basics of the DFT algorithm will be discussed.

First the DFT is defined in the mathematical sense, using an N-dimensional complex space $\mathbb{C}^N$. The orthonormal system is defined if and only if for all vectors v_n and v_m the condition [64]

$$\langle v_n, v_m \rangle = \delta_{n,m} \tag{4.1}$$

is fulfilled, where $\delta_{n,m}$ is the Kronecker Delta, i.e. it is 1 if $n = m$ and 0 otherwise. $\langle \cdot, \cdot \rangle$ is the inner product defined over $\mathbb{C}^N$. A vector $y \in \mathbb{C}^N$ is uniquely described in this orthonormal system by

$$y = \sum_{n=0}^{N-1} \langle y, v_n \rangle v_n, \tag{4.2}$$

where the coefficients $\langle y, v_n \rangle$ are called the Fourier coefficients with respect to the basis. The orthonormal basis is defined as the n-th root of unity as complex values, $v_n = e^{-i2\pi nk/N}$ with $n, k \in \{0, .., N-1\}$ [65]. Using the definition of the inner product, the Fourier coefficients $\hat{y}_n$ of a vector y are given by

$$\hat{y}_n = \langle y, v_n \rangle = \sum_{k=0}^{N-1} y_k e^{-i2\pi \frac{kn}{N}}, \tag{4.3}$$

where $k \in \{0, .., N-1\}$. The DFT of a vector y has the Fourier coefficient $\hat{y}_n$ with respect to the basis vector v_n. One should notice that the spectrum is symmetric due to the property of the DFT coefficients $\hat{y}_{N-n} = \hat{y}_{-n}$ for a real signal in the time domain.

[2]This is a virtual instrument of National Instruments.

Equation (4.3) can be interpreted as a discrete Fourier transformation of a discrete-time signal $y = (y_0, ..., y_{N-1})$, i.e. a signal with N samples, into the frequency domain with the Fourier coefficients $\hat{y} = (\hat{y}_0, ..., \hat{y}_{N-1})$. In practice a time signal will be uniformly sampled with a time interval $\Delta t = 1/f_s$ defined by the inverse of the sampling frequency. The total time is given by the number of samples N, i.e. $t_{tr} = N\Delta t = N/f_s$. The bin size is defined by the inverse of the total time $\Delta\nu = f_s/N = 1/t_{tr}$. One has to take care of aliasing effects which can lead to distortions. An alias free sampling of a time discrete signal is guaranteed if the Nyquist theorem is satisfied, i.e. the sampling rate is at least twice the maximum frequency ν of the signal, $f_s = 2\nu$. From the Fourier coefficients the magnitude mode spectra are calculated by

$$W_n = \sqrt{Re(\hat{y}_n)^2 + Im(\hat{y}_n)^2}. \tag{4.4}$$

The virtual instrument from LabView computes the root-mean-square (RMS) of the magnitude W_n, where the unit is given in Volt. Typically, for recording the discrete-time signal a total time of 100 ms with a sampling rate of 40 MHz is used, which corresponds to 4 million samples for each channel. Thus, a bin size of 10 Hz in the frequency spectra is obtained. As mentioned in Section 2.3.2, the recorded time signals can be analyzed using the differential signal, the sum signal or the signal from one segment. The FFT of the resulting signals computes the dipolar, the quadrupolar and the single segment frequency spectra, where the Fourier coefficients are defined in Eq. (4.4).

The bin size of 10 Hz limits drastically the accuracy for a frequency determination. The bin size can be further decreased when a spline interpolation between the computed Fourier components $\hat{y}_k$ is used. A spline interpolation uses a piecewise polynomial functions to interpolate between points. The spline interpolation is done with 9 points, so that it results in a bin size of 1 Hz. This method was tested in the following way. A 10 MHz rf signal of a function generator was tuned in one Hertz steps and the signals were recorded with the transient recorder. The measured frequency from the frequency spectrum shows the corresponding one Hertz steps.

4.4 Characterization of the broad-band amplifier for FT-ICR detection

For increasing the signal-to-noise ratio of the induced ion charges, broad-band pre- and post-amplifiers are used. As discussed in Section 2.3.4 the induced charges on the detection electrodes are treated as an ideal current source which loads the trap capacitance as well as the amplifier's input capacitance. The resulting voltage signal is then amplified by

a voltage amplifier designed by Stahl Electronics [59]. We present here the characterization of two such pre-amplifiers used for different purposes. The first one is a cryogenic pre-amplifier developed for the KATRIN project, which was designed for a final temperature of 77 K. But in march 2012 the KATRIN collaboration decided that, due to problems at the DPS, the whole DPS will be new designed and finally operated at room temperature. The second one is a room temperature pre-amplifier used at the FT-ICR setup in Heidelberg. For both pre-amplifiers results for the voltage amplification and the noise densities are reported. Concerning the post-amplifier identical ones are used at the KATRIN project and for the setup at MPIK. Its characterization is also determined.

4.4.1 Pre-amplifiers

Both pre-amplifiers are designed as voltage amplifiers and have a nearly identical design of the electrical circuits. A schematic view of the pre-amplifier is shown in Fig. 4.5 (a). The first stage of the amplifier circuit forms a common-source amplifier with a junction field effect transistor (FET). This circuit represents a voltage amplifier with an input impedance of 10 MΩ. The second stage is a common-drain amplifier, which is used as a voltage buffer having a low output impedance. In this stage the signal input is connected to the gate of an FET and the source delivers the output signal with an output impedance of approximately 75 Ω. The difference between the KATRIN pre-amplifier and the Heidelberg pre-amplifier is that the first one uses two gallium arsenide (GaAs) FET's for operation at cryogenic temperatures, while the latter one uses two silicon FET's. These design differences are due to the strong temperature dependence of the conductivity in the semiconductor.

For the amplification of ion signals one has to choose a front-end FET with a small gate-to-drain capacitance which couples the drain-to-source resistance of the FET to its input. A low input voltage-noise density is needed in order to increase the signal-to-noise ratio of a measured ion signal. For avoiding parasitic reactive contributions one has to use surface mountable devices (SMD) and components with low loss tangents to avoid noise caused by ohmic dissipation. The loss tangent is defined as the angle between the resistive and the reactive component of an electromagnetic field in a dielectric material.

Figure 4.5 (b) shows an assembly of the KATRIN pre-amplifier on a board with two channels. The print circuit board (PCB) is made of FR4 dielectric material which has been tested at cryogenic temperatures. It has a dielectric constant of 4.2 and a low loss tangent of approximately 0.02, which means a low parasitic capacitance. The detection electrode is capacitively coupled to the input of the pre-amplifier, which is mounted directly on the Penning trap electrode support structure. This way the distance between the detection

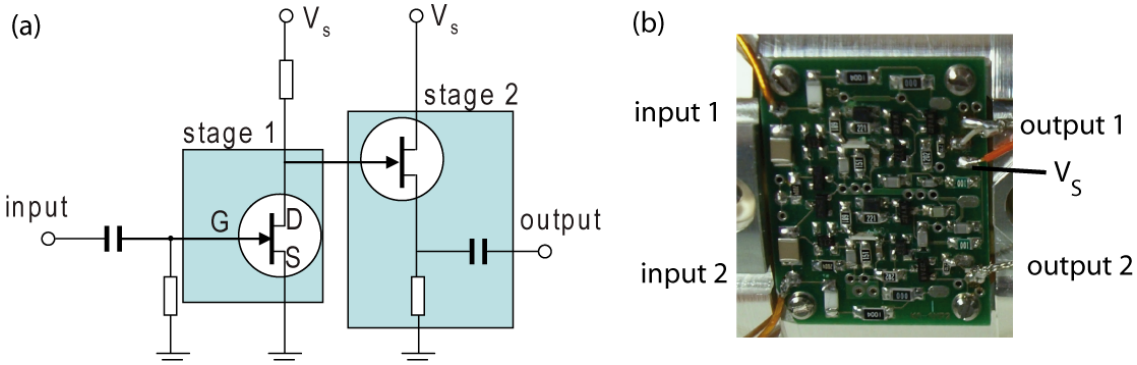

Figure 4.5: (a) Schematic circuit diagram of the voltage pre-amplifier used for the KATRIN project as well as for the FT-ICR setup in Heidelberg. The first stage is an inverting input amplifier and the second stage is a voltage buffer for converting the high impedance to a low output impedance. Panel (b) shows a photograph of the pre-amplifier board with two independent but equal channels. The printed circuit board has a size of 26x32 mm^2 and is mounted on the support structure of the Penning trap only 4 cm away from the detection electrodes.

electrode and the subsequent pre-amplifier is minimized, reducing noise pick-up and parasitic capacitances. The amplified ion signals are carried via cryogenic compatible coaxial cables to a four-channel post-amplifier for further amplification. The post-amplifier is attached to a vacuum flange outside of the UHV chamber.

A careful matching of electrical elements results in the same characteristics for amplification, voltage and current noise of both channels. Both channels of the pre-amplifier were tested and the same results of amplification and voltage noise are measured. Therefore, the results for one channel are presented in the following sections. Notice that the results for the voltage and current-noise density are shown in units of $\mathrm{V}/\sqrt{\mathrm{Hz}}$ and $\mathrm{A}/\sqrt{\mathrm{Hz}}$, respectively.

Cryogenic pre-amplifier for the KATRIN project

The voltage amplification is determined by measuring the forward transmission with a network analyzer (ZVL from Rohde & Schwarz). The rf signal from the network analyzer with an output impedance of 50 Ω is fed into the pre-amplifier with a high impedance input of 10 MΩ. The amplified rf signal is read out with a network analyzer which has an input impedance of 50 Ω. The measured forward transmission coefficient $S_{2,1}$ is lastly modified by the impedance matching of the source to the load. For the tests, the pre-amplifier is mounted into a high-frequency (hf) shielded box which is submerged into liquid nitrogen.

All tests of the KATRIN pre-amplifier have been performed at 77 K. Figure 4.6 shows

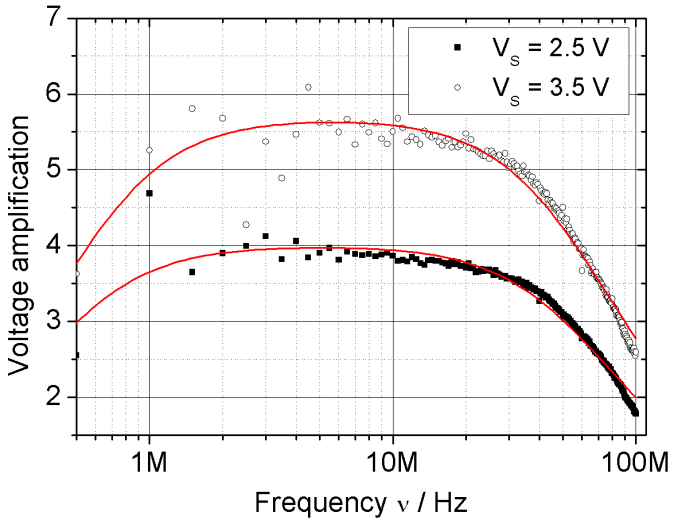

Figure 4.6: Voltage amplification of the cryogenic pre-amplifier for the KATRIN project. The data were measured at 77 K for two different biasing voltages V_s. The red line is a fit of a low- and a high-pass filter function to the data. For both data sets one obtains the cut-off frequency $\nu_{lp} = 56$ MHz.

the voltage amplification for the KATRIN pre-amplifier for a DC biasing V_s of 2.5 V and 3.5 V. The biasing voltage is delivered by a home-made voltage source. A constant voltage gain of roughly 4 and 5.5 is determined in a frequency range from 2 to 10 MHz. For both data sets a high and low-pass behaviour of the voltage amplifier is observed. A filter function is fitted to the data, delivering the cut-off frequencies $\nu_{lp} = 56$ MHz at the 3 dB loss of voltage amplification. Below a frequency of 1 MHz less data points are measured. From this results a deviation of the data to the high-pass filter curve. The broad-band frequency amplification fulfills the requirements for detecting the different ion species and clusters (He^+, T^+, T_3^+, T_5^+, ...) [50, 47], which are expected in the ion flux of the KATRIN beam line. For these ions the cyclotron frequencies are between 5 and 26 MHz, which is covered by the broad-band amplifier.

The voltage noise input density is determined in the following way: The input of the pre-amplifier is grounded and the output signal was fed into a subsequent broad-band ultra low-noise amplifier (SA-230F5 from NF Corporation). This amplifier has a voltage gain G_2 of 200 in a frequency range from 400 Hz to 140 MHz and a voltage noise density e_{n2} of $0.35\,\mathrm{V}/\sqrt{\mathrm{Hz}}$. The output of the SA-230F5 is fed into an FFT spectrum analyzer (Picoscope 3224 from Pico Technology Ltd.) which measures the voltage noise at its input. In order to reduce aliasing effects of the spectrum analyzer a low-pass filter with a cut-off frequency of 4 MHz was introduced at its input.
To yield the input voltage noise density, the measured FFT data have to be divided by

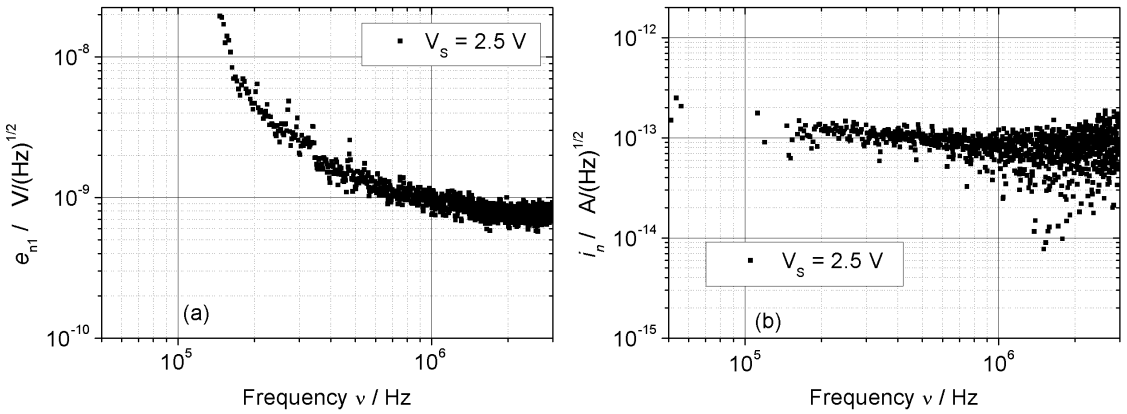

(a) (b)

Figure 4.7: Results of the noise characterization of the cryogenic pre-amplifier for the KATRIN project operated at 77 K: Panel (a) shows the measured voltage noise density as a function of the frequency for a biasing voltage of 2.5 V. (b) Resulting current noise density when a capacitance of 9.1 pF was connected to the input of the pre-amplifier. The intrinsic amplifier input capacitance of 5.3 pF was considered.

the square-root of the band width of the internal filters of the spectrum analyzer. The second amplifier with its high gain G_2 is used to amplify the voltage noise. This reduces the contribution of the internal noise of the spectrum analyzer e_{sa} compared to the measured voltage noise. When determining the total noise density e_{m} at the input of the spectrum analyzer, the input voltage noise density e_{n1} of the pre-amplifier with a gain G_1 is calculated by

$$e_{\mathrm{n1}} = \sqrt{\frac{e_{\mathrm{m}}^2 - e_{\mathrm{sa}}^2}{G_1^2 G_2^2} - \frac{e_{\mathrm{n2}}^2}{G_1^2}}. \tag{4.5}$$

Figure 4.7 (a) shows the resulting voltage noise density as a function of the frequency for a bias voltage of 2.5 V measured at 77 K. The noise density decreases approximately with $1/\sqrt{\nu}$ up to the corner frequency of roughly 1 MHz. This noise contribution is known as Flicker noise. The discontinuity of the $1/\sqrt{\nu}$ behaviour below 300 kHz is due to less data points at the voltage gain curve describing the filter function, as mentioned above (see Fig. 4.6). Thus small deviations from the high-pass filter lead to a larger slope than expected. Beyond the corner frequency at 1 MHz, a frequency independent voltage noise density of 1 nV/$\sqrt{\mathrm{Hz}}$ is measured, which is known as white noise.

The measurement of the current noise density is rather similar to the voltage noise density measurement. Here a capacitor with a capacitance of $C_{\mathrm{m}} = 9.1$ pF was connected in parallel to the pre-amplifier and to the ground. The input current charges the input

capacitance C_{in} of the pre-amplifier and the parallel capacitance C_{m}. Similar to the voltage noise measurement the signal was further amplified by the amplifier SA-230F5 and finally measured with the FFT analyzer. At its input the voltage noise density $e_{\mathrm{n1,C}}$ was detected. Since the voltage noise density e_{n1} input is known, the input current noise density i_{n} can be determined with

$$i_{\mathrm{n}} = 2\pi\nu\,(C_{\mathrm{in}} + C_{\mathrm{m}})\,\sqrt{e_{\mathrm{n1,C}}^2 - e_{\mathrm{n1}}^2}. \tag{4.6}$$

To determine the current noise density the input capacitance C_{in} has to be determined. This was measured by soldering a 5 kΩ SMD resistor in series to its input and measuring the cut-off frequency of the corresponding low-pass filter curve. This measurement yields an input capacitance of $C_{\mathrm{in}} = 5.3\,\mathrm{pF}$.
Figure 4.7 (b) shows the current noise density as a function of the frequency measured at 77 K with a bias voltage of 2.5 V. The data points show a constant value of $100\,\mathrm{fA}/\sqrt{\mathrm{Hz}}$ in a frequency range from 0.2 to 1 MHz. Beyond 1 MHz the current noise density increases slowly to $160\,\mathrm{fA}/\sqrt{\mathrm{Hz}}$ in a range from 1 to 4 MHz. The reason can be that a drain-gate capacitance C_{DG} contributes to the input resistance. The voltage and current noise density of the pre-amplifier are sufficient to detect the induced current of a few thousand ions. A detection limit studies is presented in [47].

Room temperature amplifier system for the Heidelberg FT-ICR setup

The ion image charge detection system at the FT-ICR setup uses a pre- and subsequent post-amplifiers which are operated at room temperature. Since four out of the eight segments from the ring electrode of the Penning trap are used for detection, two pre-amplifiers each of two channels are needed. The pre-amplifier is biased by a constant voltage of 5 V, which is supplied by a voltage source placed on the post-amplifier.

Similarly as described in Section 4.4.1 the amplifier is mounted into an hf shielded box. The voltage amplification and the noise density measurements were performed at room temperature. Since both channels of the pre-amplifier show identical results the data will be again presented for only one channel. Figure 4.8 (a) shows the voltage amplification of the pre-amplifier as a function of the frequency. The pre-amplifier has a voltage gain of 6.2 in a wide frequency range from 0.2 to 20 MHz. Again a filter functions is fit to the data which gives the cut-off frequency $\nu_{\mathrm{lp}} = 31\,\mathrm{MHz}$. For ion signals at eigenfrequencies of roughly 10 MHz for $^7\mathrm{Li}^+$ and 12 MHz for $^6\mathrm{Li}^+$ equal voltage amplification was ensured.
Figure 4.8 (b) shows the resulting voltage noise density for the pre-amplifier. A frequency independent noise, the so-called white noise, of $1\,\mathrm{nV}/\sqrt{\mathrm{Hz}}$ is detected in the range from 0.1 to 3 MHz. The Flicker noise appears for silicon FET's at lower frequencies.

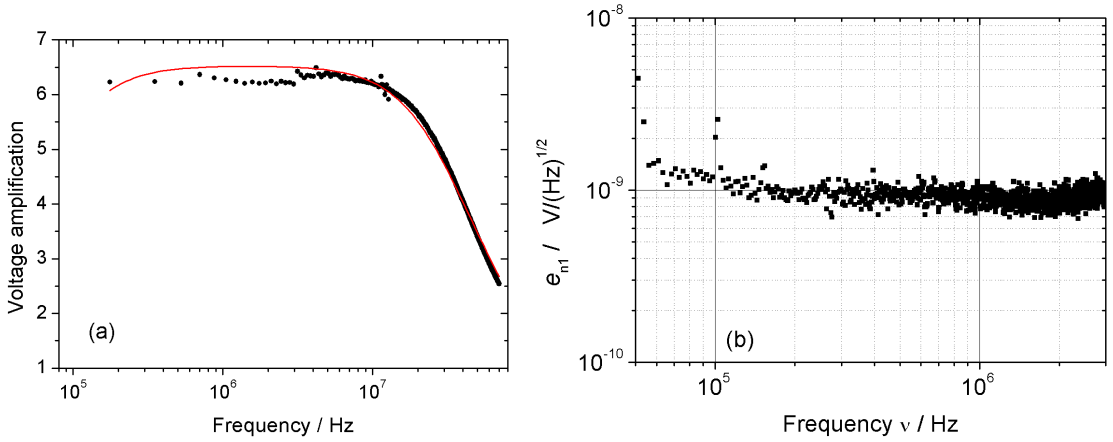

Figure 4.8: (a) Voltage amplification of the pre-amplifier measured at room temperature, as used at the FT-ICR setup in Heidelberg. The data are fit with a filter function (solid red curve), which results in $\nu_{\mathrm{lp}} = 31\,\mathrm{MHz}$. (b) The measured voltage noise density has only a white noise contribution.

4.4.2 Post-amplifier

The post-amplifier has four identical channels and has been built by Stahl Electronics. The output impedance of the pre-amplifier matches with the input impedance of 75 Ω of the post-amplifier. The output impedance is 150 Ω. The post-amplifier can be operated in magnetic fields up to 25 mT [59]. The voltage amplification was measured with a network analyzer, similar as described before and the results are shown in Figure 4.9. A constant voltage amplification of 75 in a frequency range from 0.1 to 4 MHz was determined. Then the amplification increases to a maximum gain of 100 at 13 MHz. At frequencies higher than 30 MHz the low-pass behaviour decreases the voltage amplification again. This frequency range is not of interest for the results presented in this thesis.

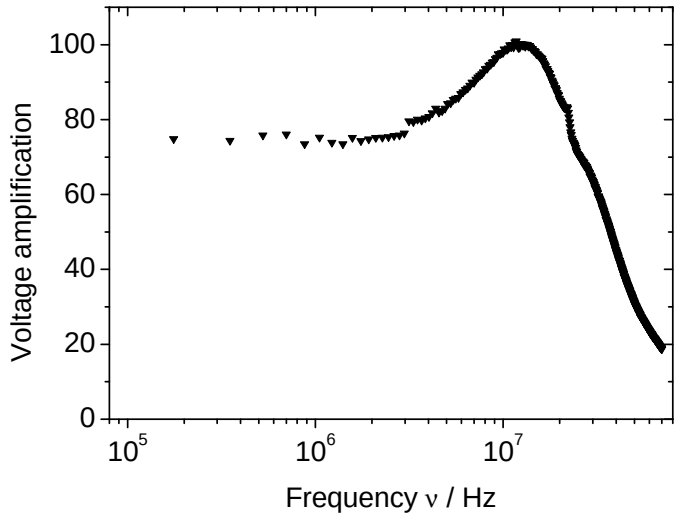

Figure 4.9: Transfer function of the the post-amplifier system used at the FT-ICR setup in Heidelberg.

Chapter 5

FT-ICR results and discussion

In this chapter the experimental results using the FT-ICR setup are presented and discussed. The setup uses the FT-ICR detection system already presented in the previous chapter. First of all, various methods for the eigenfrequencies determination are discussed. Then, the FT-ICR frequency spectra are studied for the dipolar and quadrupolar detection methods.

The conversion of motional modes due to the application of a one- or a two-pulse (Ramsey) quadrupolar excitation field has been investigated. The FT-ICR signal has been probed by changing the parameters of the quadrupolar excitation field such as the excitation frequency, duration, amplitude, and waiting time. The theoretical prediction are compared with the experimental results.

For the measurements presented in this chapter, typically 10^5 ions are stored simultaneously in the Penning trap. Therefore, effects due to space charge are present in the Penning trap and deviations from the single particle description occur. The phenomena due to space charge were experimentally observed and are presented here for the dipolar and the quadrupolar excitation methods. Many-ion simulation studies were carried out with the SIMBUCA program [66] in order to compare simulations with the experimental results.

Since the Penning trap will be used in the KATRIN experiment for mass identification, accuracy limit studies are of high importance. Here, results are presented for the frequency ratio determination of the lithium isotopes $^7Li^+$ and $^6Li^+$ and compared to the well-known literature value.

5.1 FT-ICR amplitudes in the dipolar and the quadrupolar spectra

In this section various methods for the determination of the azimuthal eigenfrequencies are discussed. With the well-known frequencies the ions can resonantly be excited. The dipolar and quadrupolar detection methods were used to obtain the FT-ICR spectra for $^7Li^+$ and $^6Li^+$.
The dependency of the resonance frequencies on the trapping potential has been studied by using the Penning trap with a four-fold segmented ring electrode. These results can also be found in [67].

5.1.1 General remarks on the FT-ICR spectra

The measurement of the ion signal with the broad-band FT-ICR detection technique is only possible if the induced image charges are greater than the noise caused by the pre-amplifier. For the broad-band detection system described in Section 4.4, the signal-to-noise ratio (SNR) can be calculated. For example, according to Eq. (2.80), 100 fA ion current induced on the detection electrodes with a detector capacitance of 10 pF leads to an SNR of $0.04 \times N_{\mathrm{ion}}$, assuming an ion cyclotron radius R_+ of 2 mm. This current is converted into a voltage which is finally measured. For the studies presented here, roughly 10^5 trapped particles per measurement cycle are detected. Since the pre-amplifier has a low noise density of $1\,\mathrm{nV}/\sqrt{\mathrm{Hz}}$ at frequencies larger than 100 kHz, the modified cyclotron frequency $\tilde{\nu}_+$ and also magnetron sidebands (e.g. $\tilde{\nu}_+ + \tilde{\nu}_-$, $\tilde{\nu}_+ + 2\tilde{\nu}_-$) as well as higher harmonics $2\tilde{\nu}_+$ can be detected. As a general remark, the measured frequencies in this section are denoted with a tilde, i.e. $\tilde{\nu}_+$, $\tilde{\nu}_-$ and $\tilde{\nu}_c$, in contrast to the eigenfrequencies for an ideal trap (ν_+, ν_-, and ν_z), as defined in Section 2.1.1. The deviations are due to systematic offsets as explained in Section 2.1.2. They are discussed in detail in Section 5.6.

The FT-ICR detection of an ion signal is as follows: After the excitation of the ion motion at the ion's eigenfrequency, the induced signals on the detection electrodes are amplified and recorded with the transient recorder. In this section the discrete-time signals were recorded with a duration of 100 ms at a sampling rate of 40 MHz. The dipolar and the quadrupolar detections were used and the FFT was computed resulting in the dipolar and the quadrupolar frequency spectra. The FT-ICR frequency spectrum shows the computed Fourier amplitude $W_\nu^{\mathrm{d,q}}$ at a frequency ν. The upper index (d,q) denotes the dipolar or quadrupolar detection method, respectively. The amplitudes are measured in Volt.

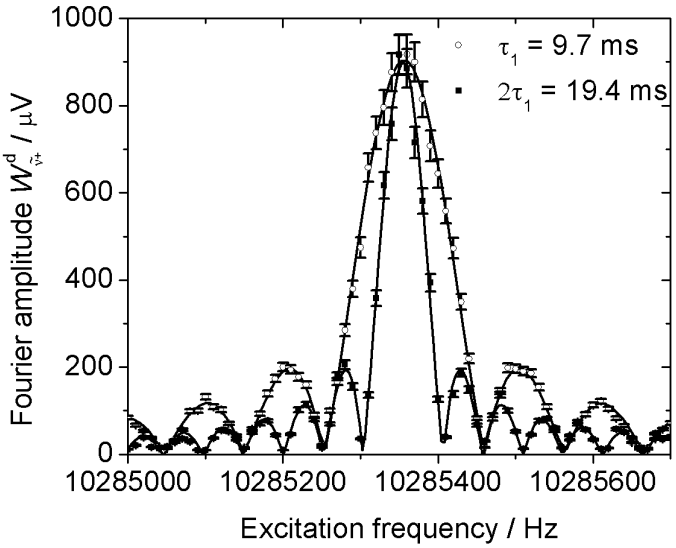

Figure 5.1: Resonance curve for a dipolar excitation pulse with an excitation duration of $\tau_1 = 9.7\,\text{ms}$ (open circles) and $2\tau_1 = 19.4\,\text{ms}$ (black circles) for $^7Li^+$. The Fourier amplitude $W^d_{\tilde{\nu}_+}$ at $\tilde{\nu}_+$ is plotted against the excitation frequency ν_{exc}. The solid lines are fits of the theoretical resonance curve defined in Eq. (2.32) to the data. The frequency at the center of the central peak corresponds to the modified cyclotron frequency $\tilde{\nu}_+$ of the ion.

5.1.2 Resonance scans for frequency determination

The eigenfrequencies $\tilde{\nu}_+$ and $\tilde{\nu}_-$ of the ion species have to be determined in order to perform experiments. With the knowledge of these frequencies the ion motion can be precisely manipulated. They can be determined from a resonance scan. For this, a dipolar rf field was applied and the excitation frequency ν_{exc} was scanned around the expected eigenfrequency. At each excitation frequency ν_{exc}, the Fourier amplitude at either the modified cyclotron frequency or the sideband frequency was measured. The maximum amplitude is reached when the excitation frequency is on resonance, i.e. equal to the eigenfrequency. Here, resonance scans of an azimuthal dipolar electric field for determining $\tilde{\nu}_+$ and $\tilde{\nu}_-$ are presented.

Determination of $\tilde{\nu}_+$ with a dipolar detection at $\tilde{\nu}_+$

The frequency of a dipolar excitation rf field was scanned $\pm 600\,\text{Hz}$ around the expected eigenfrequency $\tilde{\nu}_+$ of $^7Li^+$ with an excitation time of $\tau_1 = 9.7\,\text{ms}$ and $2\tau_1$. Figure 5.1 shows the dipolar Fourier amplitude $W^d_{\tilde{\nu}_+}$ measured at $\tilde{\nu}_+$ as a function of the excitation frequency ν_{exc}. For obtaining equal Fourier amplitudes at the resonance frequency $\tilde{\nu}_+$,

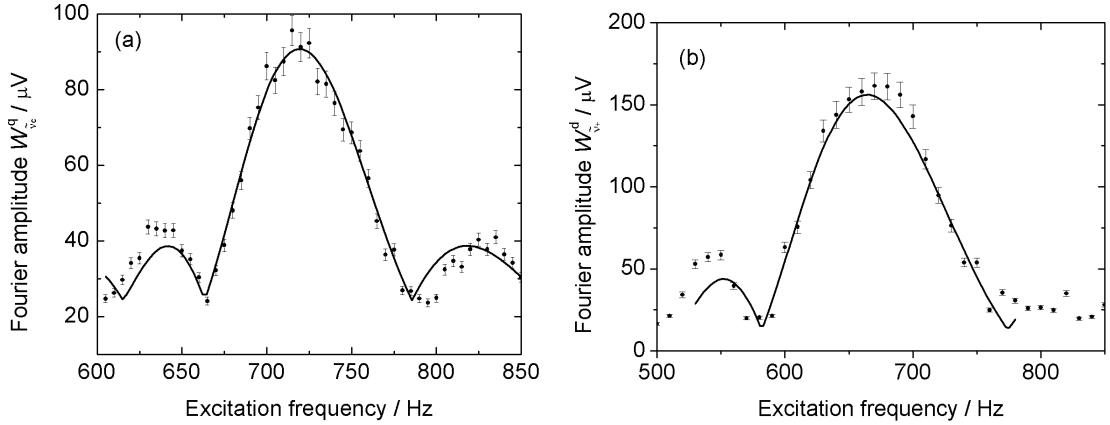

Figure 5.2: Results from two methods to determine the magnetron frequency are illustrated. (a) A dipolar excitation around $\tilde{\nu}_-$ with a quadrupolar detection of the Fourier amplitude $W^{\mathrm{q}}_{\tilde{\nu}_\mathrm{c}}$ at $\tilde{\nu}_\mathrm{c}$ for a trapping potential of 60 V. The maximum is observed when a resonant excitation is applied at $\tilde{\nu}_-$. (b) Resonant quadrupolar conversion at $\tilde{\nu}_\mathrm{c}$ of an initial magnetron motion into a pure cyclotron motion for a trapping potential of 55 V. The dipolar Fourier amplitude $W^{\mathrm{d}}_{\tilde{\nu}_+}(\nu_{\mathrm{exc}})$ is shown as a function of the excitation frequency. The solid lines is a fit of the theoretical line profile function to the data (see Eq. (2.32)).

the excitation amplitude of the dipolar rf field was reduced to the half for the excitation time $2\tau_1$. The measured amplitude $W^{\mathrm{d}}_{\tilde{\nu}_+}$ is proportional to the cyclotron radius R_+ of the detected ions. The largest cyclotron radius R_+ is measured when the excitation frequency is equal to the modified cyclotron frequency $\tilde{\nu}_+$. As expected, the cyclotron radius depends on the excitation frequency of the applied dipolar rf field. The distance between each minima for an excitation time of τ_1 is two times larger than for an excitation time of $2\tau_1$, as expected from theory. Both data sets are fit with the theoretical line shape of a finite excitation pulse given by a sinus cardinalis (see Eq. (2.32)). The modified cyclotron frequency $\tilde{\nu}_+$ is determined to be 10 285 354.7 Hz with a statistical uncertainty of 0.2 Hz. The Fourier limit (see Eq. (2.33)) is in agreement with the measured widths of the resonance peaks, $\Delta\tilde{\nu}_+ = 125$ Hz and 63 Hz, respectively. The resolving power can be further increased if longer excitation times are used.

Determination of $\tilde{\nu}_-$ with a quadrupolar detection at $\tilde{\nu}_\mathrm{c}$

The magnetron frequency could be determined by using the following method: First, a dipolar excitation field was applied and its excitation frequency was scanned around the expected $\tilde{\nu}_-$. Here, a fixed number of cycles was used, yielding an excitation duration of $\tau_1 = 8/\nu_{\mathrm{exc}}$. Thus, τ_1 depends on the excitation frequency. Then a dipolar excitation at $\tilde{\nu}_+$

was used to manipulate the cyclotron motion of the $^7Li^+$ ions. The ions were trapped at a trapping potential V_0 of 60 V.
In this measurement the cyclotron radius R_+ was kept constant while the magnetron radius depends on the applied frequency ν_{exc}. Figure 5.2 (a) shows the quadrupolar Fourier amplitude $W^q_{\tilde{\nu}_c}$ at the sideband frequency $\tilde{\nu}_c$ as a function of the excitation frequency. The Fourier amplitude is proportional to R_+R_-, as seen from Eq. (2.70). The resonance scan shows a maximum at $\tilde{\nu}_-$ which is equivalent to the largest magnetron radius. The data were fit with the theoretical line shape $R_-(\nu_{exc})$ given by Eq. (2.32) resulting in a magnetron frequency $\tilde{\nu}_-$ of 719.1(7) Hz. The relative uncertainty is 1×10^{-3}. In panel (a) of Fig. 5.2 it is observed that the minimum on the left side of the central peak are closer to the maximum than on the right side. This is due to the fact that a smaller excitation frequency causes a longer excitation duration, i.e. $\tau_1 = 8/\nu_{exc}$. Thus, the line-width of the excitation signal decreases with τ_1, which causes the asymmetric resonance form.

Determination of $\tilde{\nu}_-$ with a dipolar detection at $\tilde{\nu}_+$

The magnetron frequency can also be determined from the following method, possible only if the sideband frequency is known. A quadrupolar electric field was used to convert any initial magnetron motion into a pure cyclotron motion. First a dipolar magnetron excitation with a duration of $\tau_1 = 8/\nu_{exc}$ was applied. The frequency was scanned around the expected eigenfrequency $\tilde{\nu}_-$. This defines the initial magnetron motion $R_-(0)$ at time zero. Then a quadrupolar rf field at the sideband frequency $\tilde{\nu}_c$ with a pulse duration τ_2 equal to the conversion time τ_c was applied. This method uses the conservation of the sum of the square of the mode amplitudes ($R^2_-(0) = R^2_-(t) + R^2_+(t)$), as pointed out in Eq. (2.53). Thus a quadrupolar excitation at $\tilde{\nu}_c$ with a duration τ_c results in the final cyclotron radius $R^2_+(\tau_c) = R^2_-(0)$.

Figure 5.2 (b) shows the dipolar Fourier amplitude $W^d_{\tilde{\nu}_+}$ as a function of the excitation frequency. The resulting resonance shows the same behaviour as for a short pulse dipolar excitation. The maximum is measured at the magnetron frequency $\tilde{\nu}_- = 664(2)$ Hz using a trapping voltage V_0 of 55 V. The magnetron frequency $\tilde{\nu}_-$ could be determined with a relative uncertainty of 3×10^{-3}.

Both methods for the magnetron frequency determination presented in Fig. 5.2 have comparable relative uncertainties. The second method has a three times higher statistical uncertainty because only the central peak is fit to the data. One can see in Fig. 5.2 that the theoretical description does not follow the sidebands on the left and the right side of the resonance frequency $\tilde{\nu}_-$. An explanation can be that the phase difference between the applied excitation field and the magnetron motion of the ions changes alternatively. The ions are parallel or anti-parallel to the excitation field which leads to a decrease or an

increase of the magnetron radius, respectively. A phase difference of π appears already after a time of 4.5 ms when a detuning of 110 Hz with respect to $\tilde{\nu}_-$ is applied. However, this still needs to be further investigated.

5.1.3 Comparison of the dipolar and the quadrupolar FT-ICR spectra

When the eigenfrequencies $\tilde{\nu}_+$ and $\tilde{\nu}_-$ of the ions are known, the ion motion can be manipulated with a dipolar excitation field. In this section the frequency spectra for the dipolar and the quadrupolar detection methods are presented using the Penning trap with the eight-fold segmented ring electrode. Figure 5.3 (a) shows the frequency spectrum for $^7Li^+$ and $^6Li^+$ ions resulting from the dipolar detection method. For this measurement both lithium isotopes are excited at their eigenfrequencies $\tilde{\nu}_+$ using a dipolar rf field. The Fourier amplitude $W^{\mathrm{d}}_{\tilde{\nu}_+}$ is in first order proportional to the cyclotron radius R_+ (see Eq. (2.68)), and to the number of ions. For the $^7Li^+$ ions the SNR is determined to be 23 and for the $^6Li^+$ ions to be 3. The signal from $^7Li^+$ is higher, which is expected due to the isotopic abundance of 93% for $^7Li^+$ compared to 7% of $^6Li^+$. The blue line is a Gaussian fit to the Fourier signal, which results in the fit-parameters such as the amplitude, the center frequency and the line-width.

Figure 5.3 (b) shows the frequency spectrum for $^7Li^+$ ions when the quadrupolar detection was used. The Fourier amplitudes $W^{\mathrm{q}}_{\tilde{\nu}_\mathrm{c}}$ and $W^{\mathrm{q}}_{2\tilde{\nu}_+}$ could be detected. The Fourier amplitude at $\tilde{\nu}_\mathrm{c}$ is proportional to R_+R_- (see Eq. (2.70)). Therefore, an additional dipolar excitation field at $\tilde{\nu}_-$ was needed for this measurement, thus the ions perform a magnetron motion and a cyclotron motion. The Fourier amplitude at the second harmonic $2\tilde{\nu}_+$ is proportional to R_+^2 as stated in Eq. (2.72). This signal arises from the quadrupolar detection geometry. During one period of the cyclotron motion the image charges of the ions induced on the opposing detection electrodes are also detected and the signals are summed. The resulting quadrupolar signal is thus modulated with twice the ion's eigenfrequency.

The frequency resolution is naturally Fourier limited by the observation time of the ion signal. The line-widths $\Delta\nu$ of the signals at $\tilde{\nu}_+$ and $2\tilde{\nu}_+$ are identical and roughly equal to 18 Hz for a total time of 100 ms. The frequency resolving power $\tilde{\nu}_+/\Delta\nu$ is roughly $6\cdot10^5$.

Notice that in addition to the methods for the magnetron frequency determination presented in Fig. 5.2, the $\tilde{\nu}_-$ can also be determined in this way. The modified cyclotron frequency $\tilde{\nu}_+$ is measured with the dipolar spectra and the cyclotron frequency $\tilde{\nu}_\mathrm{c}$ is measured from the quadrupolar spectra. The difference between these frequencies yields, $\tilde{\nu}_- = \tilde{\nu}_\mathrm{c} - \tilde{\nu}_+$.

Since the cyclotron frequency $\tilde{\nu}_\mathrm{c}$ can directly be measured from the quadrupolar de-

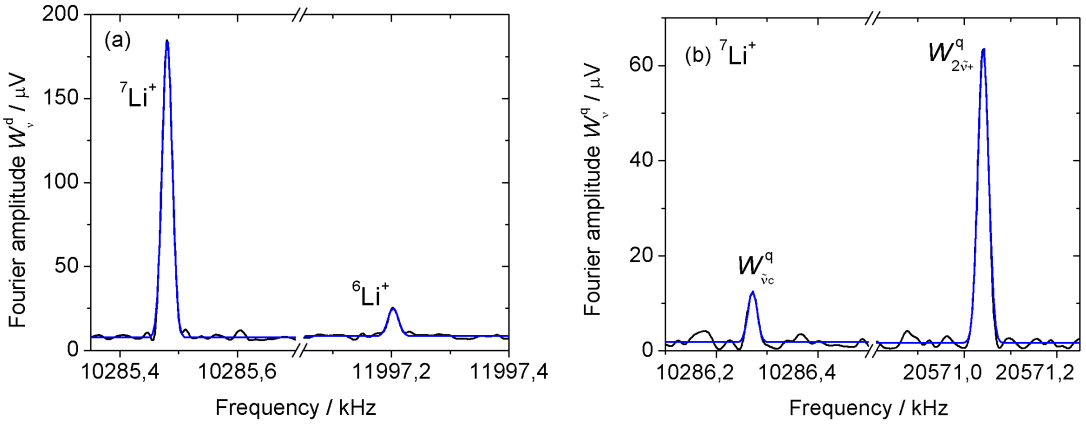

Figure 5.3: The Fourier amplitude $W_\nu^{d,q}$ is plotted as a function of the frequency. (a) The dipolar frequency spectrum shows signals at $\tilde{\nu}_+$ for both $^7Li^+$ and $^6Li^+$ ions. (b) The quadrupolar frequency spectrum is shown for the Fourier amplitudes $W^q_{\tilde{\nu}_c}$ and $W^q_{2\tilde{\nu}_+}$ for $^7Li^+$ ions. The blue line are Gaussian fits to the peaks in both panels.

tection method, the mass of the ion of interest can be determined. Note that in general the dipolar amplitude is larger than the quadrupolar amplitude. Especially for low abundant ion species the induced charges can be so low that no quadrupolar signal but a dipolar signal could be observed. In such cases a different method for mass determination has to be used. Various methods are presented in Section 5.6.

5.1.4 Frequency dependency on the trapping potential

The eigenfrequencies $\tilde{\nu}_+$ and $\tilde{\nu}_-$ depend on the applied trapping potential V_0. The magnetron frequency $\tilde{\nu}_-$ is in first order proportional to the trapping potential V_0 (see Eq. (2.17)). Thus, the measured modified cyclotron frequency $\tilde{\nu}_+$ decreases when V_0 increases:

$$\tilde{\nu}_+ = \tilde{\nu}_c - \tilde{\nu}_- = \tilde{\nu}_c - \frac{1}{2\pi}\left(\frac{V_0 C_2}{2d^2 B} + \Delta\tilde{\nu}_-\right) \tag{5.1}$$

where $\Delta\tilde{\nu}_-$ includes systematic frequency shifts. The measurement has been performed only with the four-fold segmented Penning trap. The eight-fold segmented Penning trap was not yet built at that time. Two opposing segments were used for creating a dipolar excitation field and the two other segments for ion detection. The ions were first excited at $\tilde{\nu}_-$ for 5 ms and afterwards at $\tilde{\nu}_+$ for 17 ms. A discrete-time signal with a duration of 80 ms was recorded for computing the frequency spectra. For the detection, the conventional dipolar detection as well as the single-phase quadrupolar detection methods were used. The latter one is referred as the sum signal from opposite detection segments of the four-fold ring electrode.

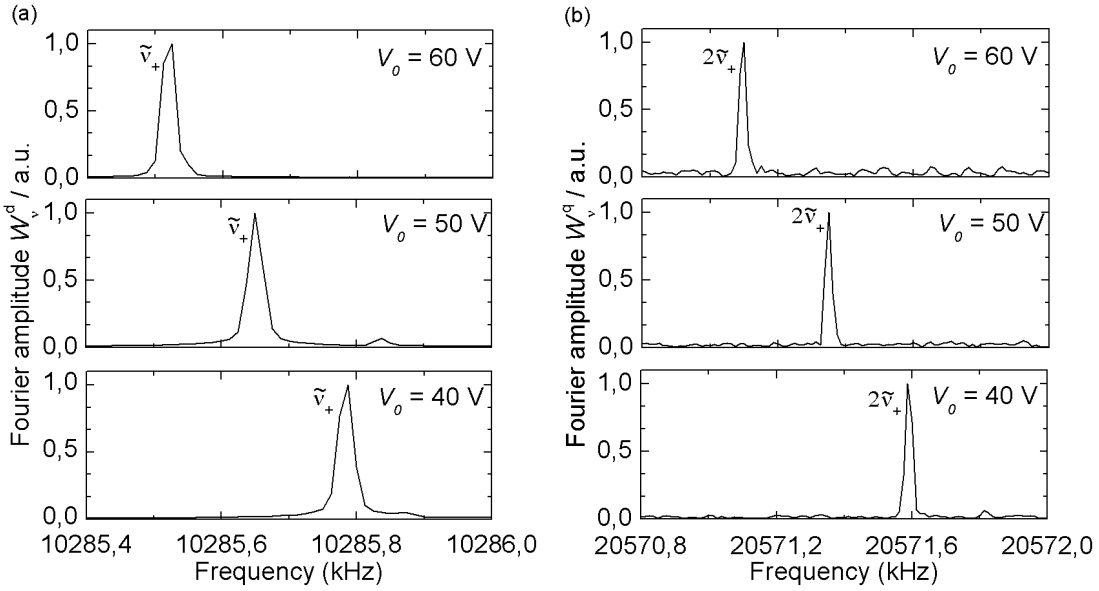

Figure 5.4: FT-ICR frequency spectra for $^7Li^+$ at the modified cyclotron frequency $\tilde{\nu}_+$ in (a), and at the second harmonic $2\tilde{\nu}_+$ in (b). The Fourier signals shift to higher frequencies as the trapping voltage V_0 decreases. The measurements are shown for the trapping voltages $V_0 = 40\,\mathrm{V}$, $50\,\mathrm{V}$ and $60\,\mathrm{V}$. The results are from Ref. [67].

Figure 5.4 shows the FT-ICR frequency spectra for trapping potentials V_0 of 40 V, 50 V and 60 V. Panel (a) shows the Fourier amplitude $W^{\mathrm{d}}_{\tilde{\nu}_+}$ in dipolar detection and panel (b) shows the Fourier amplitude $W^{\mathrm{q}}_{2\tilde{\nu}_+}$ in single-phase quadrupolar detection. For both cases, the Fourier amplitudes shift to higher frequencies when V_0 decreases. The shift at the second harmonic $2\tilde{\nu}_+$, as expected, is twice as large as the one for the frequency $\tilde{\nu}_+$ using the same trapping potential. This effect is commonly used to distinguish between a noise signal and an ion signal.

Figure 5.5 shows the measured frequencies $\tilde{\nu}_+$, $\tilde{\nu}_{\mathrm{c}}$, $(\tilde{\nu}_+ - \tilde{\nu}_-)$ and $2\tilde{\nu}_+$ as a function of the trapping potential. The sideband frequency $\tilde{\nu}_{\mathrm{c}}$, measured with the quadrupolar method, is almost independent on the trapping potential. Systematic dependencies due to trap imperfections lead to amplitude dependent frequency shifts. For a vanishing trapping potential $V_0 \to 0$, $\tilde{\nu}_+$ reaches $\tilde{\nu}_{\mathrm{c}}$ as described by Eq. (5.1). The same behaviour is observed for the lower magnetron sideband frequency at $\tilde{\nu}_+ - \tilde{\nu}_-$. Similarly, the second harmonic at $2\tilde{\nu}_+$ approaches to $2\tilde{\nu}_{\mathrm{c}} = 2(\tilde{\nu}_+ + \tilde{\nu}_-)$ for $V_0 \to 0$. The black lines in Fig. 5.5 show the theoretical behaviour of the eigenfrequencies for an ideal trap. In this case the frequencies would intersect at the cyclotron frequency for a vanishing trapping potential. The measured frequencies show deviations from the theoretical lines due to systematic frequency shifts which are discussed in detail in Section 5.6.

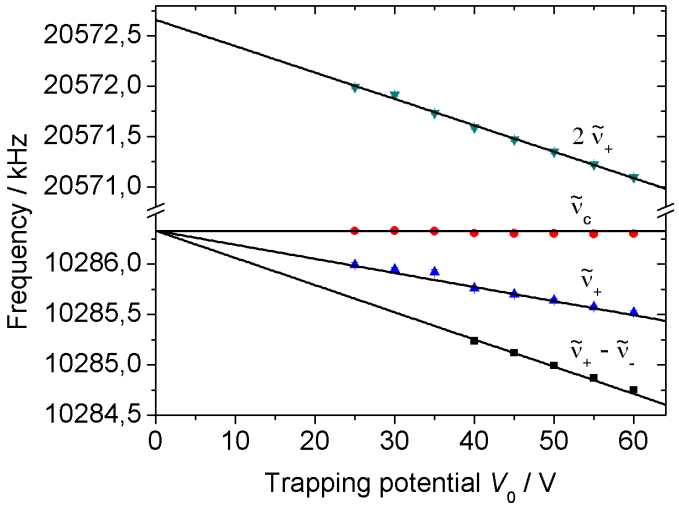

Figure 5.5: Measurement of the modified cyclotron frequency $\tilde{\nu}_+$, the magnetron sideband frequencies $(\tilde{\nu}_+ \pm \tilde{\nu}_-)$ and the second harmonic $2\tilde{\nu}_+$ of $^7Li^+$ ions as a function of the trapping potential V_0. The Fourier amplitudes were detected with the dipolar and the single-phase quadrupolar method [67]. The error bars are about 1.5 ppm and not visible in the plot. The lines show the theoretical behaviour of the various frequencies.

5.2 Sideband coupling with azimuthal quadrupolar excitation fields

The determination of the cyclotron frequency $\nu_c = qB/(2\pi m)$ is the key for mass determination of ions in a Penning trap. The ideal way to determine ν_c is to use the invariance theorem [8], when all three eigenfrequencies can be measured. The eigenfrequencies $\nu_+(\theta,\varepsilon)$, $\nu_-(\theta,\varepsilon)$ and $\nu_z(\theta,\varepsilon)$ are derived for an ion moving in a misaligned magnetic field and a harmonic distorted trapping potential, as explained in Section 2.1.2. However, when the nuclei are short-lived and created with a low production rate, the cyclotron frequency is determined in a direct way, which is well-known as the sideband frequency determination. The true cyclotron frequency ν_c differs by a systematic frequency shift $\Delta\tilde{\nu}_c$ from the measured frequency, i.e. $\tilde{\nu}_c = \nu_c + \Delta\tilde{\nu}_c$ [26]. In sideband mass spectrometry, the ion detection is either done with the TOF-ICR detection technique [68] or with the FT-ICR detection technique [14]. The latter one is reported in this thesis.

The sideband frequency can be determined from a frequency scan using an azimuthal quadrupolar electric field. The application of such a quadrupolar electric field at $\tilde{\nu}_c$ leads to an interconversion between the radial motional modes. The one- and two-pulse quadrupolar fields have been probed using $^7Li^+$ ions. The two-pulse excitation scheme is commonly known as the Ramsey excitation scheme. The FT-ICR signal was investigated by

varying the parameters of the quadrupolar rf field. These parameters are the excitation frequency ν_{exc}, i.e. the detuning $\delta = 2\pi(\nu_{\mathrm{exc}} - \tilde{\nu}_{\mathrm{c}})$, the excitation time τ_1 and the excitation amplitude. The dipolar signal allows to observe the cyclotron radius expressed by $R_+(\tau_1, \delta, g)$ (see Eq. (2.52)), which depends on the parameters of the quadrupolar rf field. The following results can also be found in [17].

5.2.1 General remarks and technical details

For the studies reported here, a Penning trap with an eight-fold segmented ring electrode was used. The setup was baked out so that a final pressure of $< 5.0 \times 10^{-9}$ mbar was achieved, which leads to a coherence time of the moving ion cloud of 160 ms. The timing scheme of the measurement cycle is shown in Fig. 4.1. After the ion injection, a dipolar excitation field at $\tilde{\nu}_-$ was applied. The magnetron excitation established an initial magnetron radius defined as $R_-(0)$. With a trapping potential V_0 of 55 V, the magnetron frequency $\tilde{\nu}_-$ is 664 Hz, using the method described in Fig. 5.2. In the next step, either a one- or a two-pulse quadrupolar excitation field was applied, which leads to an interconversion of the modes. The two-pulse scheme was generated by using an external rf-switch connected to a function generator. The excitation frequency ν_{exc} was scanned $\pm$500 Hz around the cyclotron frequency $\tilde{\nu}_{\mathrm{c}}$ using a step size of 5 Hz. At each frequency step the amplified ion signals induced on the four detection segments were recorded for 100 ms with a sampling rate of 42 MHz. After this, the dipolar FT-ICR Fourier amplitude $W^{\mathrm{d}}_{\tilde{\nu}_+}$ was measured from the frequency spectra. Finally, the ions were ejected from the trap and the next measurement cycle started again with the ion injection.

In this section, the resonance scans show the square of the dipolar Fourier amplitude $(W^{\mathrm{d}}_{\tilde{\nu}_+})^2$ as a function of the excitation frequency. The $(W^{\mathrm{d}}_{\tilde{\nu}_+})^2$ defines the signal intensity which is proportional to the square of the cyclotron radius R_+^2 and thus the kinetic energy in cyclotron mode could be determined. The stability of the dipolar Fourier amplitude has been determined from a long term measurement. The resulting standard deviation of the mean value is about 5% due to fluctuations of the ion current emitted from the ion source. For the signal intensities plotted in the resonance curves, the error bars were calculated using this statistical error.

The measured resonance scans are fit with the theoretical functions of the one- and two-pulse conversion profile (see Section 2.2.2). Here, the Levenberg-Marquardt χ^2 minimization method is used, which is a standard technique for a least square curve-fitting [69]. For the comparison of the theory with the data, the so-called R-squared value is used [70]. This value gives information about the minimization of the sum of squares of residuals. The coefficient of determination R-squared can be a number between 0 and 1. An R-squared

value close to one indicates that the regression fits well to the data, while an R-squared value near 0 indicates that the regression does not fit to the data.

For the interpretation of the results it is assumed that the trapped ions are guided centered into the trap, so that only a negligible initial magnetron motion occurs. This is verified by the application of a dipolar excitation field. If no quadrupolar signal at $\tilde{\nu}_c$ is detectable the initial magnetron motion is negligible. It is assumed that the ions are injected at the same position in the trap for each measurement cycle. The ions have some axial motion due to the in-flight capturing process but no effect on the Fourier amplitude could be observed. The origin of these initial motions is explained in detail in Section 5.6.1.

5.2.2 One-pulse excitation: variation of the excitation amplitude

When applying a quadrupolar rf field, the coupling strength g determines the strength of the interaction of the field with the ions. The coupling strength g depends on the trap geometry and is proportional to the applied excitation amplitude. The interconversion frequency, the so-called Rabi frequency depends on this coupling strength. Figure 5.6 shows the conversion time τ_c as a function of the rf excitation amplitude at a constant excitation time $\tau_1 = 9.2\,\mathrm{ms}$. It is observed that τ_c is smaller when the excitation amplitude is stronger. The data are fit with the conversion time function, given by $\tau_c = \pi/(2g)$ which depends inversely on the excitation amplitude.

Figure 5.7 shows the FT-ICR signal intensity $(W^{\mathrm{d}}_{\tilde{\nu}_+})^2$ as a function of the detuning $\delta = 2\pi(\nu_{\mathrm{exc}} - \nu_c)$ for a constant excitation time $\tau_1 = 9.2\,\mathrm{ms}$. Three different rf amplitudes, namely $U_{\mathrm{exc,PP}} = 1.7\,\mathrm{V}$ in (a), $3.4\,\mathrm{V}$ in (b) and $5.0\,\mathrm{V}$ in (c) were applied. In general, the rf amplitude can be chosen such that the excitation time is equal to $(2n+1)\tau_c$ with n an integer. In this case and at $\nu_{\mathrm{exc}} = \tilde{\nu}_c$, the initial magnetron motion is fully converted into the cyclotron motion, i.e. $R_+^2(\tau_c) = R_-^2(0)$ in (a) and $R_+^2(3\tau_c) = R_-^2(0)$ in (c). This leads to a maximum cyclotron radius, i.e. a maximum signal intensity as seen in panels (a) and (c).

When a detuning is applied, the interconversion is not complete, thus the ion motion is a superposition of a magnetron and cyclotron motion, i.e. $R_+^2(\tau_1) + R_-^2(\tau_1) = R_-^2(0)$. In consequence the Fourier amplitude decreases.

The comparison of the resonance scans in the panels (a) and (c) show that the line-width increases with larger rf amplitudes. This is due to a larger coupling strength g of the quadrupolar rf-field to the ions which decreases the conversion time. This effect can be explained by considering the phase $\phi = \omega_R \tau_1/2$ of the one-pulse profile function F_1, as seen in Eq. (2.54). The phase depends non-linearly on the detuning $\delta = 2\pi(\nu_{\mathrm{exc}} - \nu_c)$,

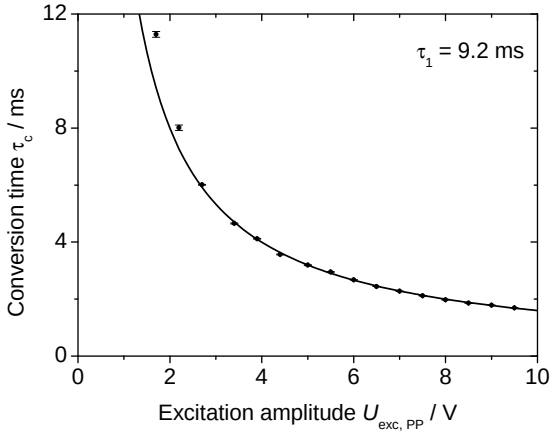

Figure 5.6: Conversion time τ_c as a function of the rf excitation amplitude $U_{\mathrm{exc,PP}}$. The solid line is a fit of the conversion time function to the data, given by $\tau_c = \pi/(2g) \propto U_{\mathrm{exc,PP}}$. The coupling strength g is directly proportional to the excitation amplitude.

which is due to the relation $\omega_R = \sqrt{4g^2 + \delta^2}$. The derivative of the phase with respect to the detuning, $d\phi/d\delta = \tau_1 \delta/\omega_R$, describes the variation of the phase with the detuning. For a large coupling strength g, the variation of the phase ϕ near $\nu_{\mathrm{exc}} = \tilde{\nu}_c$ is smooth. This leads to a broadening of the line-width of the central peak. For a lower g, the variation of the phase with the detuning is large, so that the line-width is reduced. In the special case when the detuning is much larger than the coupling strength, the slope of the derivative depends mainly on the excitation time τ_1. The profile function is then approximately the Fourier transform of a scalar wave train since the sinusoidal oscillations are independent of g.

Figure 5.7 (b) shows a resonance scan for an rf amplitude of 3.4 V. This amplitude corresponds to a conversion time of 4.6 ms which is twice the excitation time τ_1. The Fourier signal vanishes exactly on resonance because the cyclotron motion is converted back to the initial magnetron motion, i.e. $R_+^2(2\tau_c) = 0$ in (b).

The theoretical profile function given in Eq. (2.54) is fit to the data. From the fits result the parameters like the coupling constant g, the center-frequency $\tilde{\nu}_c$ and the amplitude. The R-squared value is between 0.93 to 0.96 for all fits. Thus we can conclude that the experimental data and the theoretical predictions agree very well.

Figure 5.7 (d) shows the measured signal intensity and Fig. 5.7 (e) is the expected function F_1 in color-coded contour plots as a function of the detuning and rf amplitude. Since the coupling strength scales linearly with the rf amplitude, the theoretical function is shown in units of the coupling strength. The color represents in both cases the degree of conversion. In Fig. 5.7 (d) three successive conversions from the magnetron motion to

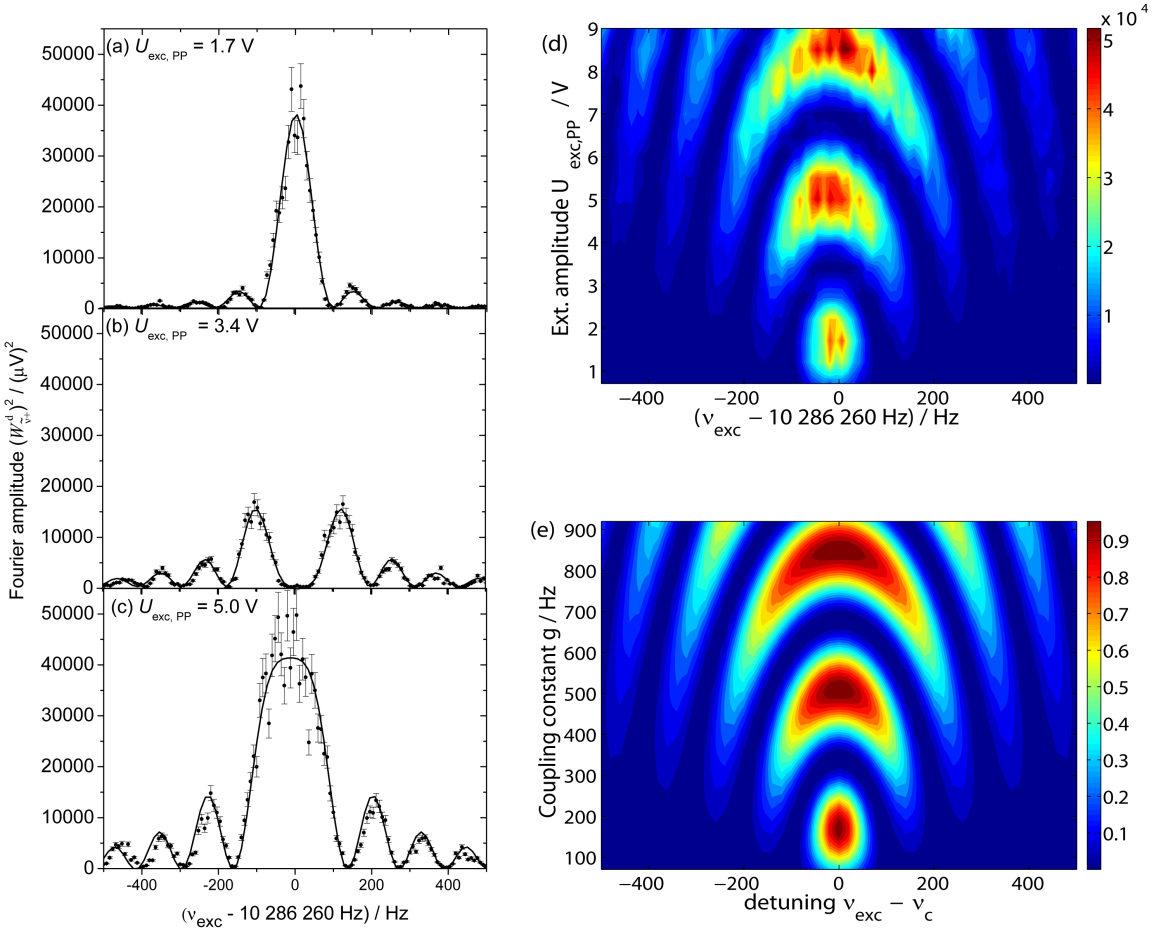

Figure 5.7: Resonance scans for a one-pulse quadrupolar excitation field measured for several excitation amplitudes: The FT-ICR signal intensity $(W^{\mathrm{d}}_{\tilde{\nu}_+})^2$ for a constant pulse duration $\tau_1 = 9.2\,\mathrm{ms}$ as a function of the detuning $\nu_{\mathrm{exc}} - \nu_c$ is shown for three different rf excitation amplitudes $U_{\mathrm{exc,PP}} = 1.7\,\mathrm{V}$ in (a), 3.4 V in (b), and 5.0 V in (c). The solid lines are fits of the theoretical one-pulse profile function F_1 (see Eq. (2.54)). (d) Square of the experimental FT-ICR amplitude as a function of the excitation amplitude $U_{\mathrm{exc,PP}}$ and the detuning δ. (e) Contour plot of the theoretical profile function for one-pulse quadrupolar excitation as a function of the coupling strength g and the detuning δ.

the cyclotron motion are observed. The line-width broadening for larger rf amplitudes appears due to the stronger coupling of the quadrupolar rf-field to the ions. Nice agreement between the data and the theory can be observed.

5.2.3 One-pulse excitation: variation of the excitation time

In this section, results with a one-pulse quadrupolar excitation field applied for several excitation times τ_1 are presented. A constant rf excitation amplitude of 5.0 V was used. Figure 5.8 shows the measured resonance scans for excitation times of $\tau_1 = 3.20$ ms in (a), 6.13 ms in (b) and 9.24 ms in (c), which correspond to roughly one, two and three times the conversion time τ_c of 3.18(3) ms. Theoretical fits are given by the black lines. For $\delta = 0$ Hz and a pulse duration of τ_c (panel (a)) a maximum signal intensity was measured. This is interpreted as a conversion of the initial magnetron motion into a pure cyclotron motion. After a pulse duration of $2\,\tau_c$, which is equal to the Rabi period τ_R a minimum signal was measured at $\delta = 0$ Hz, i.e. a back conversion from the cyclotron to the magnetron motion at the measured cyclotron frequency was observed. At $\tau_1 = 3\tau_c$, the measured cyclotron radius is again maximized.
The intensity of the fringes increases with the excitation time and the line-width of the central peak decreases, which is expected if we consider the zeros of the theoretical profile function F_1: For an excitation time $\tau_1 = (2n+1)\tau_c$, where n is an integer, a full conversion to only cyclotron motion occurs. In this case, the position of the zeros of the F_1-function next to the central peak are given by $\delta_0/(2\pi) = \pm\sqrt{4n+3}/((2n+1)2\tau_c)$. This equation implies that in terms of frequencies the detuning δ_0 at the position of the first zero obeys to a sort of time-energy uncertainty relation: $\hbar\delta_0 \cdot \tau_c(2n+1) = h\sqrt{4n+3}/2$. The line-width of the central peak decreases when the excitation time is longer and is equal to $(2n+1)\tau_c$. From the resonance scans in the panels (a) and (c) the first zero was measured to be 270 Hz and 140 Hz, respectively, which deviates from the theoretical values 272 Hz and 138 Hz due to the excitation time, which is not exactly one and three times τ_c.

Figure 5.8 (d) and (e) show the signal intensity $(W^{d}_{\tilde{\nu}_+})^2$ as a function of the detuning and the excitation time. During an excitation time of 18 ms, three full conversions occur at the resonance frequency $\nu_{exc} = \nu_c$. For a larger detuning more conversions are observed since the the Rabi frequency increases. However, for a non-zero detuning the ion motion is converted from a pure magnetron motion into a mixed motional mode.

5.2.4 Two-pulse excitation: variation of the excitation time

In this and the following subsections, the results from the measurements with the two-pulse Ramsey excitation scheme are presented. The two-pulse scheme uses two phase

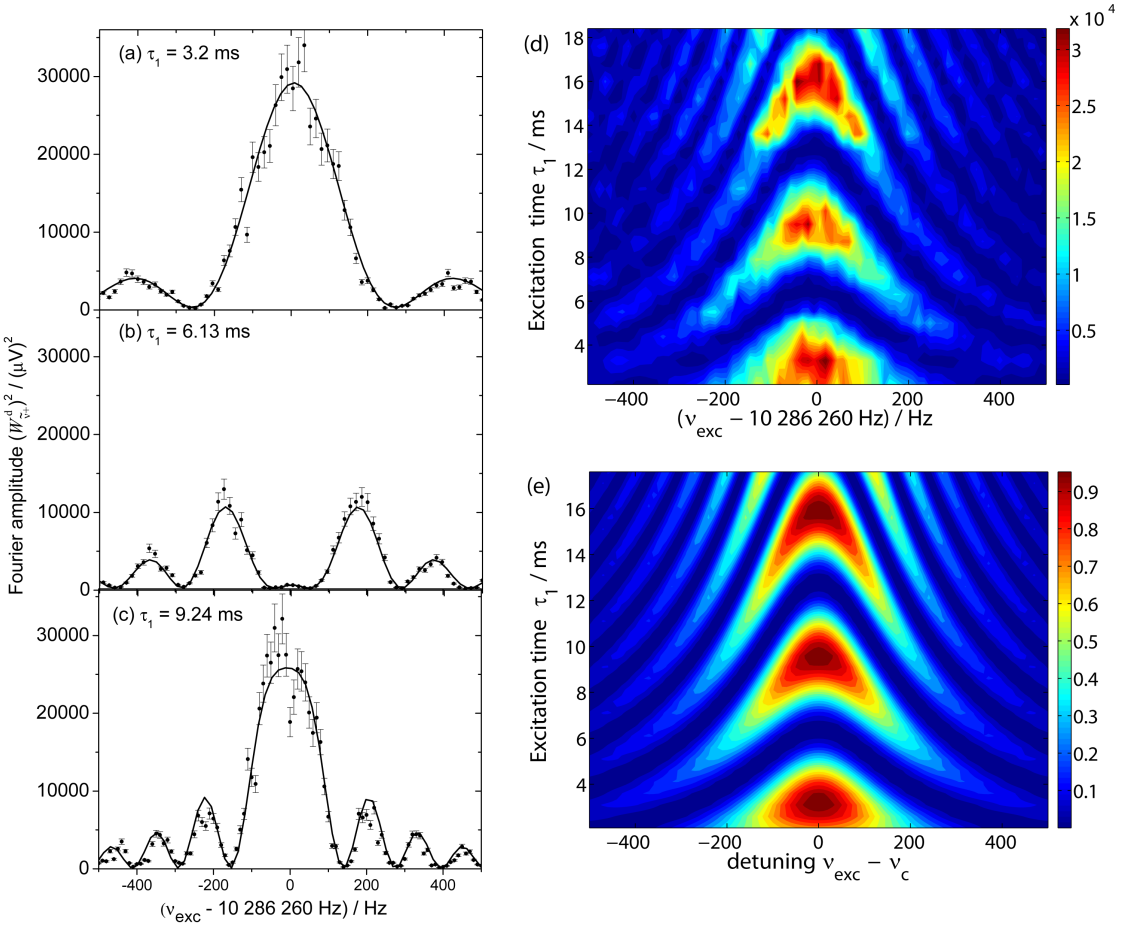

Figure 5.8: Resonance scans for a one-pulse quadrupolar excitation field measured for several excitation times: Experimental FT-ICR signal intensity $(W^{\mathrm{d}}_{\tilde{\nu}_+})^2$ for the pulse durations $\tau_1 = 3.2\,\mathrm{ms}$ in (a), 6.13 ms in (b), and 9.24 ms in (c) using a constant rf excitation amplitude $U_{\mathrm{exc,PP}} = 5.0\,\mathrm{V}$. The solid lines are fits of the theoretical one-pulse profile function F_1 (see Eq. (2.54)). (d) FT-ICR signal intensity as a function of the excitation time τ_1 and the detuning δ. (e) Contour plot of the theoretical profile for a one-pulse quadrupolar excitation as a function of τ_1 and δ.

coherent excitation pulses, which are separated by a waiting time τ_0. The interaction of the ions with the two-pulse quadrupolar field was studied for several excitation times τ_1 at a constant waiting time $\tau_0 = 7.5\,\text{ms}$ and a constant rf amplitude of 2.9 V. Figure 5.9 shows the signal intensity $(W^{\text{d}}_{\tilde{\nu}_+})^2$ for three different excitation times. The conversion time τ_c has been determined to be 7.5(2) ms and panels (a) and (c) show complete conversions from the magnetron mode into the cyclotron mode after the two resonant pulses with a duration of $2\tau_1 = \tau_c$ and $2\tau_1 = 3\tau_c$, respectively. In panel (b), a back conversion to the magnetron motion occurs after the resonant two-pulse excitation with a duration of $2\tau_1 = 2\tau_c$.

Figure 5.9 (d) and (e) serve as a comparison of the data and the two-pulse profile function depending on the excitation time and the detuning. A full conversion to a cyclotron motion occurs at an excitation time of 4 ms and 11 ms where the line-width $\Delta\nu$ of the central peak was determined to be 40 Hz and 64 Hz, respectively. Thus the line-width increases when increasing the excitation time from $2\tau_1 = \tau_c$ to $2\tau_1 = 3\tau_c$. The narrow line-width reappears periodically at excitation times $2\tau_1 = (4n+1)\tau_c$, with $n = 0, 1, 2, 3...$, while the broaden line-width reappears periodically at excitation times $2\tau_1 = (4n+3)\tau_c$. This process happens periodically with the Rabi period $\tau_R = 2\tau_c = 4\tau_1$ which is here 15 ms. This is an interesting result since a longer excitation time doesn't result necessary in a narrower line-width for a two-pulse quadrupolar excitation field.

5.2.5 Two-pulse excitation: variation of the waiting time

In this section, the two-pulse Ramsey excitation scheme is investigated by varying the waiting time. Figure 5.10 shows the FT-ICR signal intensity $(W^{\text{d}}_{\tilde{\nu}_+})^2$ for a constant excitation time $\tau_1 = 3.4\,\text{ms}$ and for three different waiting times $\tau_0 = 6.8\,\text{ms}$ in (a), 17.0 ms in (b), and 23.8 ms in (c). The excitation time τ_1 was set to be the half of the conversion time. For a resonant excitation at $\tilde{\nu}_c$, a full conversion to the cyclotron motion occurs. The envelopes are identical for all waiting times. It is described by the first $\sin^2(\omega_R\tau_1/2)$-term, which appears as, as seen in Eq. (2.56). As discussed in Section 2.2.2, the number of sidebands increases due to the longer total time τ_{tot}. Analytically, it can be described by rewriting the two-pulse profile function (Eq. (2.56)):

$$F_2(\delta, \tau_0, \tau_1, g) = \frac{16\,g^2}{\omega_R^2} \sin^2\left(\frac{\omega_R\tau_1}{2}\right) \cos^2\left(\frac{\omega_R\tau_1}{2}\right) \times \cos^2\left(\frac{\delta\tau_0}{2}\right) \left[1 - \frac{\delta}{\omega_R} \tan\left(\frac{\delta\tau_0}{2}\right) \tan\left(\frac{\omega_R\tau_1}{2}\right)\right]^2. \tag{5.2}$$

The oscillations with respect to the detuning are defined by the $\cos^2\left(\frac{\delta\tau_0}{2}\right)$-term for a constant waiting time. The distance between the zeros is given by $\Delta\delta \cdot \tau_0/2 = \pi$, i.e.

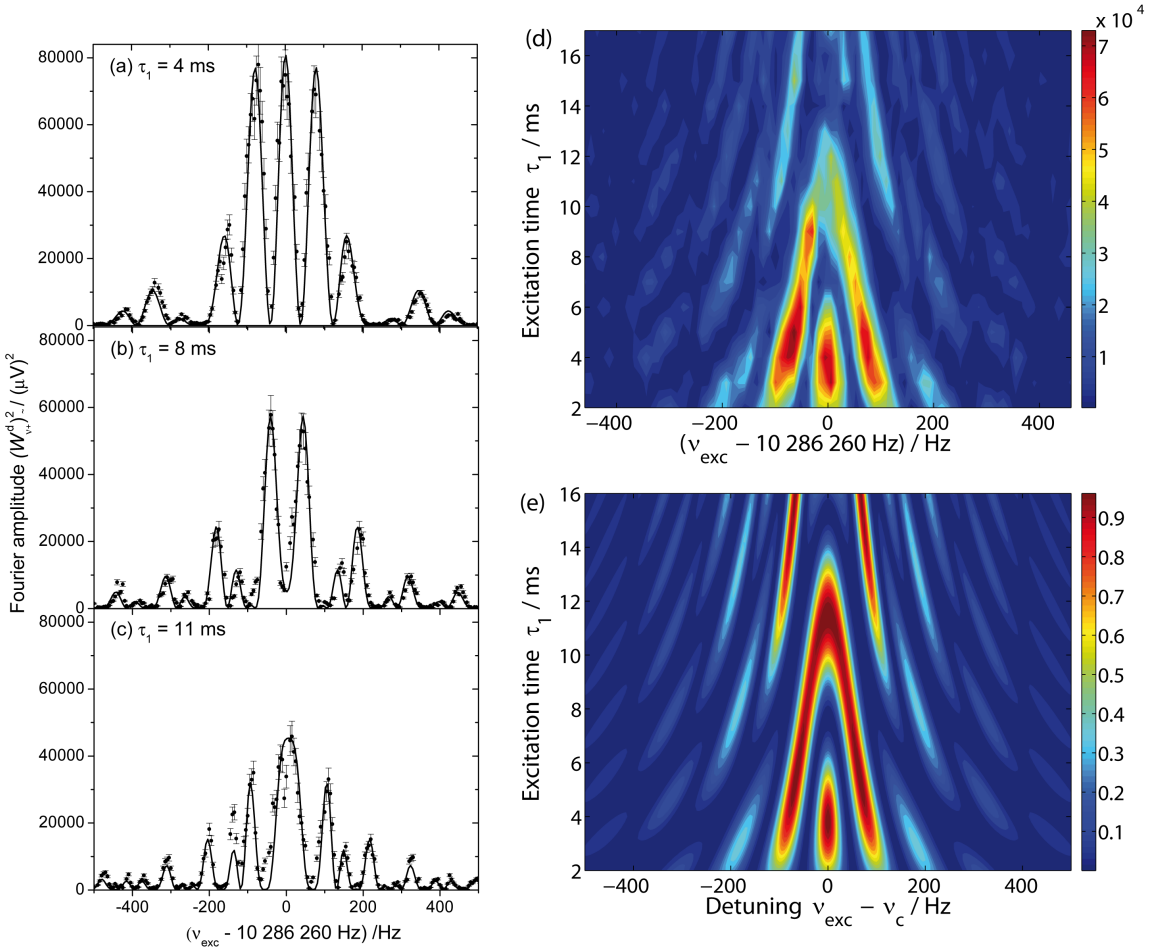

Figure 5.9: Resonance scans for a two-pulse Ramsey excitation field measured for various excitation times: Experimental FT-ICR signal intensity $(W^{\mathrm{d}}_{\tilde{\nu}_+})^2$ for three excitation times $\tau_1 = 4\,\mathrm{ms}$ in (a), 8 ms in (b), and 11 ms in (c) with a constant waiting time $\tau_0 = 7.5\,\mathrm{ms}$. The rf amplitude is $U_{\mathrm{exc,PP}} = 2.9\,\mathrm{V}$. The solid lines are fits of the theoretical two-pulse profile function F_2 (see Eq. (2.56)). (d) FT-ICR signal intensity as a function of the excitation time τ_1 and the detuning δ. (e) Theoretical contour profile for a two-pulse Ramsey excitation as a function of τ_1 and δ.

$\Delta\nu = 1/\tau_0$. Thus, a longer waiting time increases drastically the resolving power due to a longer total time $\tau_{\mathrm{tot}} = 2\tau_1 + \tau_0$.
Theoretically the waiting time and the coupling strength can be chosen such that a detuning interval exists where the magnetron motion can be converted to a pure cyclotron motion. This effect occurs if the condition $(\delta/2g)^2 \leq 1$ is satisfied [32]. For the measurements presented here, a constant rf amplitude of $U_{\mathrm{exc,PP}} = 2.9\,\mathrm{V}$ was used. The coupling strength g of 198 Hz could be extracted from the fits to the data. In our case this condition is written as $|(\nu_{\mathrm{exc}} - \nu_{\mathrm{c}})| \leq 63\,\mathrm{Hz}$. From the resonance scan shown in Fig. 5.10 (c), the first sideband is measured at a detuning of $\delta/(2\pi) \approx \pm 36\,\mathrm{Hz}$ beside the center peak. At this off-resonant frequency the ion motion is converted from a pure magnetron motion into a pure cyclotron motion.

After the first rf excitation pulse at the sideband frequency with a duration of τ_{c} the ion motion is a superposition of a magnetron and a cyclotron motion and the radii of both motions are equal. During the waiting time τ_0 the phase of the motional modes of the ions evolves in time. If a second excitation pulse is applied exactly at the sideband frequency, no phase shift between the oscillating field and the ion motion occurs. The interaction of the ions with the field leads to a full conversion to a pure cyclotron motion. For an off-resonant excitation, $\nu_{\mathrm{exc}} \neq \tilde{\nu}_{\mathrm{c}}$ with a duration of τ_{c}, the conversion is incomplete and the magnetron radius is larger than the cyclotron radius. When the phase between the rotating field and the ion motion is changed to π then a back conversion to the magnetron motion occurs. This leads to an oscillating behaviour between the magnetron and cyclotron motion with the detuning. In the case when the phase is between 0 and π, the ion motion is a superposition of a magnetron motion and a cyclotron motion. A longer waiting time leads to a faster oscillation with the detuning as seen from Eq. (5.2).

The R-squared value for the fits of the theoretical profile function is determined to be between 0.94 and 0.96. Again a nice agreement between the theoretical predictions and the experimental data is observed. From the fits to the resonance scans the sideband frequency is determined with a certain statistical uncertainty. It is observed that the statistical uncertainty decreases from 0.6 Hz to 0.1 Hz when increasing the waiting time from $\tau_0 = 1.7\,\mathrm{ms}$ to $\tau_0 = 23.8\,\mathrm{ms}$, respectively. The decrease of the statistical uncertainty was also observed by studies presented by S. George et al. in Ref. [35].

Figure 5.10 (d) shows $(W^{\mathrm{d}}_{\tilde{\nu}_+})^2$ as a function of the detuning δ for different waiting times τ_0. The intensity of the central peak and the n-th order sideband decreases strongly with the waiting time. As mentioned in Section 5.2.1, this is due to collisions of the ion cloud with rest gas particles, which limits the coherence time. The collisions damp the cyclotron radius and lead to a randomization of the phase of the cyclotron motion. Additional mechanisms like ion-ion interactions as well as trap anharmonicity lead to

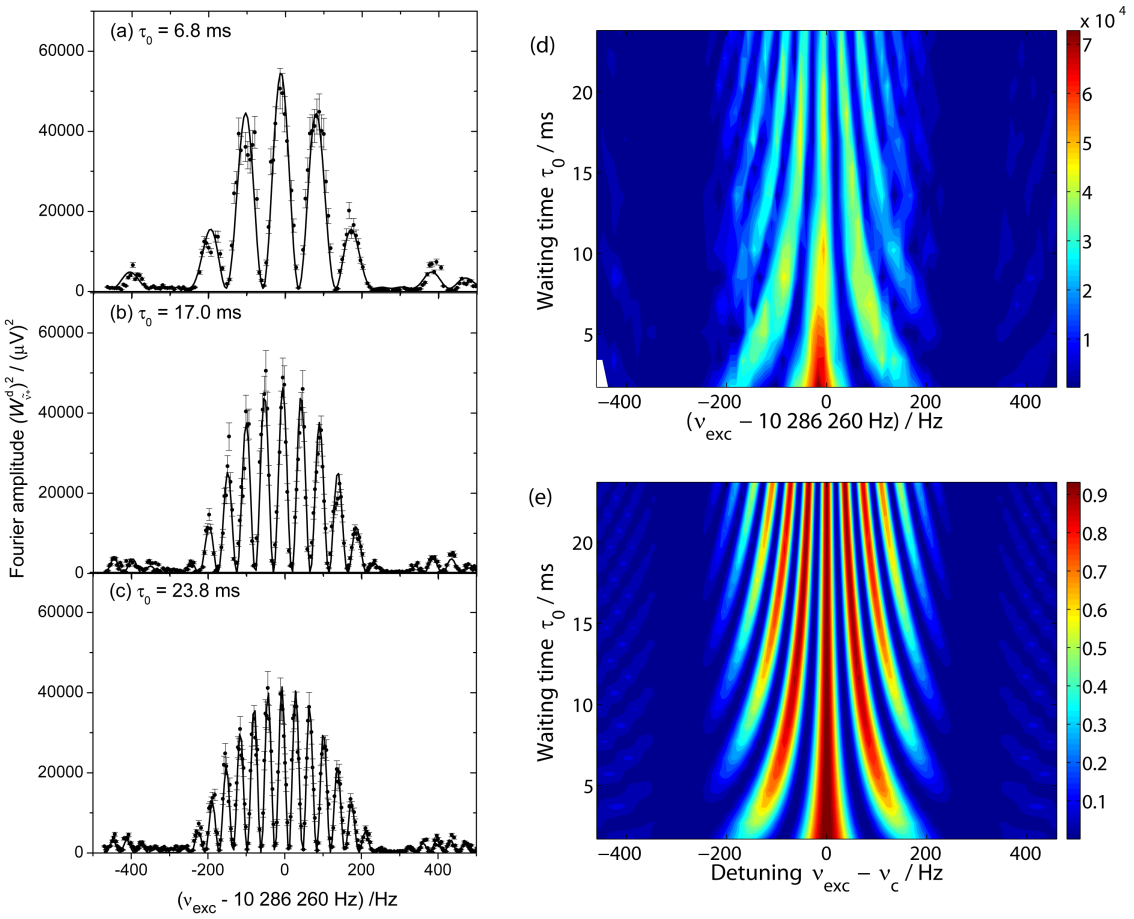

Figure 5.10: Resonance scans for a two-pulse Ramsey excitation field measured for several waiting times: Experimental FT-ICR signal intensity $(W^{\mathrm{d}}_{\tilde{\nu}_+})^2$ for the waiting times $\tau_0 = 6.8\,\mathrm{ms}$ in (a), $17.0\,\mathrm{ms}$ in (b), and $23.8\,\mathrm{ms}$ in (c) with a constant pulse duration $\tau_1 = 3.4\,\mathrm{ms}$ and constant rf amplitude $U_{\mathrm{exc,PP}} = 2.9\,\mathrm{V}$. The solid lines are fits of the theoretical two-pulse profile function F_2 (see Eq. (2.56)). (d) FT-ICR signal intensity as a function of the waiting time τ_0 and the detuning δ. (e) Theoretical contour profile for a two-pulse Ramsey excitation as a function of τ_0 and δ.

a further dephasing of the ion cloud and thus to a decrease of the Fourier signal at $\tilde{\nu}_+$ [71, 72].

5.2.6 Two-pulse excitation: constant total time

Lastly, two-pulse Ramsey measurements were performed with a constant total time $\tau_{\mathrm{tot}} = 2\tau_1 + \tau_0 = 15\,\mathrm{ms}$. Here the ratio τ_1/τ_0 of the pulse duration to the waiting time is changed for each measurement cycle. A constant rf amplitude of $U_{\mathrm{exc,PP}} = 2.9\,\mathrm{V}$ was used which is equivalent to a conversion time $\tau_c = 7.5(3)\,\mathrm{ms}$. Thus for an excitation time of $1\tau_c$ a full conversion to a cyclotron motion and a back conversion to the magnetron motion is observed. Figure 5.11 shows the FT-ICR signal intensity $(W^{\mathrm{d}}_{\tilde{\nu}_+})^2$ for the ratios of $\tau_1/\tau_0 =$ 0.30 in (a), 0.60 in (b), and 3.25 in (c). It is observed that a longer waiting time causes more sidebands. The envelope of all peaks, described by the phase $\omega_{\mathrm{R}}\tau_1$ increases when the excitation time is shorter. In addition, the line-width of the central peak decreases from (a) to (c). The larger the waiting time the more sidebands occur around the center peak, when comparing panel (a) and (c). This is again due to the fact that the phase $\phi = \delta\tau_0$ of the conversion probability F_2 oscillates much faster than the phase of the envelope. Panel (c) shows that the central peak vanishes if the excitation time τ_1 of 6.5 ms reaches the conversion time $\tau_c = 7.5\,\mathrm{ms}$. The R-squared value of the fits from the theoretical profile function F_2 given in Eq. (2.56) is between 0.93 and 0.97. As seen, the theory agrees very nicely with the data.

Panel (d) and (e) of Fig. 5.11 show the data and the theoretical two-pulse profile function as a function of the waiting time and the detuning. For a waiting time τ_0 from 5 to 7 ms and a detuning of $\pm 80\,\mathrm{Hz}$, it is observed that the first sideband is converted to a full cyclotron motion, as confirmed by the theory.

5.3 Space charge effects in a Penning trap

In FT-ICR MS, typically 10^3 up to 10^5 ions are stored, excited and detected simultaneously. When storing many particles in a Penning trap, deviations from the single ion description occur. The Coulomb interaction between the particles is not negligible. The stored ion cloud can form a plasma which can shield applied rf fields and modify the trapping potential. Additionally, Coulomb effects between two or more ion clouds lead to frequency shifts and a line broadening of the spectral Fourier amplitude.

In this section, a short introduction into nonneutral plasma is presented. The physical basics of a non-neutral plasma are described in detail in Refs. [73, 74]. Furthermore, experimental results concerning the shielding of dipolar and quadrupolar excitation fields

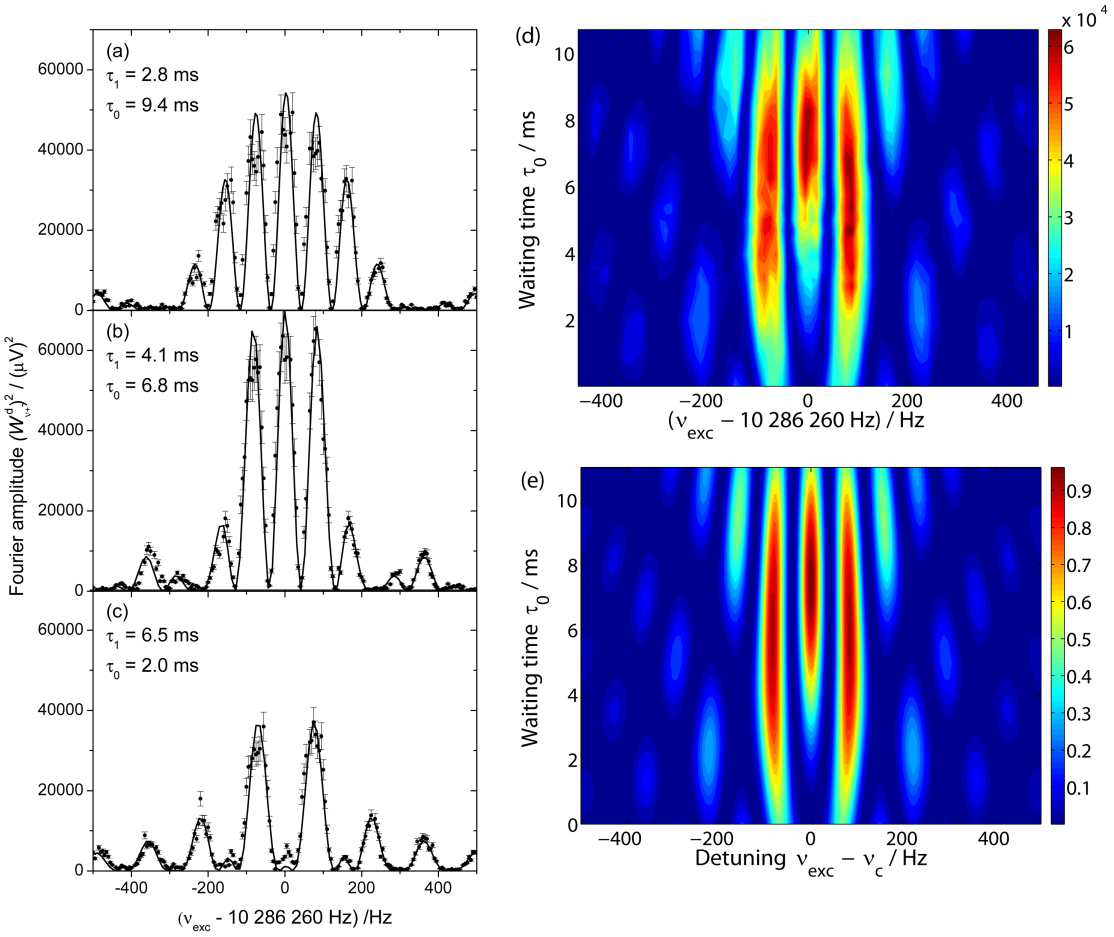

Figure 5.11: Resonance scans for a two-pulse Ramsey excitation field for a constant total time $\tau_{\mathrm{tot}} = 2\tau_1 + \tau_0 = 15\,\mathrm{ms}$: Experimental FT-ICR signal intensity $(W^{\mathrm{d}}_{\tilde{\nu}_+})^2$ for the ratios $\tau_1/\tau_0 = 0.30$ in (a), 0.60 in (b), and 3.25 in (c). A constant rf amplitude $U_{\mathrm{exc,PP}} = 2.9\,\mathrm{V}$ is applied. The solid lines are fits of the theoretical two-pulse profile function F_2 (see Eq. (2.56)). (d) FT-ICR signal intensity as a function of the waiting time τ_0 and the detuning δ. (e) Theoretical contour profile for a two-pulse Ramsey excitation as a function of τ_0 and δ.

by the charges stored in a Penning trap are presented and discussed.

5.3.1 The nonneutral plasma in a Penning trap: a short introduction

The plasma is defined as a collection of charged particles that show a collective behaviour [73]. One refers to a plasma when all dimensions of the ion cloud are large compared to the Debye length

$$\lambda_{\mathrm{D}} = \sqrt{\frac{k_{\mathrm{B}} T \varepsilon_0}{n q^2}}, \tag{5.3}$$

where T and n are the temperature and the density of the charges q, respectively. k_{B} is the Boltzmann constant and ε_0 is the vacuum permittivity. The charge density is nearly constant inside the plasma and drops to zero on the surface on the scale of the Debye length λ_{D}.
One important consequence of the collection of charges is that they create a space charge potential which can substantially modify an external electric field. This feature is known as Debye shielding (Debye and Hückel [75]). The charges in a plasma arrange their positions so that any applied electric field is Debye shielded out.
Let's consider a spheroidal plasma shape in a Penning trap. The charges create a radially outward electric field $\vec{E} \propto m/q\omega_{\mathrm{p}}^2 r$, which depends on the plasma frequency

$$\omega_{\mathrm{p}}^2 = \frac{n q^2}{\varepsilon_0 m}. \tag{5.4}$$

The ion cloud rotates as a rigid rotator about the direction of the magnetic field with the rotation frequency

$$2\omega_r(\omega_{\mathrm{c}} - \omega_r) = \omega_{\mathrm{p}}^2, \tag{5.5}$$

which depends on the cyclotron frequency and on the ion density. The rigid rotator has two possible rotating frequencies

$$\omega_{r,\pm} = \frac{1}{2}\left(\omega_{\mathrm{c}} \pm \sqrt{\omega_c^2 - 2\omega_{\mathrm{p}}^2}\right), \tag{5.6}$$

where the lower branch describes the rotation from the $\vec{E} \times \vec{B}$ drift about its own center and the upper branch describes the rotation of the cyclotron motion which is modified by the electric field created by the charges. Equation (5.6) is similar to Eq. (2.10) derived for the ion's eigenfrequencies in a trap. Here, the axial frequency is replaced by the plasma frequency. The upper branch has no apparent application in FT-ICR MS and is not considered in this thesis. The lower branch is important since the ions perform a slow circular

motion around the center of mass of the ion cloud. The shape of the ion cloud can be manipulated using a rotating wall excitation at the lower rotating frequency. A rotating wall excitation is a circular polarized dipolar field which is rotating in the same direction as the ion cloud. With a positive or negative detuning with respect to the rotating frequency, the ion cloud can be either compressed or expanded [76].
Equation (5.6) has to be real and sets the maximum density $n_{\max} = B^2\varepsilon_0/(2m)$ that can be confined in a Penning trap, which is called the Brillouin limit. In this limit, the rotating frequency of the rigid rotator is equal to the half of the cyclotron frequency [52]. For example, the Brillouin limit for $^7Li^+$ ions in a magnetic field of 4.7 T is 8.3×10^6 ions/mm^3 and the plasma frequency is $\omega_p = \omega_c/\sqrt{2}$. For a cloud with a temperature of 300 K at the Brillouin limit, the Debye length is about 13 µm.

5.3.2 Influence of space charges on the interaction of ions with a dipolar rf field

When many ions are stored in a Penning trap, the charges can create a plasma and shield the external excitation field. Here, the influence of space charges on the interaction of ions with a dipolar rf field has been investigated using a total number of about $4 \cdot 10^5$ trapped ions, with 93 % of $^7Li^+$ ions and 7 % of $^6Li^+$ ions.

The measurement cycle of an excitation amplitude scan: The measurements were performed with the trap having an eight-fold segmented ring electrode. The measurement cycle is similar to the timing scheme showed in Fig. 4.1. After the injection, a dipolar excitation field at $\tilde{\nu}_+$ of $^7Li^+$ was applied for 4.1 ms. Then, a dipolar excitation field at $\tilde{\nu}_+$ of $^6Li^+$ for 3.5 ms was used. The excitation amplitude of the $^7Li^+$ ions was scanned from 0.05 to 4 V with a step size of 0.05 V while the excitation amplitude the $^6Li^+$ ions was kept constant, once at 1.5 V and once at 2.5 V. The discrete-time signals were recorded for 100 ms and 20-times averaged, and the dipolar spectrum was computed. From this spectrum the center frequency $\tilde{\nu}_+$ and the Fourier amplitude were measured. Averaging the discrete-time signals n-times increases the SNR by $\sqrt{n}$. Finally the ions were ejected and the measurement cycle with a period of 400 ms starts again.
The amplitude scan was 20-times repeated. Thus a mean value and a statistical error could be calculated, which was used for the error propagation. The amplitude scans were done for four different trapping voltages V_0 from 25 V to 35 V in 5 V steps. Figure 5.12 shows the results as a function of the $^7Li^+$ excitation amplitude for two fixed $^6Li^+$ excitation amplitudes of 1.5 V (black data points) and 2.5 V (blue data points).

Results for a dipolar rf field: Figure 5.12 (a) shows the modified cyclotron frequency $\tilde{\nu}_+$ of $^7Li^+$ as a function of the excitation amplitude. The frequency decreases by 60 Hz over the whole excitation amplitude interval which is due to field imperfections, where the ion's eigenfrequency shifts with the cyclotron radius. Additionally, the line-width of the Fourier peak in the frequency spectra increases from 16 Hz to 26 Hz. The statistical error also increases with the excitation amplitude. This can be explained as follows. The ion cloud has a spatial extension in the radial direction. As a consequence of the field imperfections, an ion with a smaller R_+ has a larger frequency compared to an ion with a larger R_+. When the ion cloud evolves in time, a phase difference between these ions in the cloud occurs and increases over time. This phase difference leads to a spread of the ion cloud and thus the ions will not stay phase locked. More details are described in Section 5.6.1. Note that the frequency $\tilde{\nu}_+$ of $^7Li^+$ is not influenced by the excitation of the $^6Li^+$ ions.
Figure 5.12 (b) shows that the $^7Li^+$ Fourier amplitude $W^{\mathrm{d}}_{\tilde{\nu}_+}$ increases linearly with the excitation amplitude for an excitation amplitude interval from 0 V to 0.6 V and then saturates for an excitation amplitude of 1-2 V. Above this value, the Fourier amplitude decreases. The reason is that the ions don't stay phase locked, as explained above.

Figure 5.12 (c) shows the frequency $\tilde{\nu}_+$ of the $^6Li^+$ ions as a function of the $^7Li^+$ excitation amplitude. The measured frequency does not stay constant, as one expects for an excitation field with constant parameters. The frequency depends on the cyclotron radius of the $^7Li^+$ ions. For the $^6Li^+$ ions with an excitation amplitude of 1.5 V (black data points), the measured frequency $\tilde{\nu}_+$ jumps from 11 997 200 Hz to 11 997 280 Hz by 80 Hz at $U_{\mathrm{exc}} = 0.3$ V. Then the frequency stays constant up to $U_{\mathrm{exc}} = 1.9$ V and then changes by -80 Hz. In an excitation amplitude interval from 2.15 V to 4.0 V the frequency increases slowly by 30 Hz. A similar behaviour is observed when $^6Li^+$ ions are excited with an amplitude of 2.5 V (blue data points).
Figure 5.12 (d) shows the Fourier amplitude $W^{\mathrm{d}}_{\tilde{\nu}_+}$ of the $^6Li^+$ ions as a function of the $^7Li^+$ excitation amplitude. Without a pre-excitation of $^7Li^+$ no Fourier amplitude of $^6Li^+$ is observed. The Fourier amplitude increases abruptly at $U_{\mathrm{exc}} = 0.3$ V for the $^6Li^+$ excitation amplitude of 1.5 V. Then the Fourier amplitude fluctuates about a value of 50 µV and drops to a local minimum for a $^7Li^+$ excitation amplitude of 2.15 V. After that the amplitude increases and reaches a stable value of 65 µV. A similar trend is observed for the 2.5 V data curve.
One can see a correlation in the trend when comparing the $^6Li^+$ frequency $\tilde{\nu}_+$ and $W^{\mathrm{d}}_{\tilde{\nu}_+}$. For these effects the following explanation can be given. The ion cloud forms a plasma, which shields the rf excitation field. For a low cyclotron radius of $^7Li^+$ the rf field for exciting $^6Li^+$ is shielded by the plasma, thus a low cyclotron radius is measured. The

space charge potential additionally modifies the trapping potential [73] and in consequence changes the eigenfrequency for $^6Li^+$. When the $^7Li^+$ ions are excited to a larger radius, the $^6Li^+$ radius increases rapidly. In this case the two ion clouds are separated and the Debye shielding is absent. In consequence, the Fourier amplitude is maximized and the frequency stays constant, as seen by the measurements. When the cyclotron radii of both species are equal the space charges shield again the rf field. The frequency drops again and the Fourier amplitude shows a local minimum.

Figure 5.12 (e) shows the dependence of the modified cyclotron frequency of the $^6Li^+$ ions as a function of the $^7Li^+$ excitation amplitude for trapping potentials from 20 V to 35 V in 5 V steps. The frequency $\tilde{\nu}_+$ depends linearly on the trapping potential, as described by Eq. (5.1). For the trapping potential of 20 V the frequency jump is less pronounced than compared to higher potentials. For a trapping potential of 20 V, a frequency jump of 37 Hz at an excitation amplitude of $U_{\mathrm{exc}} = 0.3\,\mathrm{V}$ occurs. For a trapping potential of 35 V, a frequency shift of 45 Hz is measured at an excitation amplitude of $U_{\mathrm{exc}} = 0.55\,\mathrm{V}$. An explanation might be that due to the higher trapping potential, the ion cloud is stronger compressed. The resulting axial amplitude is lower and the ion density increases which leads to a shorter Debye length. In consequence, the created space charge potential increases and thus the shielding of the external field is stronger for a larger trapping potential. Thus a larger excitation amplitude is needed to separate the $^6Li^+$ and $^7Li^+$ ions. The increase of the frequency jump with the trapping potential results from the modification of this potential by the space charge potential.
The frequency drops down for all trapping potentials at an excitation amplitude $U_{\mathrm{exc}} = 2\,\mathrm{V}$. Here is assumed that the cyclotron radii of both ion species are equal.

5.3.3 Influence of space charges on the interconversion of modes

The interconversion of the radial modes by means of a quadrupolar excitation field is influenced by the Coulomb effects. In order to observe an interconversion of modes of the $^6Li^+$ ions, both ion species have to be spatially separated.

For this measurement, the higher abundant $^7Li^+$ ions were first excited with a dipolar excitation field at $\tilde{\nu}_+$ which allowed to separate the two species. Then, a quadrupolar rf field was applied for which the frequency was scanned around the cyclotron frequency $\tilde{\nu}_c$ of the lower abundant $^6Li^+$ species. Figure 5.13 shows four quadrupolar resonance scans of the $^6Li^+$ ions for different pre-excitation amplitudes of the $^7Li^+$ ions, i.e. for different $^7Li^+$ cyclotron radii. Without pre-excitation of $^7Li^+$, the quadrupolar excitation field was shielded and thus no quadrupolar conversion for $^6Li^+$ was observed. This case is not shown here. For an increased excitation amplitude, the shielding effect is lowered and a

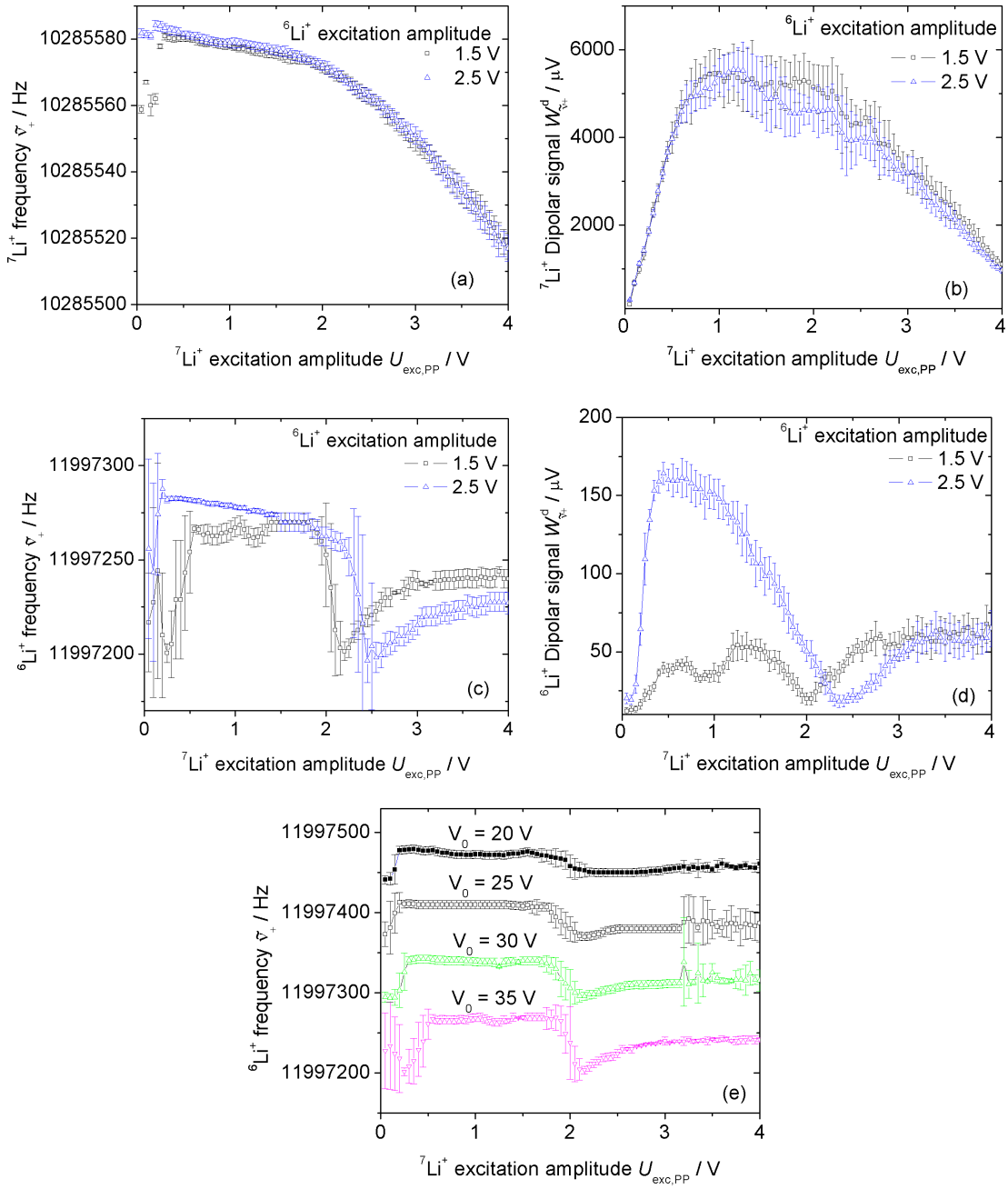

Figure 5.12: Shielding of a dipolar rf field presented for ^{6}Li$^+$ and ^{7}Li$^+$ ions as a function of the excitation amplitude for ^{7}Li$^+$ ions, respectively. The results are shown for excitation amplitudes of 1.5 V and 2.5 V for the ^{6}Li$^+$ ions. Panels (a) and (b) show the modified cyclotron frequency and the dipolar Fourier amplitude of the ^{7}Li$^+$ ions. Panels (c) and (d) show the modified cyclotron frequency and the dipolar Fourier amplitude of the ^{6}Li$^+$ ions. Panel (e) shows the measured frequency $\tilde{\nu}_+$ of ^{6}Li$^+$ for four trapping potentials V_0 as a function of the excitation amplitude. For the explanations see text.

resonance occurs.
Panels (a) and (b) of Fig. 5.13 show the resonance scan for an excitation amplitude of the $^7Li^+$ ions of 0.3 V of and 0.4 V. The central peak splits up in two peaks, with a larger amplitude for the one at higher frequency. Additionally, no sidebands on the high frequency side of the resonance are observed, while an asymmetric and broad sideband occurs at the low frequency side. In panel (c), the largest resolving power is reached for a pre-excitation amplitude of 0.75 V. For this case no sidebands are observed. In panel (d), the $^7Li^+$ ions are excited to a large cyclotron radius by using an amplitude of 40 V. The resonance scan shows sidebands resulting from the interconversion of motional modes. At this moment the two ion species are spatially separated and the influence of the space charge potential between both ion species is reduced. But notice that the amplitude of the center peak is too low. A possible explanation can be that the conversion from the magnetron to the cyclotron motion is incomplete. During the conversion process the ion can be driven to a maximum radius given by $(R_+ + R_-)/\sqrt{2}$, due to the superposition of the magnetron and cyclotron radii. At this maximum radius the space charge potential created by the $^7Li^+$ ions and field inhomogeneities can lead to an incomplete conversion.

The effects observed in the resonance scans, like peak-splitting, no sidebands and variation of the resolving power are not yet understood. A line-width broadening and a double peak structure without sidebands have also been observed experimentally at REXTRAP [77, 78], where buffer gas cooling was used. In simulation studies shown in Ref. [79] these effects were investigated using a particle number up to 10^5.

5.4 Coulomb effects: SIMBUCA simulations

The motion of Coulomb interacting particles in a Penning trap has been simulated using the open source program SIMBUCA from S. van Gorp [79]. This program evaluates the equation of motion for many Coulomb interacting particles in any kind of electromagnetic fields. The program includes Coulomb interactions, several excitation schemes and buffer gas cooling. The calculation of the Coulomb forces are performed on a graphic card using an optimized algorithm for *N*-body simulations [80].
As seen in Section 5.3, space charges can shield the rf field, leading to a peak broadening and to a suppression of the sidebands in the resonance scan. The simulations with SIMBUCA have been carried out in order to study the Debye shielding of the dipolar and the quadrupolar excitation fields.

Note that other programs for simulating Coulomb interacting particles have been developed where the particle-in-cell model [81] is used. More details about the results can be found in the references from D.E. Mitchell [71] and E.N. Nikolaev *et al.* [72]. These

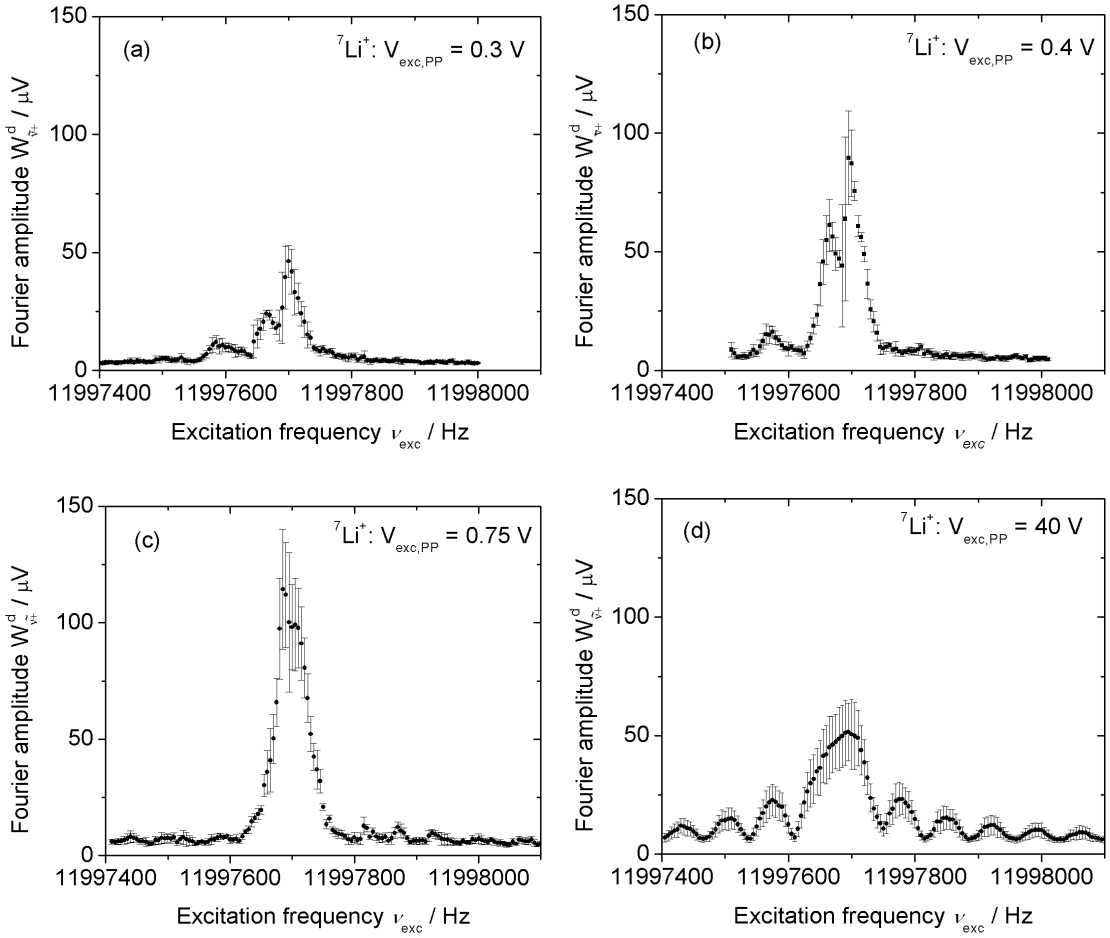

Figure 5.13: Quadrupolar conversion profile for $^6Li^+$ under the influence of the space charge of the $^7Li^+$ ions. The dipolar Fourier amplitude of $^6Li^+$ is shown as a function of the excitation frequency around $\tilde{\nu}_c$ for a one-pulse quadrupolar excitation scheme. The conversion profile was recorded for various excitation amplitudes of $^7Li^+$ of 0.3 V in (a), 0.4 V in (b), 0.75 V in (c) and 40 V (d).

programs include image charge interactions.

5.4.1 Debye shielding of a dipolar excitation field

As already mentioned in Section 5.3.1, the space charge potential created by the ions can shield the excitation field. To confirm this effect, an ion cloud with 4096 particles was simulated with a scale factor of 30, resulting in 122 880 particles [79, 66]. The ion cloud consists of 93% of $^7Li^+$ and 7% of $^6Li^+$ ions. The initial distribution of the ions is a Gaussian shape around the center of the Penning trap with a standard deviation of 0.25 mm in the x, y plane and 0.5 mm in the z direction. The electric and magnetic fields were assumed to be ideal, using an electrostatic coefficient C_2/d^2 of 783 m^{-2} and a trapping voltage of 60 V, according to the parameters from the Penning trap used in this setup. Instead of a magnetic field of 4.7 T a field of 1 T was used, which reduces the cyclotron frequency of the lithium ions. This decreases significantly the simulation time since larger time steps can be used for integrating the equation of motion with the fourth order Runge-Kutta integrator method [82]. The number of arithmetical operation is drastically decreased.

Figure 5.14 shows the simulation results of a dipolar excitation of $^6Li^+$ ions and $^7Li^+$ ions for four cases. The timing scheme of the excitations used for the simulations and their corresponding amplitudes is shown in the left column, the cyclotron radius R_+ as a function of time is shown in the second column. The red points represent the $^7Li^+$ ions and the black points represent the $^6Li^+$ ions. The distribution of the cyclotron radius after the excitations is shown in the third column and the ion position in the $x-y$-plane after the excitations is shown in the last column.

In panel (a) only a dipolar excitation at ν_+ for the $^6Li^+$ ions was applied. As seen, the space charges shield the rf field. The $^6Li^+$ ions stay near the trap center and satellite ions are formed which means a broader distribution of the cyclotron radius occurs. In panel (b), the $^7Li^+$ ions were excited to a cyclotron radius of 1 mm. The $^6Li^+$ ions were excited to a radius R_+ up to 30 mm, but satellite ions appear also at lower radii R_+. The ion distribution is spread over the cyclotron radius range from 24 mm to 32 mm. In both cases a fraction of the ions stay at the trap center. Due to the space charge of both lithium species, the ions created in the center of the Gaussian distribution are harder to excite than the ions created in the wings.

Figure 5.14 (c) is similar as case (b) but the $^7Li^+$ ions are excited to a larger cyclotron radius. As seen the ion species can be clearly separated. The clouds of both ion species show a phase coherent motion and form a condensed part [72]. Thus a narrow ion distribution around $R_+ = 32$ mm is observed.

In panel (d), both species were excited to the same cyclotron radii. As in the case of (c)

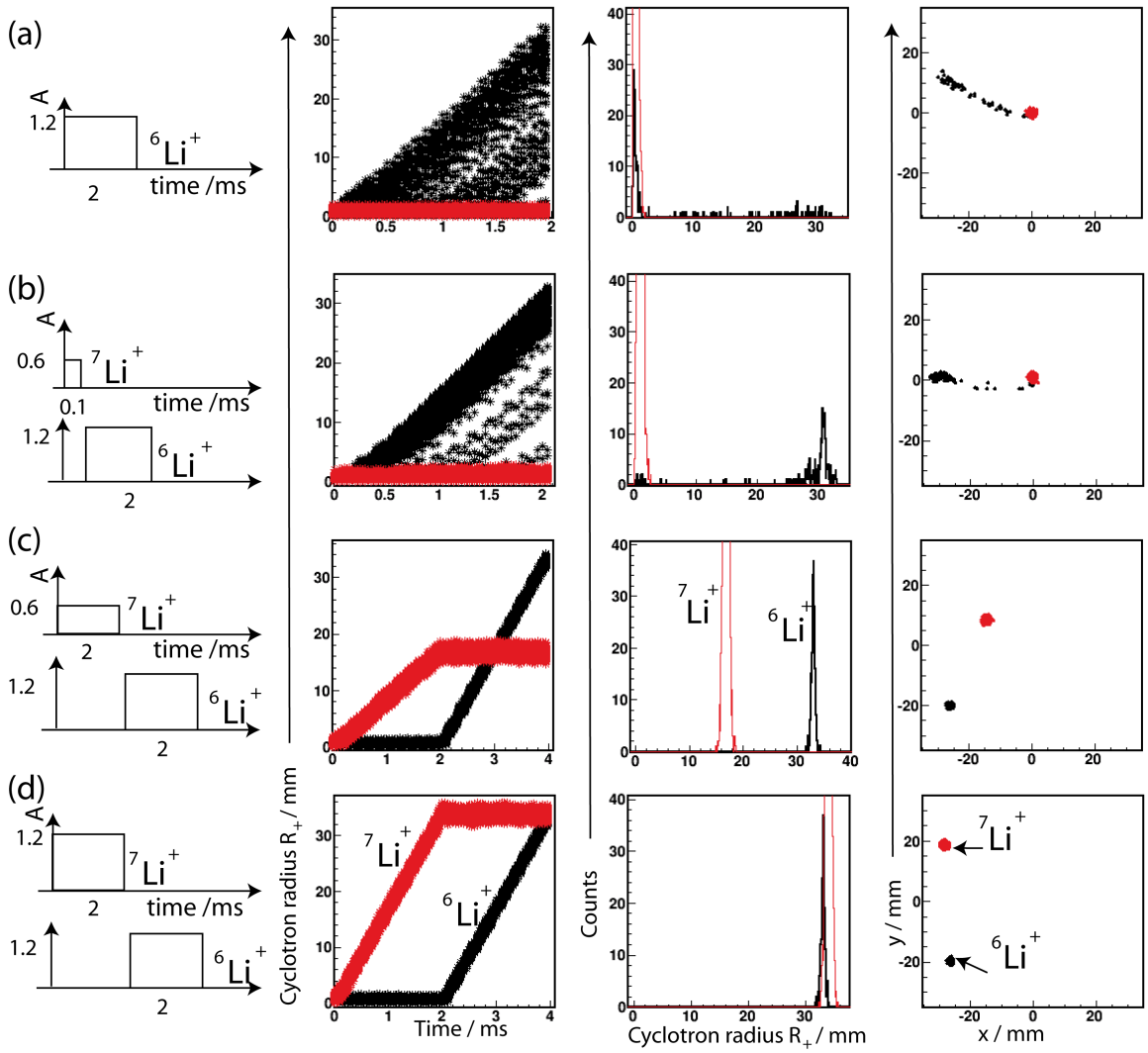

Figure 5.14: SIMBUCA simulations of an ion cloud of 4096×30 ions with 93% of $^7Li^+$ ions (red points) and 7% of $^6Li^+$ ions (black points). The left column shows the timing scheme of the excitations used for the simulations and their corresponding amplitudes. The ions were excited with a dipolar rf field at their eigenfrequency ν_+. The second column shows the cyclotron radius R_+ as a function of time, the third column the distribution of the cyclotron radii after excitations and the right column shows the position of the ions in the $x-y$-plane after excitations. One can see that a low excitation amplitude for $^7Li^+$ like in panel (a) and (b) leads to a lower cyclotron radius of $^6Li^+$ ions compared to the panels (c) and (d).

both species can be separated. Here the ions form only a condensed part which moves phase coherent in the Penning trap. This is reflected by the narrow ion distribution.

The phenomena observed in the simulations can be compared to the experimental data described in Section 5.3.3. First, the Fourier amplitude of the $^6Li^+$ ions is observed only if the $^7Li^+$ ions are pre-excited with a dipolar field at $\tilde{\nu}_+$. The excitation field for the $^6Li^+$ ions is shielded by the charges, as seen from the simulations (panel (a) and panel (b)). Secondly, in the measurement a maximum Fourier signal for $^6Li^+$ is observed (see Fig. 5.12 (d)). The simulation shows that the $^6Li^+$ ions stay phase locked when both ion species are spatially separated (panel(c)). Third, when the ions have the same cyclotron radius, no Coulomb interaction between the two ion clouds is observed in the simulation. This is different to the experimental observation. The difference can arise from the fact that we assumed an ideal trap and the image charge interaction are neglected. All together, the phenomena could be nicely described by the simulations.

5.4.2 Debye shielding of a quadrupolar excitation field

When many particles are stored in a Penning trap space charges influence the interaction of the ions with the quadrupolar excitation field. In consequence the interconversion of modes shows deviations from the single particle behaviour. The experimental results were presented in Section 5.3.3. It was observed that a conversion from the magnetron mode into the cyclotron mode for $^6Li^+$ ions is impossible if the $^7Li^+$ ions are not pre-excited at $\tilde{\nu}_+$ with the dipolar rf field. A SIMBUCA simulation using 4096 particles with a scaling factor of 30, i.e. in total $1.2{\cdot}10^5$ ions, has been performed. The electric and magnetic fields and the initial conditions of the cloud are the same as in Section 5.4.1. In these studies, a quadrupolar excitation at ν_c for $^6Li^+$ ions was investigated for various cyclotron radii of $^7Li^+$ ions.

Figure 5.15 shows the timing scheme of the excitation in the left column, the magnetron radius R_- as a function of time is shown in the middle column and the cyclotron radius R_+ as a function of time is shown in the right column. The red points represent the $^7Li^+$ ions and the black points represent the $^6Li^+$ ions.
Panel (a) shows a simulation where the Coulomb force between the particles was disabled. Application of a resonant quadrupolar rf field leads to a conversion of the initial magnetron motion into a pure cyclotron motion. The interconversion between the motional modes follows the theoretical description. Panel (b) shows a simulation using exactly the same excitation scheme as in panel (a) but the Coulomb force between the particles is enabled. In this case the space charge lead to a complete different behaviour during the application of the quadrupolar rf field. The ion cloud shields the quadrupolar excitation

field. In this simulation no interconversion could be observed.

In order to reflect the experimental results described in Section 5.3.3, an additional dipolar pre-excitation field at the modified cyclotron frequency of the $^7Li^+$ ions is applied as shown in panels (c) and (d). In case of (c), the cyclotron radius of the $^7Li^+$ ions is about 1.3 mm. The charges still shield the quadrupolar excitation field at ν_c of the $^6Li^+$ ions and influence the interconversion of modes. One can see that the interconversion is not complete and, additionally, the cyclotron radius of the $^7Li^+$ ions is spread.

In case of (d), the $^7Li^+$ ions were excited to a large radius (13.3 times larger than in (c)), so that both species are spatially separated from each other. The Coulomb interaction between the $^6Li^+$ ions and the $^7Li^+$ ions is negligible and the quadrupolar excitation field leads to the desired conversion from the initial magnetron to the cyclotron motion. The conversion time τ_c is equal to 1.1 ms as in the case without the Coulomb force shown in (a). These results are in agreement with the effects observed in the measurements (see Fig. 5.13).

As shown in the experimental results (see Section 5.3.3), a convenient way to avoid this Debye shielding is to separate the ion species using a dipolar excitation field at the modified cyclotron frequency of the higher abundant species.

5.5 Determination of the magnetic field imperfections

The sideband frequency $\tilde{\nu}_c$ is proportional to the magnetic field $B = B_0 + B_2 z^2$, where B_2 describes the magnetic bottle term. Therefore, the measurement of $\tilde{\nu}_c$ at different axial positions can be used to determine the term B_2. In this measurement, the Penning trap was moved along the z-axis by $\pm 15(1)$ mm. Figure 5.16 shows the normalized sideband frequency as a function of the axial position of the Penning trap. The data are fit with a quadratic function, resulting in a magnetic bottle term B_2 of $-42(5)\,\mathrm{mT\,m^{-2}}$.

The measured value can be compared with the one from the NMR probe measurement (see Section 3.7) where a B_2 of $-65(2)\,\mathrm{mT\,m^{-2}}$ has been determined. The magnetic bottle term derived from the ion measurement deviates by 4σ from the NRM probe measurement. Two reasons can cause this deviation. First, the magnetization of the materials has an impact on the B_2 value. While the measurement with the NMR probe is only surrounded by the stainless steel tube, the ions feel additionally the magnetization of the Penning trap. Secondly, the position of the probe in the magnetic field changed the B_2 value since the magnetic field is tilted and shifted. The NMR probe was adjusted to the magnet bore axis, while the ions perform a cyclotron motion and a magnetron motion, thus they probe the magnetic field far off-center. For further considerations the measured value with the ions will be used to calculate frequency shifts since the magnetic field was

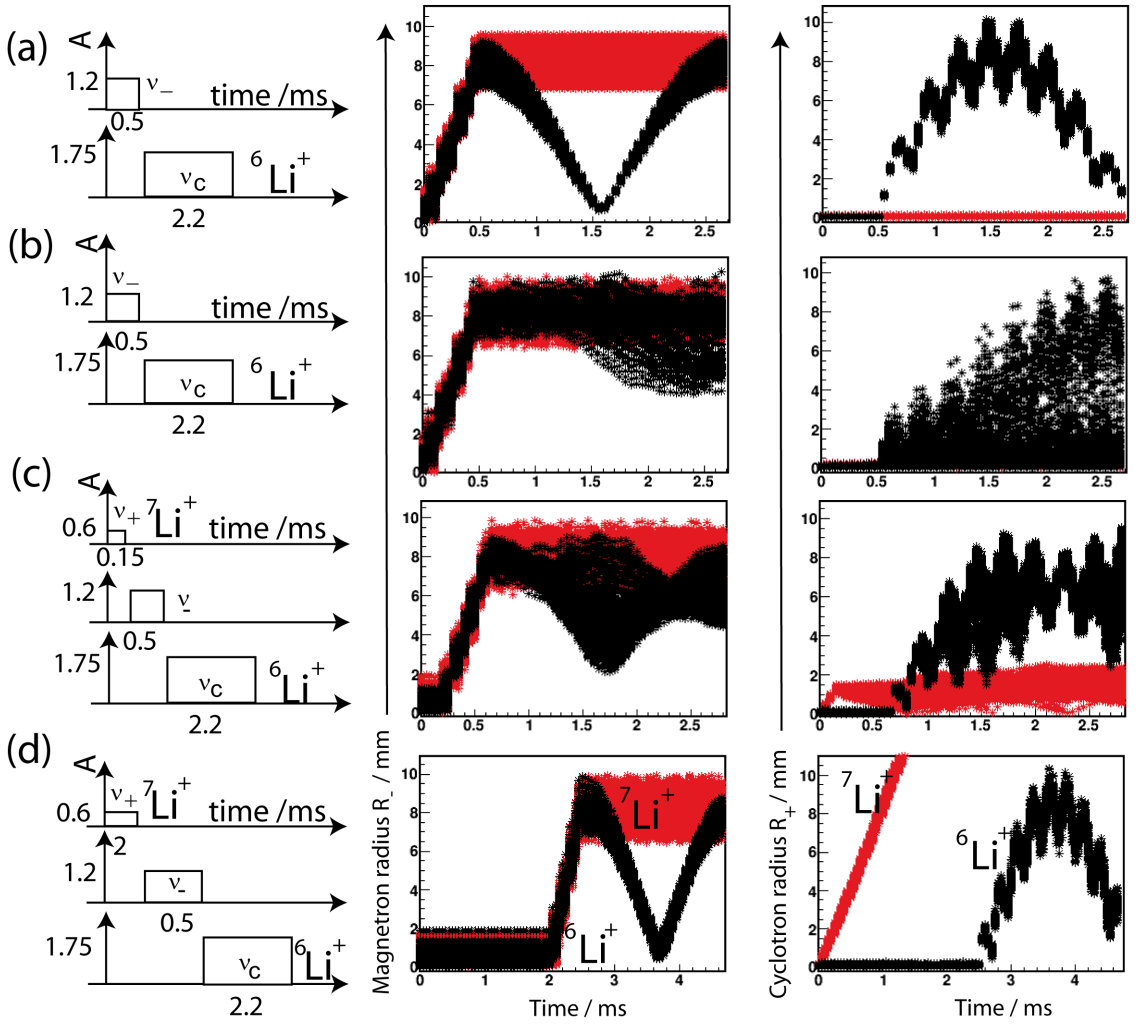

Figure 5.15: SIMBUCA simulations of an ion cloud with 4096×30 ions, with 93% of $^7Li^+$ ions (red points) and 7% of $^6Li^+$ ions (black points). In panel (a), the Coulomb interaction between the particles was not taken into account while in the panels (b), (c) and (d) the Coulomb interaction was enabled. The left column show the timing scheme, the middle column the magnetron radius $R_-(t)$ and the right column the cyclotron radius $R_+(t)$. For each result the same initial conditions were used. For details see text.

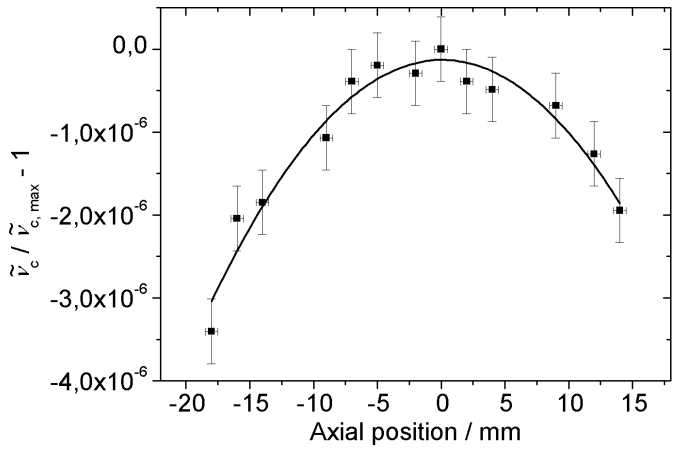

Figure 5.16: The sideband frequency $\tilde{\nu}_c$ was measured and normalized to its maximum value determined with $^7Li^+$ ions. The position of the Penning trap was shifted along the axial direction. The black curve is a quadratic fit to yield the magnetic bottle term.

probed off-center.

5.6 Frequency ratio measurements

For the determination of the accuracy of a mass measurement with the FT-ICR mass spectrometer, frequency ratio measurements have been carried out. The accuracy limit studies are of special importance for the KATRIN experiment since the $^3He^+$ and T^+ ions need to be resolved in order to determine the relative abundance. For resolving these two ion peaks in the dipolar frequency spectrum, a resolving power better than 10^4 is needed. For the frequency ratio measurements presented here, the $^{6,7}Li^+$ ion species were chosen because they are in a similar mass range as the ions expected in the KATRIN beam line. Here, three methods for a frequency ratio determination are presented.
The masses of both lithium isotopes are used in high-precision experiments as reference ions because both mass values are well known. The mass of $^7Li^+$ has been determined at SMILETRAP as $m_1 = 7.016\,003\,425\,6(45)$ u [83] with a relative uncertainty of 0.63 ppb, and the $^6Li^+$ mass has been measured at TITAN as $m_2 = 6.015\,122\,889(26)$ u with a relative uncertainty of 4.3 ppb [84]. The frequency ratio is given by $R_{\mathrm{lit}} = \nu_{c,1}/\nu_{c,2} = q_1 m_2/(q_2 m_1) = 0.857\,332\,053\,6(37)$ [84]. Throughout this section, the determined frequency ratio values are compared with the literature value.

5.6.1 Frequency shifts measurements

To determine the frequency ratio for the various methods presented here, the frequencies $\tilde{\nu}_+$ and $\tilde{\nu}_c$ of both lithium isotopes have to be measured. As already mentioned in Section 2.1.2, the frequencies of the ions in a real Penning trap depend on the motional amplitudes. This is due to field imperfections, image charge effects and relativistic effects. Distortion of fields leads to a magnetron frequency dependent frequency shift. Therefore, the frequencies were measured as a function of the cyclotron radius. First, the amplitude scan method is described. These data are fit with a model describing the frequency shift. From this model the frequency at vanishing cyclotron radius is extrapolated, which was later on used for the frequency ratio determination.

The measurement method: The measurement method is similar as the one already described in Section 5.3.2. The timing scheme is exactly the same but in this section the excitation amplitude was scanned for both ion species. When scanning the $^6Li^+$ amplitude, the excitation amplitude for $^7Li^+$ is 4.5 V in order to reduce the effects due to space charges. Here, the dipolar and the quadrupolar spectra are computed, in order to measure the frequencies $\tilde{\nu}_+$ and $\tilde{\nu}_c$.

For the $^7Li^+$ ions the measurement of $\tilde{\nu}_+$ and the Fourier amplitude $W^d_{\tilde{\nu}_+}$ has already been presented in Fig. 5.12 for a trapping potential of 35 V. For the $^6Li^+$ ions a similar excitation amplitude scan is shown in Figure 5.17 (a). The frequencies $\tilde{\nu}_+$ and $\tilde{\nu}_c$ were measured as a function of the $^6Li^+$ excitation amplitude at a trapping potential of 35 V. For an excitation amplitude range from 0.3 V to 2.5 V, the frequency decreases by 23 Hz for $\tilde{\nu}_+$ and by 13 Hz for $\tilde{\nu}_c$. Panel (a) shows the expected quadratic decrease of the frequencies with the excitation amplitude according to Eq. (2.25). The frequency shift of $\tilde{\nu}_c$ is lower compared to $\tilde{\nu}_+$, which is due to the fact that no magnetic bottle term appears for the cyclotron radius dependent part of the $\Delta\tilde{\nu}_c$ shift.

Fit model: The measured frequency shifts of $\tilde{\nu}_+$ and $\tilde{\nu}_c$ are fit with a quadratic function. In this section only the first order frequency shifts are regarded, which depend quadratically on the motional amplitude, according to Eq. (2.25). Here higher order corrections to the frequency are neglected. The fit function to the data is given by

$$\tilde{\nu}_{+/c,i} = \bar{\nu}_{+/c,i} + \frac{1}{2} a_{+/c,i} U^2_{exc} \tag{5.7}$$

where i is the index of the ion species ($i = 1$ for $^7Li^+$ and $i = 2$ for $^6Li^+$), $a_{+/c,i}$ is the slope in units [Hz/V^2] and $\bar{\nu}_{+/c,i}$ is the extrapolated frequency at $R_+ = 0$ mm. Equation (5.7) is only true if the cyclotron radius R_+ is proportional to the applied excitation amplitude.

Therefore, for the fit to the data, only an excitation amplitude interval is chosen where the Fourier signal increases linearly with the excitation amplitude.
The extrapolated frequencies $\bar{\nu}_{+/c,i}$ for a cyclotron radius R_+ equal to zero result from Eq. (5.7). These frequencies will be used to evaluate the various frequency ratios given later in this section. These frequencies still include additional frequency shifts which arise from the magnetron radius R_-, the axial amplitude R_z, the image charge shifts, the Coulomb effects and the distortion of fields which are given in detail in the following sections.

For the interpretation of the measurement results it is assumed that the trajectory of the ion beam does not change in time. The ions were always injected at the same trap position. But notice that the ions were injected off-center which causes an initial magnetron radius. The magnetron motion couldn't be avoided since the ions were guided by the magnetic field which is shifted and tilted at the trap position (see Section 3.7 for the magnetic field map). The magnetron radius R_- is equal to the distance of the position of the ions to the trap center.

The axial oscillation rises up from the axial kinetic energy of the ions. To study systematic frequency shifts it is important to know the amplitude of the axial motion. For this a simulation with the program SIMION has been performed. This program calculates the trajectory of an ion in an electromagnetic field. The model implements the geometry of the current cylindrical Penning trap using a trapping voltage of 35 V and a magnetic field of 4.699 T. The ions are equally distributed over an area of a circle with a radius of 1 mm before they are guided into the Penning trap. The ions move parallel to the magnetic field vector, so that no cyclotron motion occurs ($R_+ = 0$ mm). The axial kinetic energy is 20 eV. The injection endcap is switched within a time of 100 µs from 0 V to 35 V. After the trapping, the ions perform a magnetron motion and an axial oscillation. The x, y and z coordinates of the trapped ions are recorded every µs for a duration of 2 ms, in order to observe a full magnetron period. Figure 5.18 shows the probability of presence of the ions along the trap axis. One can see that the probability is maximum at the turnaround point at $z_{\max} = \pm 16$ mm, which is well below the length of the ring electrode $z_r = 56$ mm. As expected, the probability follows exactly the classical harmonic oscillator, which is described by $A/\sqrt{1-(z/z_{\max})^2}$. For further systematic calculations presented in this section an axial amplitude of 16 mm will be used.

Figure 5.17 (b) shows the frequencies $\bar{\nu}_{+,1}$ extrapolated to $R_+ = 0$ mm for $^7Li^+$ as a function of the trapping potential V_0. As expected the modified cyclotron frequency decreases linearly with V_0. The data are fit with Eq. (5.1) and two fit parameters are deducted: The magnetic field B and the coefficient C_2/d^2. Using this method for both lithium isotopes, a mean value of $C_2/d^2 = 812(30)\,\mathrm{m}^{-2}$ is derived.

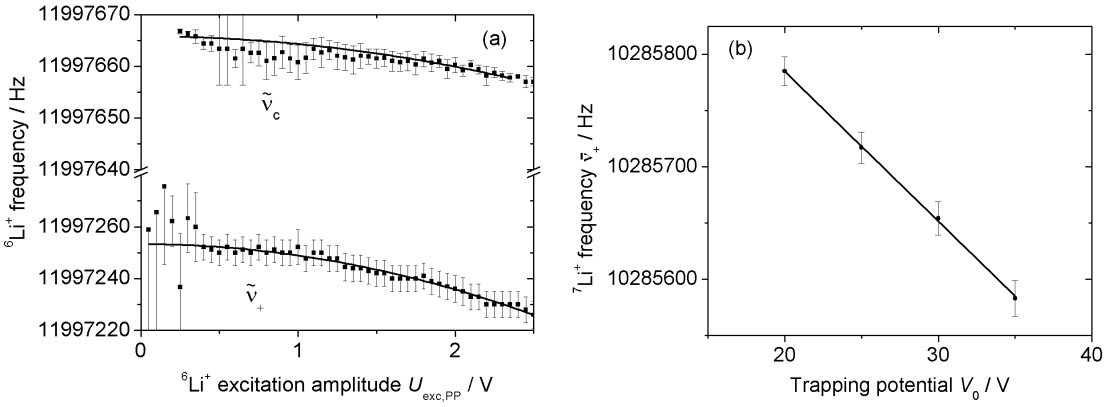

Figure 5.17: (a) Measured frequencies $\tilde{\nu}_{+,2}$ and $\tilde{\nu}_{c,2}$ of $^6Li^+$ from the dipolar and quadrupolar detections as a function of the excitation amplitude for $^6Li^+$ at a trapping potential of 35 V. The excitation amplitude for $^7Li^+$ was kept constant. The black lines are fits of Eq. (5.7) to the data. Both frequencies were simultaneously measured. (b) Modified cyclotron frequency $\bar{\nu}_{+,1}$ of $^7Li^+$ as a function of the trapping potential. The black line is a fit of Eq. (5.1) to the data.

The electrostatic coefficient C_2/d^2 was also determined by an analytical model as explained in Section 3.5.1. With a d parameter of 26.6 mm one obtains $C_2 = 860\,\mathrm{m}^{-2}$. The measured value deviates by about 1.5 standard deviations from this value. This can be explained by the fact that for a cylindrical trap the C_2 value depends on the radius. Since the ions perform a cyclotron and magnetron motion, they probe the electrostatic trapping field off-axis.

5.6.2 Frequency ratio determination using the dipolar detection method

The frequency ratio was determined from the measurement of the modified cyclotron frequencies $\tilde{\nu}_{+1}$ and $\tilde{\nu}_{+2}$ from the dipolar frequency spectra (see Fig. 5.3 (a)). The frequency ratio R_1 is calculated using the modified cyclotron frequencies $\bar{\nu}_{+,i}$ which are extrapolated to $R_+ = 0\,\mathrm{mm}$

$$R_1 = \frac{\bar{\nu}_{+,1}}{\bar{\nu}_{+,2}}. \tag{5.8}$$

Figure 5.19 (a) shows the deviation of the frequency ratio from the literature value $R_1 - R_{\mathrm{lit}}$ as a function of the trapping potential V_0. The error bars in the plot include statistical and systematic errors. The deviation from the literature value decreases when the trapping potential decreases. This is a direct consequence of neglecting the magnetron frequency $\tilde{\nu}_-$ in Eq. (5.8) because the modified cyclotron frequency for $^6Li^+$ is larger than for

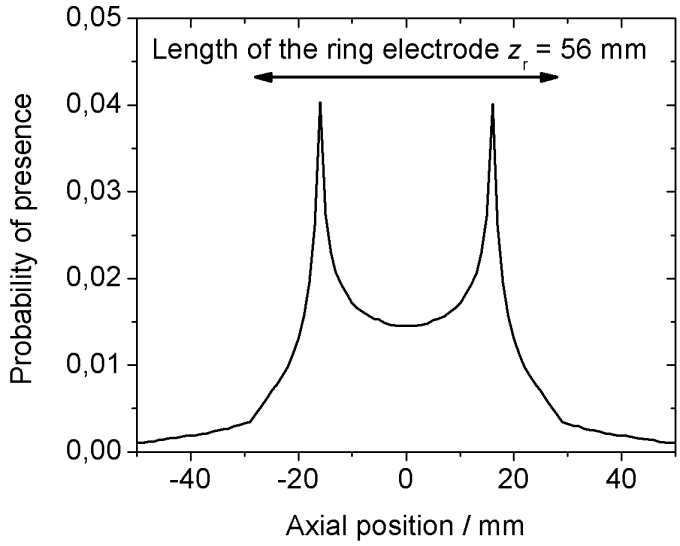

Figure 5.18: SIMION simulation of confined ions in a Penning trap for a trapping potential of 35 V and an ion energy of 20 eV. The trap center is at $z = 0$ mm. The ion trajectory is recorded every 1 µs. The probability of presence along the trap axis follows exactly the classical harmonic oscillator. The turning point at $z = \pm 16$ mm is inside the length of the ring electrode.

$^7Li^+$. For a trapping potential of 20 V the deviation from the literature value $R_1 - R_{lit}$ is $-2.19(3)_{stat}(148)_{sys} \cdot 10^{-6}$.

The main contribution to the systematic error arises from the finite magnetron radius and the axial amplitude, which lead to a frequency shift according to Eq. (2.25). As discussed in Section 5.6.1, the conservative values for these motions are $R_- = 5$ mm and $R_z = 16$ mm, leading to a frequency shift of 1.3 ppm for $^7Li^+$ and of 1.3 ppm for $^6Li^+$ for a trapping potential of 20 V. The interaction of the ions with its induced charges on the ring electrode leads to a frequency shift. Here, for roughly 10^5 particles, the frequency shift is 40 ppt, calculated with Eq. (2.26). Referring to [8], the frequency ν_+ of an ideal trap is equal to $\nu_+(\theta, \varepsilon)$ when only regarding misalignment and distortion of the fields. During the measurement time t_{meas} of 60 min, the decay rate and fluctuations of the magnetic field (see Section 3.7) lead to a frequency shift of 0.1 ppb. This value is negligible, since it is much below the resolving power of the mass spectrometer. The total systematic uncertainty results from the quadratically sum of the uncertainties mentioned before.

For further systematic studies, the measurements have to be performed with only one trapped ion species. Moreover, the initial magnetron radius and the axial amplitude have to be reduced.

5.6.3 Frequency ratio determination using the dipolar and the quadrupolar detection method

The frequency ratio is determined by using the dipolar and the quadrupolar detection method. The frequency ratio is derived when the modified cyclotron frequency was measured from the dipolar frequency spectra and the magnetron frequency $\tilde{\nu}_-$ was determined by the method described in Section 5.1.3. Here, $\tilde{\nu}_-$ is determined by $\bar{\nu}_{-,1} = \bar{\nu}_{c,1} - \bar{\nu}_{+,1}$ using the $^7Li^+$ ions. The frequency ratio R_2 is defined by

$$R_2 = \frac{\bar{\nu}_{+,1} + \bar{\nu}_{-,1}}{\bar{\nu}_{+,2} + \bar{\nu}_{-,1}}, \tag{5.9}$$

where $\bar{\nu}_{+,i}$ are the same frequencies as in the previous section. Figure 5.19 (b) shows the deviation of the frequency ratio from the literature value $R_2 - R_{lit}$ as a function of the trapping potential. Since the magnetron frequency is taken into account, a better accuracy is achieved compared to the method presented in the previous section. For a trapping potential of 20 V a value of $0.84(4)_{stat}(148)_{sys} \cdot 10^{-6}$ is determined. The accuracy gets slightly better compared to the method described in the previous section when decreasing the trapping potential. The systematic uncertainty decreases, since the frequency shifts depend on the magnetron frequency.
The systematic error on the modified cyclotron frequency is the same as described in the previous section. Additionally, the systematic error on the magnetron frequency has to be considered. Using Eq. (2.25) the difference $\Delta\nu_c - \Delta\nu_+$ results in a relative shift of 0.2 ppm.

5.6.4 Frequency ratio determination using the quadrupolar detection method

The detection of the sideband frequency $\tilde{\nu}_c$ with the quadrupolar detection method is very important since it is a direct way for mass determination. As explained in Section 5.1.3, the measured cyclotron frequency is accessible if the ions perform simultaneously a magnetron motion and a cyclotron motion. The frequency ratio R_3 is defined by

$$R_3 = \frac{\bar{\nu}_{c,1}}{\bar{\nu}_{c,2}}. \tag{5.10}$$

Figure 5.20 shows the deviation of the frequency ratio from the literature value as a function of the trapping voltage. The frequency ratio is closer to the literature value when the trapping potential is smaller. At a trapping potential of 20 V the deviation of the frequency ratio from the literature value $R - R_{lit}$ is $2.65(2)(131) \cdot 10^{-6}$, which is 2σ away

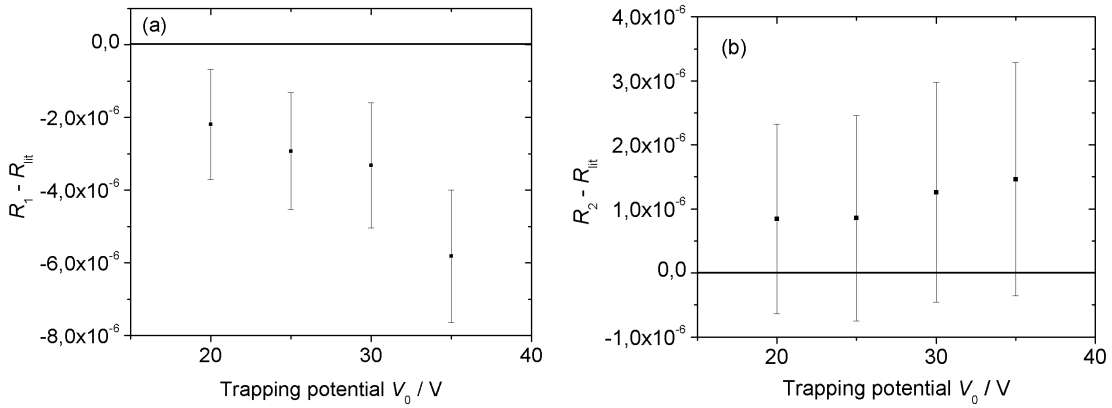

Figure 5.19: (a) Deviation of the frequency ratio from the literature value $R - R_{\mathrm{lit}}$ at four different trapping potentials V_0. (a) The modified cyclotron frequency $\bar{\nu}_{+/\mathrm{c},i}$ was used to calculate the ratio R_1. In panel (b) the frequency ratio R_2 is derived by using the sum of the modified cyclotron frequency $\bar{\nu}_{+/\mathrm{c},i}$ and the magnetron frequency. For details see the text.

from the literature value. The deviation arises from the measured frequency $\tilde{\nu}_{\mathrm{c}}$ of $^6\mathrm{Li}^+$, which shifts 6 times stronger with the trapping potential than the $^7\mathrm{Li}^+$ data. A possible explanation can be that a larger trapping potential increases the ion density. Thus, the created space charge potential is stronger and the trapping potential is modified by the charges of the higher abundant $^7\mathrm{Li}^+$ ions.
The main contribution of the systematic error arises from the frequency shift due to the magnetron and axial motions. This is calculated with Eq. (2.25) and results in 0.93 ppm. Additionally, a frequency shift of 48 ppt due to distortion of fields and misalignment is taken into account.

5.6.5 Comparison of the frequency ratio measurements

The results of the deviation of the frequency ratio from the literature for the three methods are listed in Table 5.1. All three methods show nearly the same relative uncertainty. The highest accuracy is reached with the dipolar detection method when the magnetron frequency is known. For this method, an accuracy $(R - R_{\mathrm{lit}})/R_{\mathrm{lit}} \approx 0.98 \cdot 10^{-6}$ and a relative uncertainty $\Delta R/R \approx 1.73 \cdot 10^{-6}$ are achieved when using a trapping potential of 20 V. The determined value is within the literature value. The advantage of this method is that the modified cyclotron and the magnetron frequencies can be measured separately. This is useful when the quadrupolar Fourier amplitude is not detectable but only the dipolar Fourier amplitude. This can happen when measuring ion species with a low abundance.

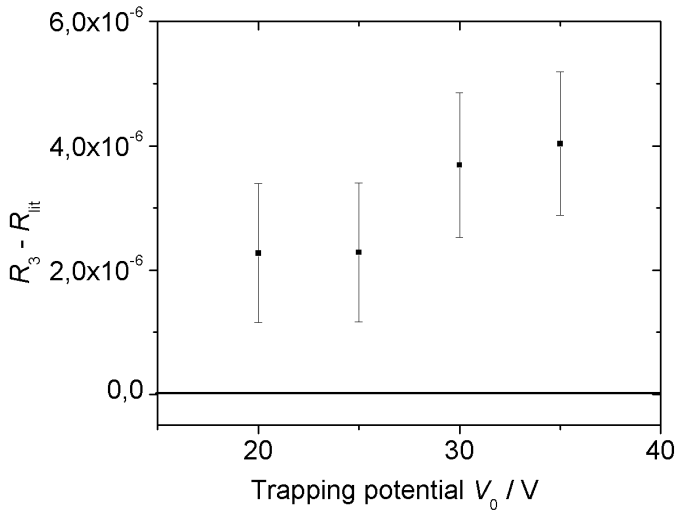

Figure 5.20: Deviation of the frequency ratio from the literature value $R_3 - R_{\mathrm{lit}}$ as a function of the trapping potential V_0. Here, the sideband frequency at $\bar{\nu}_{\mathrm{c},i}$ was measured with the quadrupolar detection.

For all presented methods, the accuracy can be improved by cleaning the ion beam from contaminants and measuring only one ion specie. The accuracy can be further improved when low trapping potentials are used.

To reduce the systematic uncertainties the following solutions can be applied to the setup: Experimentally, different techniques have to be applied to reduce the magnetron radius and the axial amplitude. Most commonly the buffer gas cooling technique is used, which is described in Section 2.2.3. With this technique, the cyclotron and axial radii are damped exponentially by the collisions with the buffer gas molecules, thus the ions are centered in the trap.

The frequency shifts due to electrostatic imperfections might also be decreased by using a lower trapping potential and using a compensated Penning trap. Such a trap with correction electrodes can minimize the coefficients C_4 and C_6. A cleaning mechanism of the unwanted ion species would reduce the Coulomb interaction between ion clouds of different species.

Frequency ratio method	$R_i - R_{\mathrm{lit}}$
R_1 from dipolar detection at $\bar{\nu}_{+,i}$	$-2.19(3)_{\mathrm{stat}}(148)_{\mathrm{sys}} \cdot 10^{-6}$
R_2 from dipolar detection at $\bar{\nu}_{+,i}$ with $\tilde{\nu}_{-}$-determination	$0.84(4)_{\mathrm{stat}}(148)_{\mathrm{sys}} \cdot 10^{-6}$
R_3 from quadrupolar sideband detection at $\bar{\nu}_{\mathrm{c},i}$	$2.65(2)(131) \cdot 10^{-6}$

Table 5.1: Comparison of the deviation of the frequency ratio to the literature value for the three presented methods. The values were taken for a trapping potential of 20 V. For more details see the text.

Chapter 6

Conclusion and Outlook

6.1 Conclusion and final achievements

The goal of this thesis was to build up and characterize a broad-band FT-ICR detection system. Such a system was successfully developed and used to investigate several excitation and detection schemes.

The broad-band amplifier system, used for converting the induced image currents into a voltage, was characterized. The pre-amplifier shows a white noise behaviour of $1\,\mathrm{nV}/\sqrt{\mathrm{Hz}}$ and a voltage amplification of about 6.5 in a broad frequency range from 0.2 MHz up to 30 MHz. Thus an ion detection with this pre-amplifier is possible in a mass-to-charge m/q range from 2 to 400 u/e.

The cylindrical Penning trap, developed for the KATRIN experiment, was characterized. In particular the deviations from an ideal quadrupolar potential were determined near the trap center by using an analytical model of an open-endcap cylindrical Penning trap. The harmonic term C_2/d^2 of $820(20)\,\mathrm{m}^{-2}$ was experimentally determined from the dependency of the modified cyclotron frequency on the trapping potential. Good agreement between the measurements and the model has been reported.

An FT-ICR control system has been developed to provide a flexible and stable control of the experiment. This system includes the control of the function generators for generating the excitation signals, the transient recorder for recording the ion signals and computing the dipolar and the quadrupolar detection schemes. This makes the possibility to combine easily several excitation schemes with several detection schemes.

A theoretical study describing the induced ion image charges on the detection plates of a cylindrical Penning trap was developed and adapted for both detection schemes to the experiment presented here. Time dependent image charges are derived in a form of a Fourier series whose coefficients depend on the magnetron and cyclotron amplitudes of

the ion motion. Therefore, the experimentally observed Fourier amplitudes at the combinations of interest of eigenfrequencies can be analyzed.

The FT-ICR dipolar detection scheme was used for the first time to investigate azimuthal one- and two-pulse (Ramsey) quadrupolar excitation schemes at the sideband frequency $(\nu_+ + \nu_-)$, using $^7Li^+$ ions. The FT-ICR dipolar signal was studied by varying important parameters such as excitation frequency, excitation time and waiting time. The two-pulse Ramsey excitation scheme shows that a longer total time reduces the statistic uncertainty for the determination of the cyclotron frequency. When varying the excitation time and using a constant waiting time the narrowest line-width reappears periodically at the Rabi period τ_R, which is twice the conversion time τ_c. A quantum mechanical model was built to understand the interconversion of the motional modes due to the interaction of a quadrupolar rf field with an ion. A general solution for the one- and two-pulse conversion profile functions was found. The measurements with the FT-ICR detection method demonstrated the validity of the derived profile function for both excitation schemes.

Coulomb effects between the ions were experimentally investigated using 10^5 lithium ions with their natural abundance, i.e. 93 % of $^7Li^+$ ions and 7 % of $^6Li^+$ ions. Due to the space charge, frequency shifts and a variation of the cyclotron radius of the ions were observed. When exciting the ion species at their modified cyclotron frequency with a dipolar excitation field, the higher abundant ion species is easier to excite than the lower abundant ion species. This is due to the Debye shielding of the applied dipolar field by the ion cloud. When the higher abundant species is first excited by a strong dipolar rf field then the lower abundant species could be excited for both excitation schemes. Thus, the Debye shielding could be avoided. For a quadrupolar excitation field two phenomena were observed in the resonance scans of the lower abundant species. The resonance shape depend on the dipolar excitation amplitude of the higher abundant species. Here a suppression of sidebands and a decrease of the frequency resolving power was observed. These are important results for future studies when for example two isobaric species with a high abundance have to be resolved.

In order to understand the observed shielding effects, N Coulomb interacting particles in a Penning trap were studied numerically with the open source software SIMBUCA. A total number of $1.2 \cdot 10^5$ Coulomb interacting particles was simulated by exciting the two lithium ion species with a dipolar or a quadrupolar excitation field. The simulations confirm that many stored ions shield any applied rf field as observed in the experiment. The simulation as well as the experiment showed that the two ion species have to be spatially separated in order to perform a manipulation of the motional mode.

The Penning trap will be installed in the beam line of the KATRIN experiment to identify ion species and ion clusters. Therefore, accuracy and precision limit studies were

carried out to determine the frequency ratio of $^7Li^+$ to $^6Li^+$ ions with three methods. The ions were excited with a dipolar rf field and detected with the dipolar and the quadrupolar method. The three methods showed comparable results on the evaluated frequency ratio. The highest accuracy $(R - R_{lit})/R_{lit}$ of approximately $0.98 \cdot 10^{-6}$ with a relative uncertainty of $1.73 \cdot 10^{-6}$ was reached by detecting the modified cyclotron frequency and measuring the magnetron frequency separately. The systematic uncertainties are mainly due the trap field imperfections, which lead to frequency shifts due to the initial magnetron radius and the axial amplitude. This initial magnetron motion results from the shifted and tilted magnetic field which leads to an unavoidable off-center trapping since the ions are guided by the magnetic field. Avoiding this motion was not possible since it was found that the superconducting magnet has two out of three broken shim-coils. The magnetic field in an axial direction was improved by loading the z-shim-coil with a different shim current. But x, y-shim coils could not be loaded with any shim current since probably the heater units are broken. It is almost impossible to perform experiments where well-defined initial conditions require centered ions, like in the case of an octupolar excitation scheme.

Finally the FT-ICR Penning trap mass spectrometer for the KATRIN project was succesfully completed and delivered. The cryogenic amplifiers were tested and fulfill the requirements of a low-noise behaviour of $1\,nV/\sqrt{Hz}$ for frequencies higher than 1 MHz. Also the required sensitivity limit, resolving power and accuracy as explained above, is sufficient to resolve the $^3He^+$ and T^+ ions.

6.2 Outlook, the PIPERADE project

After the KATRIN project, the FT-ICR setup in Heidelberg will be used in the context of the PIPERADE (PIège de PEnning pour des ions RAdioactifs à DEsir) project [85]. The Piperade setup will be located in DESIR (Désintégration Excitation et Stockage d'Ions Radioactifs), the low-energy part of the future SPIRAL2 facility (Système de Production d'Ions RAdioactifs en Ligne de 2^{eme} génération). SPIRAL2 is an extension to the existing GANIL (Grand Accélérateur National d'Ions Lourds) accelerator located in Caen, France. The PIPERADE setup will be used to purify the radioactive beam from undesired ion species.

When producing the ion of interest by nuclear reactions a huge amount of isobaric contaminants is created at the same time. In order to remove these isobaric ion species a system with a high resolving power is needed. The ions will be first separated by a High Resolution Separator (HRS). Since higher resolving power and further separation are needed, the ions will be guided after the HRS into the PIPERADE setup, located at the entrance of the DESIR hall. The requirements for this system are the following:

- A large trapping capacity up to 10^7 ions due to the ratio between the contaminants and the ions of interest.
- A high mass resolving power of $m/\Delta m > 10^5$ in order to separate isobaric species.
- A short separation time of a few 100 ms to a few 10 s due to the limit of the half-life of the nuclei.

The project needs to find new ways to purify and accumulate exotic nuclei. To reach this goal two solutions are discussed so far: (i) A setup consisting of two Penning traps. The first one can be used for mass selection with a high-resolving power and the second one is used to store, accumulate and cool the ions. (ii) A system consisting of a Multi-Reflection Time-Of-Flight (MR-TOF) mass spectrometer which is used to clean and purify the ion beam [86] and behind a Penning trap for accumulating and cooling the ions.

In addition, since up to 10^7 ions will be stored one has to regard the nonneutral plasma physics. Here, another excitation scheme like the rotating wall, which is a circular polarized dipolar excitation, provides a way to compress or expand the ion cloud when exciting at the rotating frequency of the ion cloud [76]. Also combinations of a dipolar and quadrupolar excitation field are possible to purify a sample. For example, one can use simultaneously a dipolar excitation at the magnetron frequency and a quadrupolar field at the sideband frequency in order to obtain a centering of the ions without buffer-gas [87]. Also a dipolar excitation at the modified cyclotron frequency and an axial quadrupolar field which couples the cyclotron motion to the axial motion can be chosen to separate ion species. The first simulations with SIMBUCA and experimental tests concerning the separation of ion species for the PIPERADE project have already been started in Heidelberg.

Bibliography

[1] A. Einstein. *Annal. Phys.*, 18:639, 1905.

[2] K. Blaum, H. Kracke, S. Kreim, A. Mooser, C. Mrozik, W. Quint, C. C. Rodegheri, B. Schabinger, S. Sturm, S. Ulmer, et al. g-factor experiments on simple systems in Penning traps. *Journal of Physics B: Atomic, Molecular, and Optical Physics*, 42(15):154021, 2009.

[3] D. Lunney, J. M. Pearson, and C. Thibault. Recent trends in the determination of nuclear masses. *Reviews of Modern Physics*, 75(3):1021–1082, August 2003.

[4] K. Blaum. High-accuracy mass spectrometry with stored ions. *Physics Reports*, 425(1):1–78, 2006.

[5] W. Shi, M. Redshaw, and E. G. Myers. Atomic masses of ^{32,33}S , ^{84,86}Kr , and ^{129,132}Xe with uncertainties ≤ 0.1 ppb. *Physical Review A*, 72(2):022510, 2005.

[6] D. Lunney, J. M. Pearson, and C. Thibault. Recent trends in the determination of nuclear masses. *Rev. Mod. Phys.*, 75:1021–1082, Aug 2003.

[7] A. G. Marshall. Milestones in fourier transform ion cyclotron resonance mass spectrometry technique development. *International Journal of Mass Spectrometry*, 200:331–356, December 2000.

[8] L. S. Brown and G. Gabrielse. Geonium theory: Physics of a single electron or ion in a Penning trap. *Reviews of Modern Physics*, 58(1):233–311, January 1986.

[9] G. Gabrielse. Antiproton mass measurements. *International Journal of Mass Spectrometry*, 251:273–280, April 2006.

[10] The ALPHA Collaboration. Confinement of antihydrogen for 1,000 seconds. *Nature Physics*, 7:558–564, 2011.

[11] The ALPHA Collaboration. Resonant quantum transitions in trapped antihydrogen atoms. *Nature*, 483:439–443, March 2012.

[12] G. Gräff. A direct determination of the proton electron mass ratio. 297(1):35–39, March 1980.

[13] A. G. Marshall, C. L. Hendrickson, and G. S. Jackson. Fourier transform ion cyclotron resonance mass spectrometry: a primer. *Mass spectrometry reviews*, 17(1):1–35, 1998.

[14] M. B. Comisarow and A.G. Marshall. Fourier transform ion cyclotron resonance spectroscopy. *Chemical Physics Letters*, 25:282–283, March 1974.

[15] S. Ulmer, H. Kracke, K. Blaum, S. Kreim, A. Mooser, W. Quint, C. C. Rodegheri, and J. Walz. The quality factor of a superconducting rf resonator in a magnetic field. *Review of Scientific Instruments*, 80(12):123302–123302–8, December 2009.

[16] E. W. Otten and C. Weinheimer. Neutrino mass limit from tritium decay. *Reports on Progress in Physics*, 71(8):086201, August 2008.

[17] M. Heck, K. Blaum, R. Cakirli, M. Kretzschmar, G. Marx, D. Rodriguez, L. Schweikhard, S. Stahl, and M. Ubieto-Diaz. One- and two-pulse quadrupolar excitation schemes of the ion motion in a Penning trap investigated with FT-ICR detection. *Applied Physics B: Lasers and Optics*, 107(4):1019–1029, 2012.

[18] N. F. Ramsey. A New Molecular Beam Resonance Method. *Physical Review*, 76:996, October 1949.

[19] N. F. Ramsey. A Molecular Beam Resonance Method with Separated Oscillating Fields. *Physical Review*, 78:695, June 1950.

[20] K. Blaum, Yu N. Novikov, and G. Werth. Penning traps as a versatile tool for precise experiments in fundamental physics. *Contemporary Physics*, 51(2):149–175, 2010.

[21] S. Earnshaw. *Trans. Camb. Phil. Soc.*, 7:97–112, 1842.

[22] Hans Dehmelt. *Rev. Mod. Phys.*, 62:525–530, Jul 1990.

[23] J. Repp, C. Böhm, J. Crespo Lopez-Urrutia, A. Dörr, S. Eliseev, S. George, M. Goncharov, Y. Novikov, C. Roux, S. Sturm, S. Ulmer, and K. Blaum. PENTATRAP: a novel cryogenic multi-Penning-trap experiment for high-precision mass measurements on highly charged ions. *Applied Physics B: Lasers and Optics*, 107(4):983–996, 2012.

[24] G. Bollen, H.-J. Kluge, M. König, T. Otto, G. Savard, H. Stolzenberg, R. B. Moore, G. Rouleau, G. Audi, and ISOLDE Collaboration. Resolution of nuclear ground and isomeric states by a Penning trap mass spectrometer. *Physical Review C*, 46(6):R2140–R2143, December 1992.

[25] X. Xiang, P. B. Grosshans, and A. G. Marshall. Image charge-induced ion cyclotron orbital frequency shift for orthorhombic and cylindrical FT-ICR ion traps. *International Journal of Mass Spectrometry and Ion Processes*, 125(1):33–43, May 1993.

[26] G. Gabrielse. The true cyclotron frequency for particles and ions in a Penning trap. *International Journal of Mass Spectrometry*, 279(2-3):107–112, January 2009.

[27] L. Schweikhard and A. G. Marshall. Excitation modes for Fourier transform-ion cyclotron resonance mass spectrometry. *Journal of the American Society for Mass Spectrometry*, 4(6):433–452, June 1993.

[28] L. Schweikhard, M. Lindinger, and H.-J. Kluge. Parametric-mode excitation/dipole-mode detection Fourier-transform-ion-cyclotron-resonance spectrometry. *Review of Scientific Instruments*, 61(3):1055–1058, March 1990.

[29] S. Eliseev, M. Block, A. Chaudhuri, F. Herfurth, H.-J. Kluge, A. Martin, C. Rauth, and G. Vorobjev. Octupolar excitation of ions stored in a Penning trap mass spectrometer -A study performed at SHIPTRAP. *International Journal of Mass Spectrometry*, 262(1-2):45–50, April 2007.

[30] P. B. Grosshans and A. G. Marshall. General theory of excitation in ion cyclotron resonance mass spectrometry. *Analytical Chemistry*, 63(18):2057–2061, 1991.

[31] A. G. Marshall and D. C. Roe. Theory of Fourier transform ion cyclotron resonance mass spectroscopy: Response to frequency sweep excitation. *The Journal of Chemical Physics*, 73:1581–1590, August 1980.

[32] M. Kretzschmar. The Ramsey method in high-precision mass spectrometry with Penning traps: Theoretical foundations. *International Journal of Mass Spectrometry*, 264(2-3):122–145, July 2007.

[33] M. S. Zubairy M. O. Scully. Cambridge University Press.

[34] M. König, G. Bollen, H. J Kluge, T. Otto, and J. Szerypo. Quadrupole excitation of stored ion motion at the true cyclotron frequency. *International Journal of Mass Spectrometry and Ion Processes*, 142(1-2):95–116, 1995.

[35] S. George, K. Blaum, F. Herfurth, A. Herlert, M. Kretzschmar, S. Nagy, S. Schwarz, L. Schweikhard, and C. Yazidjian. The Ramsey method in high-precision mass spectrometry with Penning traps: Experimental results. *International Journal of Mass Spectrometry*, 264(2-3):110–121, July 2007.

[36] S. George, S. Baruah, B. Blank, K. Blaum, M. Breitenfeldt, U. Hager, F. Herfurth, A. Herlert, A. Kellerbauer, H.-J. Kluge, M. Kretzschmar, D. Lunney, R. Savreux, S. Schwarz, L. Schweikhard, and C. Yazidjian. Ramsey Method of Separated Oscillatory Fields for High-Precision Penning Trap Mass Spectrometry. *Physical Review Letters*, 98(16):162501, April 2007.

[37] G. Savard, St. Becker, G. Bollen, H.-J. Kluge, R.B. Moore, Th. Otto, L. Schweikhard, H. Stolzenberg, and U. Wiess. A new cooling technique for heavy ions in a Penning trap. *Physics Letters A*, 158(5):247–252, September 1991.

[38] M. B. Comisarow. Fundamental aspects of FT-ICR and applications to chemistry. *Hyperfine Interactions*, 81(1):171–178, 1993.

[39] H. Häffner, T. Beier, S. Djekiae, N. Hermanspahn, H.-J. Kluge, W. Quint, S. Stahl, J. Verdu, T. Valenzuela, and G. Werth. Double penning trap technique for precise g factor determinations in highly charged ions. *The European Physical Journal D*, 22(2):163–182, February 2003.

[40] S. Rainville, J. K. Thompson, and D. E. Pritchard. An Ion Balance for Ultra-High-Precision Atomic Mass Measurements. *Science*, 303(5656):334–338, January 2004.

[41] R. S. Van Dyck, S. L. Zafonte, S. Van Liew, D. B. Pinegar, and P. B. Schwinberg. Ultraprecise Atomic Mass Measurement of the α Particle and ^{4}He. *Physical Review Letters*, 92(22):220802, June 2004.

[42] J. Ketelaer.

[43] G. Bollen. Mass measurements of short-lived nuclides with ion traps. *Nuclear Physics A*, 693(1-2):3–18, October 2001.

[44] P. B. Grosshans, P. J. Shields, and A. G. Marshall. Comprehensive theory of the Fourier transform ion cyclotron resonance signal for all ion trap geometries. *The Journal of Chemical Physics*, 94(8):5341–5352, April 1991.

[45] John David Jackson. *Classical electrodynamics*. Wiley, New York, NY, 3rd edition, 1999.

[46] M. Kretzschmar. Model calculation of amplitudes for FT-ICR ion detection in a cylindrical penning trap. *Applied Physics B: Lasers and Optics*, 107(4):1007–1017, 2012.

[47] M.Ubieto Diaz. *Off-line commissioning of a non-destructive FT-ICR detection system for monitoring the ion concentration in the KATRIN beamline*. University of Heidelberg, 2011.

[48] H. Spieler. *Semiconductor detector system*. Oxford Science Publications, New York, 1rd edition, 2005.

[49] M. B. Comisarow. Signal modeling for ion cyclotron resonance. *The Journal of Chemical Physics*, 69(9):4097–4104, November 1978.

[50] A. Kosmider. *Tritium retention techniques in the KATRIN transport section and commissioning of its DPS2-F cryostat*. Karlsruher Institute of Technoloy, 2012.

[51] The KATRIN Collaboration. *KATRIN Design Report 2004*. Karlsruher Institute of Technoloy, 2004.

[52] L. Brillouin. A Theorem of Larmor and Its Importance for Electrons in Magnetic Fields. *Physical Review*, 67(7-8):260–266, April 1945.

[53] M. Ubieto-DiÂaz, D. RodriÂguez, S. Lukic, Sz. Nagy, S. Stahl, and K. Blaum. A broad-band FT-ICR Penning trap system for KATRIN. *International Journal of Mass Spectrometry*, 288(1-3):1–5, November.

[54] J. P. Blewett and E. J. Jones. Filament Sources of Positive Ions. *Physical Review*, 50(5):464–468, September 1936.

[55] M. Ueda, R. R. Silva, R. M. Oliveira, H. Iguchi, J. Fujita, and K. Kadota. A comparison of the -emission properties of pasty, liquid and glassy -eucryptite ion sources. *Journal of Physics D: Applied Physics*, 30(19):2711–2716, October 1997.

[56] T. I. Song. *Lithium ion source for satellite charge control*. Naval Postgraduate school, 1990.

[57] *Werkstoff-Datenblatt Cu-OFE*. Deutsches Kupferinstitut e.V., 2009.

[58] G. Gabrielse, L. Haarsma, and S. L. Rolston. Open-endcap Penning traps for high precision experiments. *International Journal of Mass Spectrometry and Ion Processes*, 88(2-3):319–332, 1989.

[59] S. Stahl. *Manual HV-Series*. www.stahl-electronics.com, 2012.

[60] H. L. Malcom. *Spin Dynamics: Basics of Nuclear Magnetic Resonance*. WILEY, 2008.

[61] H. Golzke. *Accuracy determination of the KATRIN FT-ICR mass spectrometers using ^{6}Li and ^{7}Li*. 2012.

[62] M. R. Beasley, R. Labusch, and W. W. Webb. Flux Creep in Type-II Superconductors. *Phys. Rev.*, 181:682–700, May 1969.

[63] Tukey J. W. Cooley, J. W. An algorithm for the machine calculation of complex Fourier series. *Math. Comp.*, 19:297, 1965.

[64] D. Werner. *Funktionalanalysis*. Springer-Verlag Berlin Heidelberg, 2007.

[65] G.-M. Greuel. *Lineare Algebra I und II*. Lecture notes, Kaiserslautern, 1999.

[66] S. Van Gorp, M. Beck, M. Breitenfeldt, V. De Leebeeck, P. Friedag, A. Herlert, T. Iitaka, J. Mader, V. Kozlov, S. Roccia, G. Soti, M. Tandecki, E. Traykov, F. Wauters, Ch. Weinheimer, D. Zakoucky, and N. Severijns. Simbuca, using a graphics card to simulate Coulomb interactions in a penning trap. *Nuclear Instruments and Methods in Physics Research Section A: Accelerators, Spectrometers, Detectors and Associated Equipment*, 638:192–200, May 2011.

[67] M. Heck, K. Blaum, R. Cakirli, D. Rodriguez, L. Schweikhard, S. Stahl, and M. Ubieto-Diaz. Dipolar and quadrupolar detection using an FT-ICR MS setup at the MPIK Heidelberg. *Hyperfine Interactions*, 199(1):347–355, 2011.

[68] M. Mukherjee, D. Beck, K. Blaum, G. Bollen, J. Dilling, S. George, F. Herfurth, A. Herlert, A. Kellerbauer, H. J. Kluge, S. Schwarz, L. Schweikhard, and C. Yazidjian. ISOLTRAP: an on-line penning trap for mass spectrometry on short-lived nuclides. *The European Physical Journal A*, 35(1):1–29, February 2008.

[69] K. Levenverg. A Method for the Solution of Certain Non-Linear Problems in Least Squares. *The Quarterly of Applied Mathematics*, 2:164–168, 1944.

[70] A. Colin Cameron and Frank A.G. Windmeijer. An R-squared measure of goodness of fit for some common nonlinear regression models. *Journal of Econometrics*, 77(2):329–342, April 1997.

[71] D. W. Mitchell. Realistic simulation of the ion cyclotron resonance mass spectrometer using a distributed three-dimensional particle-in-cell code. *Journal of the American Society for Mass Spectrometry*, 10(2):136–152, February 1999.

[72] E. N. Nikolaev, R. M. A. Heeren, A. M. Popov, A. V. Pozdneev, and K. S. Chingin. Realistic modeling of ion cloud motion in a Fourier transform ion cyclotron resonance cell by use of a particle-in-cell approach. *Rapid Communications in Mass Spectrometry*, 21(22):3527–3546, 2007.

[73] A.J. Peurrung, R.T. Kouzes, and S.E. Barlow. The non-neutral plasma: an introduction to physics with relevance to cyclotron resonance mass spectrometry. *International Journal of Mass Spectrometry and Ion Processes*, 157–158, 1996.

[74] A. J. Peurrung, R. T. Kouzes, and S. E. Barlow. Trapped nonneutral plasmas, liquids, and crystals (the thermal equilibrium states). *Reviews of Modern Physics*, 71(1):87+, January 1999.

[75] E. Hückel P. Debye. Zur Theorie der Elektrolyte. I. Gefrierpunktserniedrigung und verwandte Erscheinungen. *Physikalische Zeitschrift*, 9(25):185, 1923.

[76] X. P. Huang, F. Anderegg, E. M. Hollmann, C. F. Driscoll, and T. M. O'Neil. Steady-state Confinement of Non-neutral Plasmas by Rotating Electric Fields. *Physical Review Letters*, 78:875–878, February 1997.

[77] A. Gustafsson, A. Herlert, and F. Wenander. Mass-selective operation with REXTRAP. *Nuclear Instruments and Methods in Physics Research Section A: Accelerators, Spectrometers, Detectors and Associated Equipment*, (0):8–15.

[78] F. Ames, G. Bollen, P. Delahaye, O. Forstner, G. Huber, O. Kester, K. Reisinger, and P. Schmidt. Cooling of radioactive ions with the penning trap REXTRAP. *Nuclear Instruments and Methods in Physics Research Section A: Accelerators, Spectrometers, Detectors and Associated Equipment*, 538:17–32, 2005.

[79] S. Van Gorp. *Search for physics beyond the standard electroweak model with the WITCH experiment*. Katholieke Universiteit Leuven, 2012.

[80] T. Hamada and T. Iitaka. The Chamomile Scheme: An Optimized Algorithm for N-body simulations on Programmable Graphics Processing Units. *arXiv:astro-ph/0703100*, March 2007.

[81] Dale W. Mitchell and Richard D. Smith. Two dimensional many particle simulation of trapped ions. *International Journal of Mass Spectrometry and Ion Processes*, 165–166:271–297, November 1997.

[82] W.H. Press. *Numerical recipes*. Cambrigdge, 2007.

[83] Sz. Nagy, T. Fritiöff, M. Suhonen, R. Schuch, K. Blaum, M. Björkhage, and I. Bergström. New Mass Value for Li7. *Physical Review Letters*, 96(16):163004, April 2006.

[84] M. Brodeur, T. Brunner, C. Champagne, S. Ettenauer, M. Smith, A. Lapierre, R. Ringle, V. L. Ryjkov, G. Audi, P. Delheij, D. Lunney, and J. Dilling. New mass measurement of ^{6}Li and ppb-level systematic studies of the Penning trap mass spectrometer TITAN. *Physical Review C*, 80(4):044318, October 2009.

[85] http://www.cenbg.in2p3.fr/piperade/.

[86] R.N. Wolf, D. Beck, K. Blaum, Ch. Böhm, Ch. Borgmann, M. Breitenfeldt, F. Herfurth, A. Herlert, M. Kowalska, S. Kreim, D. Lunney, S. Naimi, D. Neidherr, M. Rosenbusch, L. Schweikhard, J. Stanja, F. Wienholtz, and K. Zuber. On-line separation of short-lived nuclei by a multi-reflection time-of-flight device. *Nuclear Instruments and Methods in Physics Research Section A: Accelerators, Spectrometers, Detectors and Associated Equipment*, 686:82–90, September 2012.

[87] M. Rosenbusch, K. Blaum, Ch. Borgmann, S. Kreim, M. Kretzschmar, D. Lunney, L. Schweikhard, F. Wienholtz, and R.N. Wolf. Buffer-gas-free mass-selective ion centering in Penning traps by simultaneous dipolar excitation of magnetron motion and quadrupolar excitation for interconversion between magnetron and cyclotron motion. *International Journal of Mass Spectrometry*, 325–327:51–57, July 2012.

Danksagung

Zu aller erst möchte ich mich bei Klaus Blaum bedanken, der einem in allen Belangen immer positiv unterstützt. Dein Engagement und deine Motivation sind beispiellos. Dein Optimismus wirkt sich auch auf deine Umgebung aus. So wurde ich immer wieder inspiriert neue Wege zu gehen, hatte aber gleichfalls auch die Freiheit eigene Ideen umzusetzen. Vielen lieben Dank für die Unterstützung während der gesamten Promotion.

Ich möchte mich auch bei Wolfgang Quint bedanken, dafür dass du die schöne Aufgabe als Zweitgutachter meiner Arbeit angenommen hast.

Ein besonderer Dank geht an Lutz Schweikhard von der Universität in Greifwald. Aus den Diskussionen mit dir habe ich immer viel gelernt und deine Ideen zu weiterführenden Experimenten haben diese Arbeit wesentlich beinflusst.

Auch einen herzlichen Dank an Stefan Stahl. Du hast uns immer mit deinem Wissen unterstützt und grundlegend zum Erfolg des KATRIN Projektes mit beigetragen.

Vor allem will ich mich bei meinen lieben Laborkolleginnen Burcu, Pauline und Marta für die schöne, lustige und vor allem erfolgreiche Arbeitszeit bedanken. Die konstruktiven Diskussionen, Denkanstösse und euer technisches Geschick haben auch dazu beigetragen, dass es mit dem FT-ICR Labor nach vorne geht. Vielen Lieben Dank!

Bei Klaus, Christian, Burcu, Tommi, und vor allem Pauline möchte ich mich für die kritische Durchsicht der Arbeit bedanken.

Auch möchte ich mich bei meinen Kollegen aus dem Nachbarlabor und der ganzen Fallentruppe am MPIK bedanken.

Mein besonderer Dank geht an Micha für die vielen lustigen Abende. Mit dir ist Heidelberg zu einer belebten Stadt geworden. Micha, Alex und Andre, die vielen schönen Kletterausflüge bleiben mir immer in Erinnerung. Nach dem Kletterunfall wart ihr immer für mich da und ihr habt mir immer geholfen. Vielen Dank für die Unterstützung.

Hua, dir gilt ein besonderer Dank. Du hast mich immer unterstützt!

Zudem möchte ich meiner Mutter Kuni, meiner Schwester Diana und meinem Bruder Detlef für die Unterstützung danken. Willi, ich werde dich ewig in meinem Herzen tragen.